To the Graduate Council:

I am submitting herewith a dissertation written by John Eilef Mathis entitled "High Resolution Multi- and Single Photon Electron Spectroscopy Using a Hemispherical Electron Spectrometer with Position-Sensitive Detection." I have examined the final copy of this dissertation for form and content and recommend that it be accepted in partial fulfillment of the requirements for the degree of Doctor of Philosophy with a major in Chemistry.

Robert N. Compton, Major Professor

We have read this dissertation
and recommend its acceptance:

Accepted for the Council:

Associate Vice Chancellor
and Dean of the Graduate School

HIGH RESOLUTION MULTI- AND SINGLE PHOTON ELECTRON SPECTROSCOPY USING A HEMISPHERICAL ELECTRON SPECTROMETER WITH POSITION-SENSITIVE DETECTION

A Dissertation

Presented for the Doctor of Philosophy

Degree

The University of Tennessee, Knoxville

John Eilef Mathis

December 1995

ABSTRACT

The design and construction of a large-radius, hemispherical-geometry electron spectrometer is described. The spectrometer employs a position-sensitive microchannel detector with position decoding accomplished by the rise-time method. Either a high-energy ultraviolet lamp, or a pulsed, dye-laser are used to photoionize samples.

Single (PES) and multiple photon (MPI:PES) ionization photoelectron spectroscopy of triethylamine (TEA) was studied. The adiabatic ionization potential of TEA was accurately determined using both single (7.47±0.04 eV) and multiphoton (7.53±0.10 eV) ionization photoelectron spectroscopy. Although excitation to both the S_1 and S_2 states can occur, multiphoton ionization always occurs out of the S_1 state. When dissociation of the cation occurs, the photoelectron energy distribution similarly reflects this partitioning.

Bromochlorofluoromethane was also studied. By using a supersonic expansion to cool the gaseous sample, it was possible to discern and assign vibrational structure of several of the halogen photoelectron peaks. In addition, the adiabatic and vertical ionization potentials were found to be 10.95 ± 0.05 eV and 11.28 ± 0.02 eV, respectively.

TABLE OF CONTENTS

LIST OF FIGURES

CHAPTER 1

INTRODUCTION

The manner in which atoms combine to form molecules depends upon the energy levels, spin, and angular momentum of the valence electrons. Chemical bonding involves the interaction of the valence electrons, whether the bonding be ionic, covalent, or van der Waal. Consequently, a complete understanding of the nature of molecules requires a detailed knowledge of the quantum mechanical state of these electrons.

The technique of photoelectron spectroscopy is a powerful tool for probing the orbitals of atoms and molecules. Angle-resolved photoelectron spectroscopy can provide information on the orbital energies and angular momenta of the electrons as well as the symmetry and structure of the ionic properties of molecules, and simplified selection rules make photoelectron spectroscopy a powerful tool for determining orbital energies.

Photoelectron spectroscopy (PES) is based upon the familiar photoelectric effect. This effect is more commonly seen in solids, wherein a photon, impinging on a surface, causes the solid to release an electron with a kinetic energy,

$$KE = h\nu - \phi, \tag{1.1}$$

where h is Planck's constant; ν is the frequency associated with the photon; and ϕ is the energy binding the electron to the solid. Photoelectron spectroscopy is used to study the energy and angular distributions of electrons ejected from atoms and molecules. By absorbing photons, the atoms and molecules gain internal energy. Once the internal energy exceeds a certain level, the atom or molecule can no longer hold onto the electron,

and the electron breaks free. The energy and angular momentum of the ejected electron reveals to the investigator from which orbital the electron originated and some of the properties of that orbital.

In the gas phase, the kinetic energy of the released electron is given by[1]

$$KE = h\nu - I.P. - \epsilon, \tag{1.2}$$

where I.P. is the energy level of the molecular species from which the electron is ejected (the ionization potential) of the gas species, and ϵ is the internal energy level of the gas species, i.e., the molecule involved may not achieve its initial vibrational and rotational states, and ϵ represents this condition. For example, the probability of an ion reaching a particular vibrational state, and thus the relative intensity of the signal, depends upon the degree to which the ground-state wavefunction overlaps with that of the various vibrational states of the ion. These probabilties are referred to as Franck-Condon factors. It is possible, therefore, by studying kinetic energies of the outgoing electrons, to deduce the properties of the ions, a task that is very difficult for conventional spectroscopy.[1]

In the broadest sense, photoelectron spectroscopy differs from conventional spectroscopy in that absorption and photoelectron ejection almost always occurs, providing that the incident photon has sufficient energy. Furthermore, photoelectron spectroscopy has the capability to probe any of the orbitals. [2]

A brief overview of the various methods for producing photoelectron spectra follows. A more detailed look will be provided in the chapter describing ionization. Different methods are used because each has characterstics which make them better suited for certain applications than the others.

For example, either a single photon from a high-energy source, or several low-energy photons working in concert (multiphoton ionization, MPI) can supply sufficient energy for ionization. The single-photon method usually employs ultraviolet lamps, x-ray sources, or synchrotron-radiation light sources. UV lamps are normally used for probing the outer orbitals where the binding energies are less than 41 eV which is the photon energy of light produced by the HeII transition. Synchrotron radiation is also used as a tuneable source of radiation.

To probe orbitals further toward the nuclei, higher photon energies are needed. These are supplied by x-ray radiation, usually from magnesium and aluminum Kα radiation. At these higher energies, more electron ejection mechanisms come into play, providing a wealth of information regarding the environment of the electron before it is ejected. Depending upon the ejection mechanism, the terms for electron spectroscopy at these photon energies are either Auger spectroscopy, or x-ray photoelectron spectroscopy (XPS) (also known as Electron Spectroscopy for Chemical Analysis (ESCA)).

Multiphoton ionization (MPI) employs more than one photon to cause an electron to leave an atom or molecule. MPI, however, requires an extremely large photon density to work and relies primarily upon just one type of light source - the laser. These lasers are normally operated in a pulsed mode which produces very high peak power.

In the case of non-resonant MPI, an incoming photon causes the bound electron to jump to a virtual eigenstate below the ionization limit (much like Raman spectroscopy), and successive photons excite the electron into a real state or into the continuum. This is

a concerted mechanism on the part of the photons, because the virtual state has an enormous uncertainty associated with its energy, and hence, through the uncertainty principle, the lifetime of the virtual state is very short.[3] Consequently, one must increase the probability of more than one photon being present at a given instant by using light of very high intensities ($> 10^9$ watts/cm^2), viz., laser light.

Because more than one photon is used to achieve ionization, the overall selection rules also are different than for single-photon conventional spectroscopy, and many one-photon "forbidden" transitions become possible. For example, the $3^2S \rightarrow 5^2S$ transition in sodium vapor which is one-photon forbidden (because $\Delta l = 0$) is two-photon allowed through virtual ^2P states.

An additional advantage of MPI is that ionization can be accomplished with lasers having low photon energy. Atoms and molecules which require single-photon energies in the UV range for ionization can be ionized via MPI with lasers operating in the visible light range. Furthermore, if one can tune the photon energy such that real intermediate states are reached, one can selectively ionize atoms and molecules. This is known as resonantly enhanced MPI (REMPI).

REMPI often results in very simple spectra. REMPI uses the same multiple photon phenomenon to ionize the atom or molecule, but the key difference is that instead of only virtual states being reached, a real, intermediate state is reached before subsequent photons are absorbed to cause ionization. This resonant state greatly increases the MPI signal since the energy of the intermediate state is better defined than in the non-resonant case, and, therefore, the lifetime of the state is much longer. This increases the

probability of the electron absorbing additional photons before it decays back into a lower energy state, thereby increasing the REMPI signal. Because this intermediate is selectively enhanced, fewer peaks are observed in the electron spectrum as the non-resonant peaks have a much lower intensity. Moreover, the intermediate state often acquires the same geometry as the ion which causes, according to the Franck-Condon principle, the resulting PES spectrum to consist mainly of the $\Delta v = 0$ transition.

Once the photoelectrons are produced a spectrometer is used to measure their energy. Many types of spectrometers exist, but they can be divided into two broad categories. The first type uses electrostatic fields to deflect the electrons and are known as dispersive spectrometers, The second type, known as time-of-flight (TOF) electron analyzers, sorts the electrons by the time it takes them to traverse some predetermined distance. These are. An ideal electron spectrometer would have high energy resolution at all energies and good electron collection efficiency.

This dissertation describes the construction and operation of an electron spectrometer system of hemispherical geometry, a dispersive type. Design considerations and operating procedures of this spectrometer will be described. Some noteworthy features of this spectrometer include a large electron-trajectory radius and a position-sensitive detector which allows single electron counting. The system is capable of both single and multiphoton ionization as it uses both a pulsed dye laser and an ultraviolet lamp to effect photoionization of gases.

The versatility of using two photon sources will be demonstrated by a study of the photoionization of TEA. Both sources were used to determine the identity of resonant

states through which MPI proceeds. Triethylamine was chosen because it has some unusual photophysical properties, among which is its strong absorption of UV light..

Bromochlorofluoromethane (BCFM), one of the simplest chiral molecules, was also studied. Cooling of BCFM via supersonic expansion enabled the spectrometer system to resolve for the first time the vibrational structure of the photoelectron peaks due to ionization of the bromine.

CHAPTER 2

HISTORY OF GAS-PHASE PHOTOELECTRON SPECTROSCOPY

Although the photoelectric effect has been known for over 75 years (Einstein received the 1921 Nobel Prize for the theory of the photoelectric effect) it has only been since the early 1960's that photoelectron spectroscopy has been widely used.

Much effort was expended during the first part of the twentieth century to duplicate the photoelectric effect in the gas phase. Because of the difficulty with scattered light interfering with the measurements, no one was able to observe the photoelectric ionization of a gas until Williamson[4] (1923) detected ions produced by the illumination of a beam of potassium ions with UV light. Foote and Mohler[5] (1925) used an improved device which reduced space-charge effects in order to observe the photoionization of atomic cesium vapor.

Until the development of better energy analyzers, photoelectron spectroscopy languished. Kai Siegbahn's group in Sweden improved upon the existing magnetic-deflection electron spectrometers[6] to probe solids with x-rays and measure the the energies of the ejected electrons.[7]

Little was accomplished in gas phase photoelectron spectroscopy until Vilesov, et al.[8] (1961) used a vacuum monochromator and an electrostatic, retarding grid photoelectron spectrometer to investigate the electron energy spectrum of benzol and aromatic amines in the gas phase. Unaware of these results, Turner and Al Joboury[9] reported a year later that they were the first to measure the ionization potentials of several

gaseous elements and simple molecules using photoelectron spectroscopy which employed a similar type of retarding grid spectrometer. Since then, many other types have been employed to measure photoelectron energies. Among these are dispersive instruments with many different geometries, e.g., spherical, cylindrical, cylindrical mirror, and parallel plate types. In addition the time-of-flight principle has been used for measuring electron energies. The latter type is well-suited for systems employing pulsed-lasers to effect multiphoton ionization.

History of Multiphoton Ionization

The difficulty in obtaining two-photon transitions was initially explained in 1929 by Göppert.[10] Two years later, she developed the full theory in her doctoral dissertation.[11] She showed that two-photon spectroscopy, although possible, would be difficult to accomplish because of the quadratic dependence upon light intensity for the two-photon absorption. New light sources would be needed to make this technique feasible.

The first two- and three-photon absorptions were observed in the low-energy, radio-frequency region. Hughes and Grabner[12] (1951) noticed an extra peak in their radiofrequency spectrum of $Rb^{86}F$ which they attributed to a "double quantum transition." Later, Kusch[13] (1954) observed two- and three-photon transitions in the radiofrequency spectrum of an O_2 beam which had been cooled to 77K.

Almost immediately after the invention of the laser, researchers began investigating multiphoton phenomena in earnest, with the first two-photon, visible-light transition observation by Peticolas and Rieckhoff (1963).[14] These researchers produced blue light

when high-intensity, red light from a ruby laser (694.3 nm) illuminated a Eu^{2+} - doped CaF_2 crystal inducing two-photon absorption. Soon thereafter, they achieved[15] (1963) the first two-photon absorption by a molecular system when they used a ruby laser to probe crystalline anthracene. The early lasers, however, produced light of a fixed wavelength, greatly limiting the number of systems of which spectra could be obtained. This changed when Fröhlich and Mahr[16] in 1966 combined the ruby laser with filtered light from a xenon flashlamp to scan, in a limited way, the spectrum of crystalline anthracene performing the first two-color, two-photon spectroscopy. Most of the work done during this period examined the ionization properties of atoms and simple molecules.

After the discovery of stimulated emission in organic dye compounds by Stockman and colleagues[17] and the development of the dye laser by Sorokin and Lankard,[18] it was not long before a tunable dye-laser operating in the visible wavelengths was developed.[19] The invention of the tunable, organic-dye laser enlarged the MPI field immensely, allowing the study of a wider range of complicated systems. Bergman and Jortner[20] (1972) paved the way by using a ruby-laser-pumped dye laser to measure the spectra of several organic molecules in both solids and solutions. Gas phase two-photon absorption was first observed by Hoschstrasser et al. (1974) in benzene.[21] Bray, et al.[22] expanded on this work by examining nitric oxide, the first small molecule and the first diatomic molecule to be studied by multiphoton methods. They examined the individual rotational levels of the $A\ ^2\Sigma^+$ state using a nitrogen-laser pumped dye laser. Eight months later, Johnson et al. reported[23] the first non-resonant multiphoton ionization of a molecule, nitric oxide. They also used a nitrogen pumped dye laser to produce the four-photon

ionization spectrum.

Using more than one photon can also be used to eliminate Doppler broadening of spectral lines. Using two-photons to eliminate Doppler broadening was proposed by Vasilenko and co-workers[24] in 1970. In this method, the two photons are traveling in opposite directions. If the molecule is moving with a velocity, v, relative to the light, then the molecule in the molecule frame of reference sees a photon of frequency $\omega_o(1-v/c)$. For the photon traveling in the opposite direction, the molecule sees a photon of frequency of $\omega_o(1+v/c)$. Hence, the moving molecule will be excited to an energy level of $2\omega_o$ independent of velocity. Four years after Vasilenko *et al.* proposed this "Doppler-free" spectroscopy, three groups[25,26,27] simultaneously reported the observation of two-photon absorption in sodium with the absence of Doppler broadening.

Studies of organic compounds by MPI has ranged from simple alkanes to rather large polyaromatic compounds. Polyatomic molecules, however, increase the complexity of the photoelectron spectrum. In addition to electronic transitions, rotational and vibrational transitions are also possible with polyatomics. Excess energy can be channeled into molecular pre-dissociation, rotational and vibrational modes, autoionization, and radiationless transitions.

The marriage of MPI with photoelectron spectroscopy occurred not long after the invention of the laser. In 1972, Evans and Thonemann[28] obtained the first electron kinetic energy spectrum originating from multiphoton ionization by focusing light from a Q-switched ruby laser into a vacuum chamber and thereby ionizing the residual hydrocarbon vapors.

The first resonant MPI of a molecule, I_2, was accomplished by Dalby and co-workers[29] who at the same time discovered a Rydberg state in iodine which, until then, had been hidden because the transition is one-photon forbidden. Soon thereafter, Compton and co-workers (1980) accomplished the first, resonantly-enhanced MPI-PES (REMPI) of an atom, xenon. In the years since, the REMPI of xenon has become a reliable calibration standard, and the number of molecular and atomic systems studied by both the MPI and REMPI processes has grown enormously.

CHAPTER 3

IONIZATION

Introduction

Two methods for producing photons for ionization are used in the spectrometer: a discharge lamp producing photons in the ultra-violet region for single-photon spectroscopy, and a pulsed laser for multiphoton studies. A goal for this arrangement is to combine the output from single-photon source with the laser's output in order to perform state-selected photoelectron spectroscopy producing photoelectrons with energies well above the ionization threshold.

The discharge lamp, manufactured by VSW, Ltd., normally used helium to produce the UV light. In this type of lamp, gases flowing through a capillary are ionized and excited by an electric discharge thereby producing light. By adjusting the flow conditions, specific lines of the emitted light can be preferentially produced. For example, under low pressure conditions, helium emits light primarily at a wavelength of 58.43 nanometers (HeI emission) corresponding to an energy of 21.22 eV. By further reducing the pressure, a substantial amount of HeII light can be produced with a photon energy of 40.8 eV. At higher pressures, the HeII light is reduced by photoabsorption, producing He^+ ions.

Reducing the pressure also has a beneficial effect on the ultimate resolution. As Samson[30] shows, the pressure within the discharge capillary determines in part the line width associated with the emitted radiation, with the line width varying proportionally

from 3 meV to 5 meV over the typical operating pressure range of a 58.4 nm He lamp.

Ionization Characteristics

A photon of sufficient energy, E=hν, can eject an electron from an orbital of an atom or a molecule:

$$M + h\nu \rightarrow M^* + e. \tag{3.1}$$

The kinetic energy of the ejected electron, K.E., represents the difference in energy between the energy of the photon and the binding energy, E_{bind}, holding the electron to the atom

$$K.E. = h\nu - E_{bind}. \tag{3.2}$$

If the object being ionized is a molecule, there exists other paths, such as rotational and vibrational energy, along which the excess energy can be expended, and these, then, are also included, i.e.,

$$K.E. = h\nu - E_{bind} - E_{vib,rot}. \tag{3.3}$$

When ionization occurs, the molecule's orbital angular momentum changes according the usual dipole selection rules, viz., by $\Delta L = 0, \pm 1$, and its spin multiplicity changes by ± 1.

The angular distribution of the photoelectrons reflects the orbital from which they came. As noted above, the photoelectron carries away angular momentum of quantity λ

$= l, l \pm 1$. For example, if the originating orbital was a pi orbital in a diatomic molecule, then the photoelectron's wavefunction will consist of a mixture of sigma and delta wavefunctions. The intensity of the photoelectron current as a function of the observation angle for polarized light is given by:[2]

$$I(\theta) = \frac{\sigma}{4\pi}\left(1 + \frac{\beta}{2}(3\cos^2(\theta) - 1)\right), \tag{3.4}$$

and for unpolarized light:

$$I(\theta) = \frac{\sigma}{4\pi}\left(1 + \frac{\beta}{2}\left(\frac{3}{2}\sin^2(\theta') - 1\right)\right). \tag{3.5}$$

where σ is the ionization cross section. β is called the anisotropy parameter and is a complicated function of the angular momentum, ionization cross sections, and phase differences between the outgoing waves. Since the anisotropy parameter depends upon the orbital angular momentum, the polarization dependence can be used to help determine the orbital from which the electron was ejected.

For equation (3.1), the angle θ is measured from the light's electric vector; for equation (3.2), the angle θ' is measured from the direction of the light. It is possible to eliminate the β dependence by setting the angle to 54.736°. With early photoelectron spectrometers, it was not possible to rotate the polarization of a UV source, and so it was necessary to rotate the apparatus. For the light source used in this dissertation, however, changes in polarization are effected by the use of grazing-incidence gold-plated mirrors.

Eland[1] states that two rules can often be applied to the relationship between the single-electron-process photoelectron spectrum and the electronic spectrum of a closed-shell molecule:

> "(1) Each band in the spectrum corresponds to ionization from a single molecular orbital.
>
> (2) Each occupied molecular orbital of binding energy less than hν gives rise to a single band in the spectrum."

In a sense, these rules arise from Koopmans' theorem[31] which states that each ionization potential from a closed-shell molecule is equal in magnitude to the orbital energy of the electron being removed. However, as Eland[1] points out, caution should be used in ordering the ionic states based upon the ordering of calculated orbital energies based upon Koopmans' theorem. Oftentimes, the orbital energies lie too close together, the uncertainty in the calculated orbital energies is large, and correct assignments cannot be made. Most importantly, Koopman's theorem ignores the effects of configuration interaction between electrons and electron correlation. Eland suggests that not only should calculated energies be used in the assignment, but that other characteristics, such as the shapes and intensities of the bands, be included as well.

The appearance of the photoelectron bands depends on the Franck-Condon overlap between the ground state and the ionized state. This principle behind this overlap derives from the Born-Oppenheimer principle which allows for the separation of the electronic and nuclear motions of a molecule. Given that the wavefunction for a molecule with internuclear separation R and electron position **r** is

$$\Psi = \psi_e(r,R)\psi_{vib}(R), \tag{3.6}$$

The intensity of the electric dipole transition is proportional to the square of the transition moment between the initial state $|i\rangle$ and the final state $|f\rangle$

$$\mu_{if} = \int\int \Psi^{*\prime} \mu \Psi'' \, dR\, dr \tag{3.7}$$

where $\mu = \mu_{nuclear} + \mu_{electronic}$. Expanding the wavefunction, we obtain

$$\mu_{if} = \int \psi^*_{e'} \psi^*_{vib'} (\mu_e + \mu_{nuclear}) \psi_{e''} \psi_{vib''} \, dR\, dr, \tag{3.8}$$

with

$$\mu_{if} = \int \left(\int \psi^*_{e'} \mu \psi_{e''} dr \right) \psi^*_{vib'} \psi_{vib''} dR + \int \psi^*_{e'} \psi_{e''} dr \int \psi_{vib'} \mu_{nuclear} \psi_{vib''} dR. \tag{3.9}$$

The second term on the R.H.S. of equation (3.6) vanishes because the electronic wavefunctions belong to the same complete, orthonormal set. Setting

$$\mathbf{M}_{if} = \int \psi^*_{e'} \mu \psi_{e''} dr \tag{3.10}$$

we can bring this term outside of the first term on the R.H.S. of equation (3.6) if it does not depend on R, or if the dependence is very small. We then have

$$\mu_{if} = \overline{M_{if}} \int \psi^*_{vib'} \psi_{vib''} dR. \tag{3.11}$$

Hence, the Franck-Condon factor,

$$\left|\int \psi^{*}_{vib'} \psi_{vib''}\, dR\right|^2 \qquad (3.12)$$

gives the relative intensity of a transition between two vibrational states.

If the overlap is perfect, i.e., if the potential curve of the ionized state is the same as the ground state's and lies directly above the ground state, then the photoelectron band will consist of one, very intense peak. If, on the other hand, the potential curve has been altered by going to the ionized state, then the band will consist of several peaks. For example, Figure 1 shows the photoelectron spectrum of nitrogen generated by using HeI light for this dissertation. Nitrogen has the ground-state configuration $1\sigma_g^2 1\sigma_u^2 2\sigma_g^2 2\sigma_u^2 1\pi_u^4 3\sigma_g^2$; this is shown diagrammatically in ?. The assignments shown were previously done by conventional absorption spectroscopy. The lowest photoionization potential is assigned to the $X\ ^2\Sigma_g^+$ state, and results when an electron is removed from the $3\sigma_g$ orbital. This band has only a few peaks, showing that the geometry of the nitrogen molecule did not change much when the electron was removed, and, consequently, it can be concluded that this orbital is not strongly bonding. The next band, $A^2\Pi_u$, shows many more peaks, reflecting the removal of an electron from the strongly bonding, $1\pi_u$ orbital. Finally, it can be deduced that the $2\sigma_u$ orbital ($B^2\Sigma_u^+$) is not strongly anti-bonding.

The number of electrons entering the analyzer can be calculated by considering the number density of molecules in the ionizing region, N, the intensity of the light, Φ, the cross section for ionization, σ, and the acceptance angle of the analyzer, Ω. This is

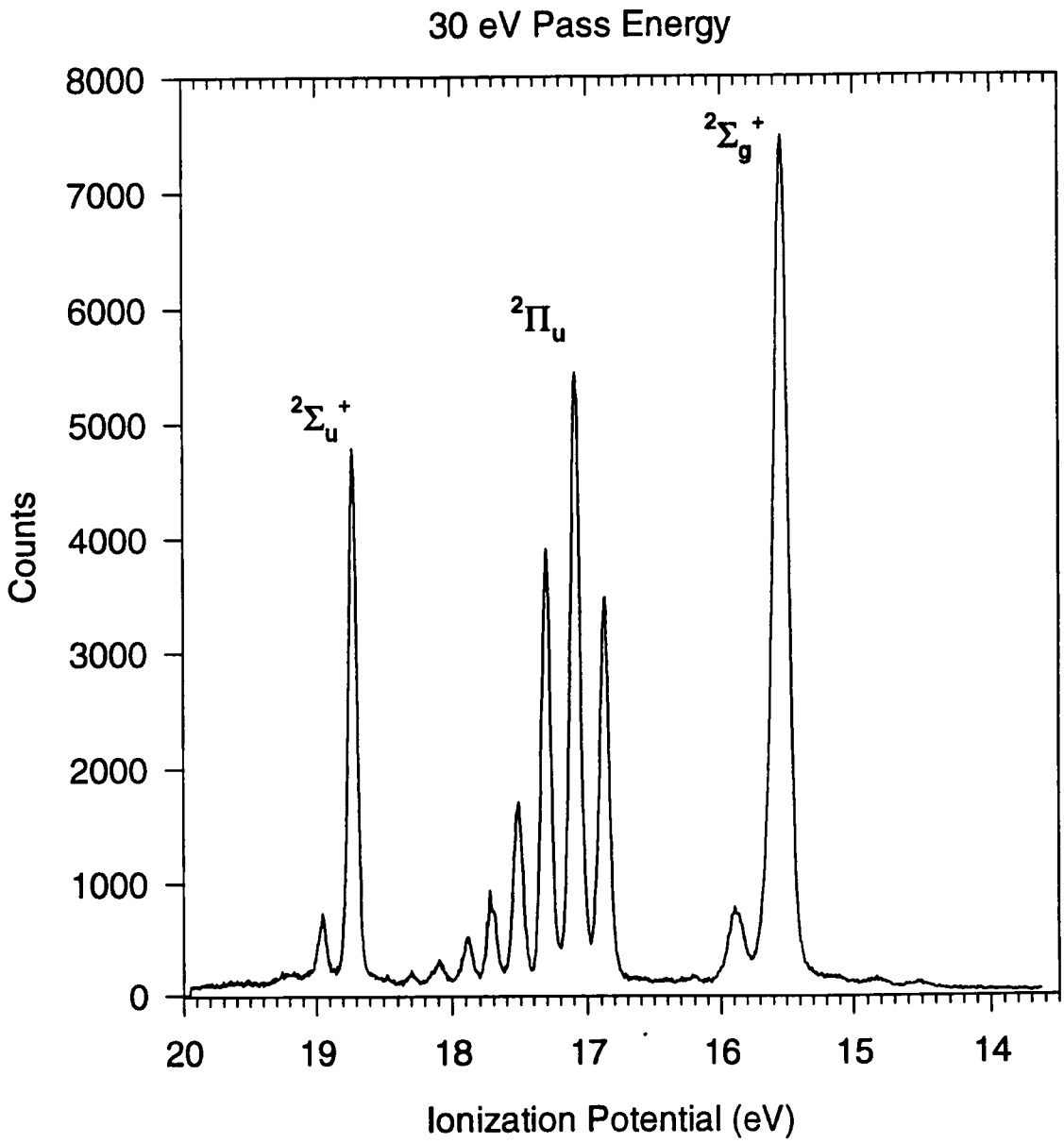

Figure 1. Full spectrum of nitrogen taken with analyzer described in this dissertation.

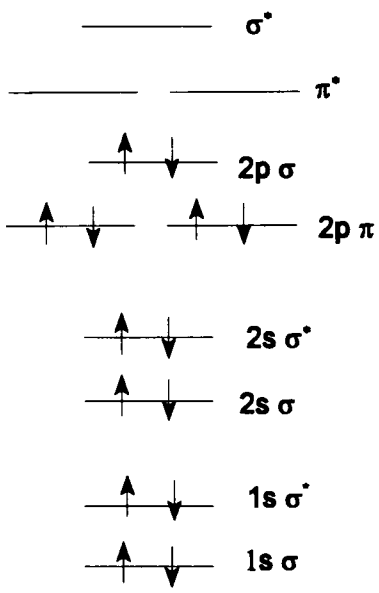

Figure 2. Energy levels of N_2.

given by the equation

$$I = \sigma\phi NV\Omega \tag{3.13}$$

For single photon spectroscopy with HeI light, the typical cross section is on the order of 10^{-18} cm^2. The light intensity is 10^{12} cm^{-2} s^{-1} For the effusive source described above in the ionizing section, the number density was 10^{10} cm^{-3}, and combining with the acceptance solid angle of 0.0025 steradian gives a rate of 25 electrons/second, which is the same order of magnitude as observed experimentally.

Multiphoton Ionization

A Quanta-Ray model DCRII Nd-YAG laser was used to produce the conditions necessary for MPI. The laser's fundamental 1.06 μm output was converted, either by sending it through frequency doubling and tripling crystals or by pumping a dye laser, to the desired wavelength. A typical output from the dye laser, at 440 nm, was 4 mJ/pulse at pulse repetition rate of 10 Hz. Since the pulse width was typically 9 nsec, this output corresponds to a power of 440 kilowatts. To increase the photon density further, the light was focussed to a small spot by lens with a short focal length.

The theory of multiphoton transitions is much more complicated than the single-photon case. As stated earlier, a multiphoton transition occurs when a bound electron first absorbs a single photon which raises the electron to a virtual energy level. Subsequently, and nearly instantaneously, the electron absorbs another photon which raises the electron still further in energy. This process continues until either the electron reaches a real quantum level, or the electron reaches the continuum and

escapes. Please see Figure 3 for an illustration.

Treatment of the multiphoton process generally requires either second-order perturbation theory, or a density matrix method. For reasons of brevity, only a general overview of the theory will be given here.

The results obtained Faisal[32] will be briefly described. For a more detailed description, the reader is urged to use this reference or that of Lambropoulos[33].

As stated above, a multiphoton transition occurs when a photon excites an electron to a virtual state at which point it subsequently absorbs an additional photon. This process continues until either the electron escapes, or it decays back to a lower state. It becomes possible, therefore, to use light with relatively low energy to attain energies equivalent to UV light.

For example, for a two-photon transition from state $|1\rangle$through a virtual state $|i\rangle$, to a final state $|2\rangle$, the transition moment, R_{12}, is given by[31]

$$R_{12} = \frac{1}{2}\sum_{i} \frac{\langle 1|\boldsymbol{\mu E}|i\rangle\langle i|\boldsymbol{\mu E}|2\rangle}{E_2 - E_i - h\nu} \qquad (3.14)$$

where $\boldsymbol{\mu}$ is the dipole moment; $\boldsymbol{E}$ is the electric field; and E_1 and E_2 are the energies of the two levels. Thus, the overall transition can be thought of as two successive electric dipole transitions. Hence, many transitions that are one-photon forbidden become possible in two-photon transitions, e.g., g ↔ g and u ↔ u.

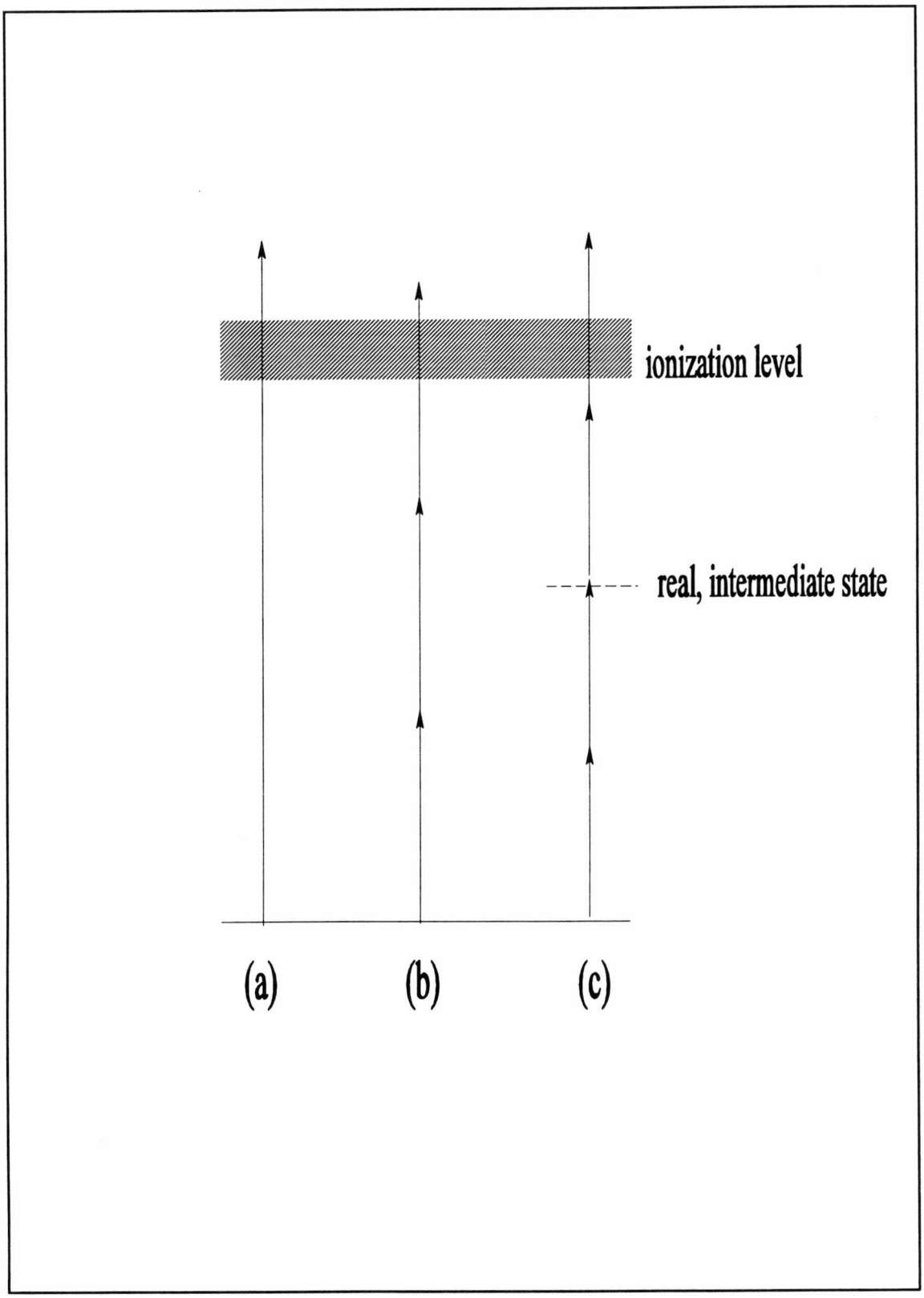

Figure 3. Types of photoionization showing (a) single-photon ionization, (b) non-resonant MPI, and c) resonantly enhanced MPI (REMPI)

In the case multiphoton ionization, the electron escapes. Faisal shows that the rate of absorption of n photons in this case can be calculated according to

$$W_{i\to f}^{(n)} = 2\pi\left(\frac{2\pi\alpha F\omega}{e^2}\right)^n |T_{(i\to f)}^{(n)}|^2 \delta(\omega_i + n\omega - \omega_f) \tag{3.15}$$

where F is the photon flux given by

$$F \equiv \frac{E^2}{8\pi}\frac{c}{\hbar\omega} \tag{3.16}$$

and T represents the matrix elements:

$$T_{i\to f}^{(n)} \equiv \langle f|DG[\omega_i+(n-1)\omega]DG[\omega_i+(n-2)\omega]...DG[\omega_i+\omega]D|i\rangle \tag{3.17}$$

where G is the Green's function and D is the dipole moment operator. Except for very simple molecules, these matrix elements are difficult to calculate.

The rate of ionization per atom can be cast in a slightly different form which shows the explicit dependence on the light intensity, i.e.,

$$W_n = \delta_n I^n \tag{3.18}$$

where δ_n is the n-photon generalized ionization cross section and has units $cm^{2n}\ s^{n-1}$, and I is the laser intensity with units of photons $cm^{-2}\ s^{-1}$.

If the light is in resonance with an intermediate state, the cross-section is greatly

enhanced. As an example, Goodman and Philis show[34] that for a four-photon REMPI the intensity coefficient is given by

$$\delta_4 = \sum_i \sum_j \sum_k \left| \frac{\langle 1|\mu_a|k\rangle\langle k|\mu_b|j\rangle\langle j|\mu_b|i\rangle\langle i|\mu_a|o\rangle}{(E_{ko}-3\hbar\omega_L)(E_{jo}-2\hbar\omega_L)(E_{io}-\hbar\omega_L)} \right|^2 \tag{3.19}$$

For a 2+2 REMPI from state E_0 through the intermediate state E_f, they show that the MPI electron current is given by

$$Current_{MPI} = \frac{N_o \delta_2^{(r)} \delta_2^{(f)} I^4}{\delta_2^{(f)} I^2 + \gamma} \tag{3.20}$$

where $\delta_2^{(r)}I^2$ is the 2-photon pumping rate from E_o to E_f, and $\delta_2^{(f)}I^2$ is the 2-photon pumping rate from E_f to the continuum. γ represents the rate of radiative depopulation from E_f, and N_o is the gas density. For typical values, they give

$$\delta_2^{(r)} = 10^{-50} \frac{cm^4\ s}{molecule\ photon^2}$$
$$\delta_2^{(f)} = 10^{-40} \frac{cm^4\ s}{molecule\ photon^2} \tag{3.21}$$

For low laser-light intensities or small absorptivity, $\gamma >> \delta_2^{(i)}$, and the overall ionization probability is proportional to $\delta_2^{(r)}\delta_2^{(i)}I^n$. For higher intensities, $\delta_2^{(i)} >> \gamma$, and since $\delta_2^{(i)} > \delta_2^{(r)}$ in most cases, saturation of the ionization step causes the overall ionization

probability to be proportional to $\delta_2^{(r)}I^2$.

Lasers provide a convenient source for high-photon density. For the far-field case, the beam waist at the focus is given by[35]

$$w = \frac{f\lambda}{\pi d} \tag{3.22}$$

where f is the focal length of the lens; λ is the wavelength of the laser light, and d is the diameter of the laser beam before it is focussed. Under diffraction-limited conditions, this reduces to $w = f\theta$. The confocal beam length gives the distance from the focus at which the beam waist increases by a factor of $\sqrt{2}$ over that of the focal value.

$$b = \frac{2\pi w^2}{\lambda} \tag{3.23}$$

As an example, the molecule nitric oxide can be ionized via a 2+2 resonant process. Using the respective cross sections given above, one can calculate the maximum MPI current. Given a gas density over the entrance aperture of 10^{10} cm^{-3}, a laser power density of 10^8 W/cm^2 at a wavelength of 451 nm, the MPI current density for a 1 cm^3 irradiated volume would be 5.2×10^{16} electrons/(s-cm^3). With a lens having a focal length of 20 cm and laser beam having a width of 0.5 cm before being focussed, the ionization volume is 1.2×10^{-8} cm^3. Thus, the maximum number of electrons that can be produced per second is 6.1×10^8, corresponding to an average current of 9.8×10^{-11} A.

A. C. Stark Effect

A strong D.C. electric field will split the absorption lines in a spectrum into several components. This is known as the Stark effect. The intense A.C. electric vector of the light of a laser creates enormous electric fields and can, itself, split the lines.

The a.c. Stark effect involves rapid transitions between the split states in the presence of an optical field. Using perturbation theory on the system, one arrives at an expression for the magnitude of the splitting from an initial level, f, as[36]

$$\Delta E_f = \frac{1}{4}\xi^2 \sum_g \left[\frac{|V_{fg}|^2}{(E_f - E_g - \hbar\omega)} + \frac{|V_{fg}|^2}{(E_f - E_g + \hbar\omega)} \right] \qquad (3.24)$$

where ξ is the electric field strength; E_f and E_g are the energy levels of f and g, respectively; and V_{fg} is the dipole matrix moment connecting the two levels.

In multiphoton spectroscopy, the a.c. Stark effect manifests itself as a broadening in the signal response. The profile of a laser pulse does not resemble a square wave, and thus the electric field associated with the pulse does not turn on and off instantly. According to Kruit *et al.*[37], if one assumes that the resonant energy levels are a.c. Stark shifted by $\Delta E = \alpha I$ (where α is the Stark shift coefficient and I is the laser intensity), then the molecule will be excited only during that time when the laser intensity equals the energy difference between the *shifted* levels. Therefore, the shape of the resonance peak reflects the distribution of intensities in space and time.[36]

CHAPTER 4

ANALYZER THEORY AND CONSTRUCTION

The types of electron spectrometers most commonly used can be divided into two groups: those which rely upon separating electrons of different energy spatially - the dispersive instruments - and those which separate them temporally. Among the former are the retarding grid, cylindrical mirror, hemispherical shell, and cylindrical shell. The latter type includes the time-of-flight and magnetic bottle spectrometers.

The retarding grid was the first type used in gas phase photoelectron spectroscopy because of its simplicity in design and operation and its high electron-collection efficiency. However, this type suffers the drawback of poor resolution, and requires taking the derivative of the collected current to produce a spectrum.

The cylindrical mirror analyzer also has a high collection efficiency for electrons. Moreover, it has a higher theoretical resolution than either the hemispherical-sector or cylindrical-sector types, and its entrance and exit apertures lie in equipotential planes. Despite these advantages, it is not often used in gas phase photoelectron work because of the difficulty in changing the orientation of the entrance aperture. For situations where fixed geometries are used, such as for Auger spectroscopy it is the instrument of choice.

The time-of-flight spectrometer has excellent resolution for low energy electrons and has a very good electron-collection efficiency. It also has the advantage of being able to measure simultaneously all electron energies. Other attractive features are its

simplicity of construction and operation, especially when used with pulsed lasers. A serious drawback of the time-of-flight electron spectrometer, however, is the limited energy range over which useable resolution can be realized. This can be seen by considering its principle of operation.

The time for an electron of energy, E, and mass, m, to travel a distance, l, is

$$t = \frac{l}{\sqrt{2mE}}. \tag{4.1}$$

Differentiating this equation with respect to E gives

$$dt = \frac{l}{\sqrt{2m}} E^{-\frac{3}{2}} dE, \tag{4.2}$$

showing how the resolution varies with electron kinetic energy.

Similar to the time-of-flight spectrometer, the magnetic bottle spectrometer uses a magnetic field to direct all of the electrons toward the time-of-flight tube. This method increases the collection efficiency, but has the disadvantage of introducing magnetic fields into the ionization region which could affect the process being studied.

The hemispherical analyzer, on the other hand, provides very good resolution over a much wider range of electron energies. Above 5 eV, where external fields become relatively minor, the resolution, $E/\Delta E$, of a hemispherical analyzer is essentially constant, depending only upon the dimensions of the analyzer and the slit widths. Some disadvantages of the hemispherical analyzer are the complexity of

construction and the necessity for focussing the electrons before they enter the analyzer.

Because a design goal of this apparatus was the capability of performing two-color experiments with both a UV lamp and a laser, the electron spectrometer described in this dissertation needs to have high resolution at both high and low electron energies and to accommodate position sensitive detection. To this end, it was decided to use a hemispherical type of spectrometer with a wide gap between the hemispheres.

Hemispherical Analyzer

As its name implies, the hemispherical analyzer consists of two, concentric hemispheres. A schematic of the analyzer is shown in Figure 1. An electrical potential is applied between the hemispheres which spatially discriminates electrons of different energies. The theory of operation of the hemispherical electron energy analyzer was first put forward by Purcell.[38] As he pointed out, the paths of equal-energy electrons in a hemispherical analyzer follow the trajectories of great circles, with the foci of the electrons located by a line passing through the radius center, terminating at the electrons' origin, and intersecting the mean electron radius. The magnification from the source to the image plane is minus unity.

The requirement to operate at low pass energies (< 1 eV) pushes the need to minimize the effects of variations in surface charge. One way to do this is to increase the size of the analyzer so that the electrons pass far from the surfaces. To further reduce the effect, the surfaces normally are coated with a graphite film so that surface charges are dissipated. The design goal of the spectrometer was to have a resolution of better than 0.010 eV at a transmission energy (pass energy) of 1 eV.

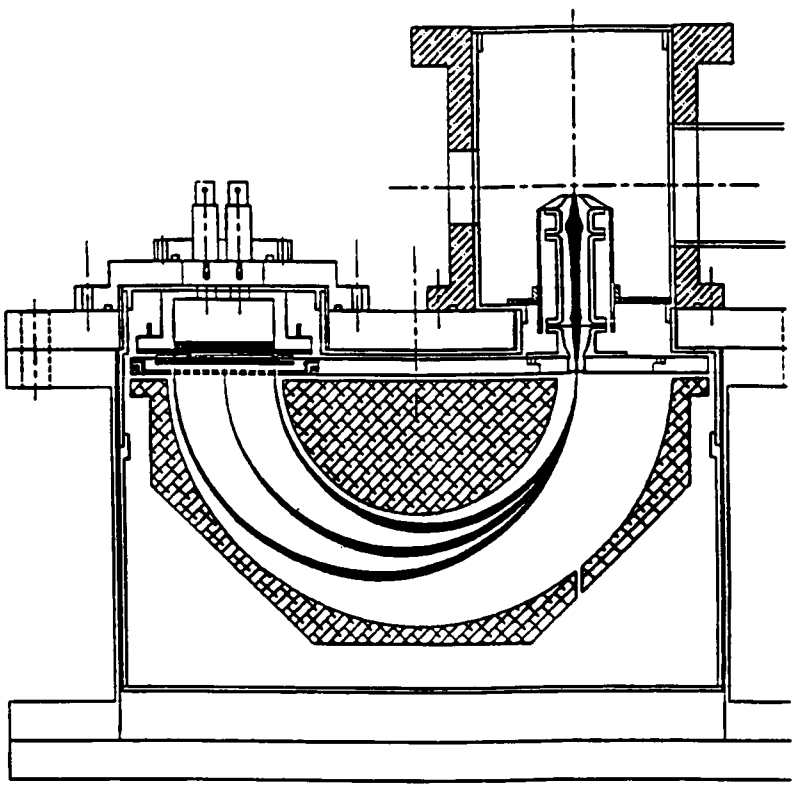

Figure 4. Schematic diagram of the analyzer.

The theoretical transmission of the spectrometer at a given pass energy, the electron energy the analyzer allows through, is proportional to the mean radius of the electron trajectory and is given by[39]

$$\frac{\Delta E_{o,½}}{E} = \frac{w}{2R_o} + \alpha^2 \qquad (4.3)$$

where $E_{o,1/2}$ is the half-height width of the signal peak; w is the average width of the slits, R_o is the electron-trajectory radius, and α is angular spread of the electrons as they enter the analyzer. Hence, the larger the radius, all things being equal, the higher the resolution. Other factors, hovever, limit the extent to which the radius can be increased. First of all, increasing the radius also increases the mass of the system which can be a strain on the supporting structure and the alignment mechanism.

The other major factor that limits the size of spectrometer is the presence of magnetic fields. Although shielding with either Helmholtz coils or Mu-metal effectively reduces external magnetic fields, the fields cannot be eliminated entirely, and these residual magnetic fields limit the size of the analyzer. An analysis by Roy and Carette[40] yields the following relationship between the residual magnetic induction B (gauss), the electron energy E_o (eV), the path length l (cm), and the maximum deviation of the electron beam d (cm):

$$B = 6.74 E_o^{½} \frac{d}{l^2}. \qquad (4.4)$$

The analyzer described in this disseration is completely shielded by Mu metal, a high-magnetic-permeability material. Measurements put the maximum magnetic induction within the analyzer at 0.001 G. Using a typical lower limit for E_o of 0.5 eV, and constraining d to be less than the slit diameter (~ 0.1 cm), one obtains a maximum for l of ~ 30 cm, or a radius of ~ 10 cm.

Having set the radius, the next step is to determine w and α. Rudd[41] determined that optimum resolution for a hemispherical analyzer is obtained when $\alpha^2 = w/2R_0$. Using equation (4.3), this leads to an entrance slit width of 1 mm, with $\alpha = 4.0°$.

The potentials on the hemispheres required for an electron of kinetic energy, KE, to pass through to the detector are easily derived. First the potential, Φ, within the hemispheres having radii R_1 and R_2 must satisfy Laplace's equation

$$\nabla^2\Phi = 0, \tag{4.5}$$

with the boundary conditions $\Phi(R_1) = V_1$ and $\Phi(R_2) = V_2$.

The spherical symmetry of the problem points towards a solution in spherical coordinates with the result:

$$\Phi(r,\theta,\phi) = \frac{a}{r} + b. \tag{4.6}$$

To find the constants a and b, we apply the boundary conditions, with the results

$$a = \frac{V_1 - V_2}{\frac{1}{R_1} - \frac{1}{R_2}}; \tag{4.7}$$

$$b = \frac{R_1 V_1 - R_2 V_2}{R_1 - R_2}. \tag{4.8}$$

This gives us the first of the two equations needed to find V_1 and V_2. The second equation is found by equating the electric force within the hemispheres with the centripetal force of the electrons traveling in a circular path.

The electric field within the hemispheres is given by

$$E = -\nabla\Phi = -\frac{\partial\Phi}{\partial r} = \frac{a}{r^2}. \tag{4.9}$$

Equating the two forces,

$$eE = \frac{mv^2}{r}. \tag{4.10}$$

It is readily apparent that this can be put in terms of the kinetic energy (transmission energy, TE) required for electron passage:

$$e\frac{a}{r^2} = \frac{2TE}{r}. \tag{4.11}$$

This gives us a in terms of the TE:

$$a = 2\frac{TEr}{e}. \tag{4.12}$$

If the electron has a kinetic energy, KE, before it enters the analyzer, it must be accelerated by a potential of V=(TE-KE)/e to match the TE of the analyzer. This is also the potential within the hemispheres at the entry point, i.e.,

$$\frac{a}{r} + b = \frac{TE - KE}{e}. \tag{4.13}$$

Thus, we now have the two equations needed to solve the problem in terms of KE, TE, and r, viz.,

$$\frac{V_1 - V_2}{\left(\frac{1}{R_1} - \frac{1}{R_2}\right)r} + \frac{R_1V_1 - R_2V_2}{R_1 - R_2} = \frac{TE - KE}{e}; \tag{4.14}$$

and

$$2\frac{TE}{e} + \frac{R_1V_1 - R_2V_2}{R_1 - R_2} = \frac{TE - KE}{e}. \tag{4.15}$$

The solution to the problem is, therefore,

$$V_1 = \frac{1}{e}\left(TE(2\frac{r}{R_1} - 1) - KE\right); \tag{4.16}$$

$$V_2 = \frac{1}{e}\left(TE(2\frac{r}{R_2} - 1) - KE \right). \qquad (4.17)$$

If $r = (R_1 + R_2)/2$, then

$$V_1 = \frac{1}{e}\left(TE\frac{R_2}{R_1} - KE \right); \qquad (4.18)$$

and

$$V_2 = \frac{1}{e}\left(TE\frac{R_1}{R_2} - KE \right). \qquad (4.19)$$

If $R_2 > R_1$, then the inner hemisphere's potential corresponds to V_1, and the outer's to V_2. Equations (4.18) and (4.19) can be used to find the relationship between ΔV, the potential between the hemispheres, and TE:

$$\Delta V = \frac{TE}{e}\left(\frac{R_2}{R_1} - \frac{R_1}{R_2} \right). \qquad (4.20)$$

For the present analyzer, which has inner radius of 3 inches and an outer radius of 5 inches, the above results gives $\Delta V = 1.067(TE)$. In practice, however, contact potentials and other effects alter this ideal situation, and as a result the operational equation for the present analyzer is $\Delta V = 1.087(TE) + 0.95$.

When it is necessary to scan over a range of electron energies, two methods

exist to accomplish this. The first method varies the transmission energy. This method cannot be used in quantitative work, however, as the brightness of the electron beam (see equation 4.25) varies with transmission energy. The second method keeps the transmission energy constant while changing the potential on the entire analyzer, thus bringing the energy of the electrons produced in the field-free region to that of the analyzer.

As an example calculation for a typical situation, suppose it is desired to observe photoelectrons having a kinetic energy of 5 eV with the analyzer set for a transmission energy of 5 eV. Then,

$$V_{inner} = \frac{5\ eV\ x\ 1.667}{e} - \frac{5\ eV}{e} = 3.33\ V$$
$$V_{outer} = \frac{5\ eV\ x\ 0.600}{e} - \frac{5\ eV}{e} = -2.00\ V \qquad (4.21)$$

and the potential of the entire analyzer is set to V = (TE - KE)/e = 0 V.

In practice, however, the actual potentials required for electron passage differ from the theoretical because of the presence of contact potentials. These potentials arise when different types of metals contact each other, such as when a copper wire makes contact with an aluminum surface. The magnitude of the potential generated is approximately equal to the difference in the electronic work functions of the two metals.

Two quantities, generally, reflect the performance of a dispersive analyzer: the dispersion and the trace width. The ability of such an analyzer to separate electrons

with different kinetic energies depends upon its dispersion. The dispersion of the analyzer the amount by which the electrons' impact position, x, in the focal plane varies with a change in kinetic energy, E, for a given pass energy, E_0. This is given by the expression

$$D = \Delta x\left(\frac{E_o}{\Delta E}\right) \tag{4.22}$$

For a 180° hemispherical analyzer, the dispersion is $2R_0$.[42]

The trace width reflects the size of the impact spot on the focal plane caused by iso-energetic electrons with different initial angular distributions at the source aperture. If the impact position of an electron at normal incidence on the entrance aperture is R_0, then the angular dependence is given by[43]

$$R_0(1 + \delta) = R_0\frac{\cos^2(\Delta\alpha)}{1 + \sin^2(\Delta\alpha)} \tag{4.23}$$

where the displacement caused by $\Delta\alpha$ is $R_0\delta$. In a third-order approximation, equation (4.23) can be reduced to[43]

$$\delta = -2(\Delta\alpha)^2 \tag{4.24}$$

The trace width is, therefore, $2(\Delta\alpha)^2R_0$.

One figure of merit for a dispersive analyzer is the ratio of trace width to dispersion.[43] This figure of merit essentially gives the resolving power as function of

entrance angle, and is equal to $(\Delta\alpha)^2$ for a hemispherical analyzer.

Although the number of electrons passing through the analyzer described in this dissertation is very small, if high currents were needed then consideration of the maximum would be needed. The conservation of energy limits the amount of electron current which can pass through the analyzer. This can be cast in terms of the law of Helmholtz and Lagrange which states that for an electron beam traveling with energy E, differential area dA, and through differential solid angle $d\Omega$, the energy at point 1 is related to the energy at point 2 by[4] (Kuyatt and Simpson, 1967)

$$E_1 d\Omega_1 dA_1 = E_2 d\Omega_2 dA_2 \tag{4.25}$$

Casting this equation in terms of current, Kuyatt and Simpson reformulate the equation as[4]

$$\frac{B_1}{E_1} = \frac{B_2}{E_2} \tag{4.26}$$

where $B_i = dI/dA_i d\Omega_i$ is the electron "brightness." This equation shows the effect that accelerating or decelerating the electrons has on the transmitted current.

Space charge effects also limit the electron current which can pass through the analyzer, although this is not a problem for performing photoelectron spectroscopy with this analyzer as will be proved now. Simpson and Kuyatt show[4] that the maximum amount of current which can pass, in microamperes, is given by

$$I_{max} = 38.5\ E_{FWHM}^{\frac{3}{2}}\ (\frac{d^2}{l^2}) \qquad (4.27)$$

where E_{FWHM} is the theoretical resolution of the analyzer; d is the diameter of the apertures, and l is the distance between the apertures. For the present analyzer, with a 1 mm source slit (the position-sensitive detector's equivalent exit slit is not a limiting factor), the maximum current which can be transmitted is 4400 picoamperes, or 2.7 x 10^{10} electrons/second. This value normally is never reached in the present analyzer as the maximum number of electrons produced typically is on the order of 6000 per second.

The use of a position-sensitive detector (PSD) has many advantages over a single-detector spectrometer. The biggest advantage is that a PSD can simultaneously detect all of the electrons that pass through the analyzer, and this greatly reduces the amount of time needed to acquire a spectrum. If the number of detectors is N, the amount of information acquired per unit time can increase by a factor of N, although the actual increase is somewhat less than this in practice because fringing effects reduce the effective area of the detector. Reducing the collection time is important, because over long periods of time, potentials can drift and alter the spectrum. Moreover, if a dye laser is being used for photoionization, the power of the laser can decrease substantially over time and also change the appearance of the spectrum, or even preclude ionization.

For weak signals, such as when the spectrometer is operating at very low pass energies, a single detector analyzer is superior to one with a multichannel array. Here

we have to introduce a measure to reflect the trade-off between resolution and transmission. Dahl[44] proposed using a measure of "goodness", G, given by

$$G = TR, \tag{4.28}$$

where R is the resolution of the analyzer, and T is the transmission given by

$$T = \Omega A. \tag{4.29}$$

Here, Ω is the solid angle of the electron beam accepted, and A is the area of the entrance aperture. For a multichannel array with N channels,

$$G = TNR. \tag{4.30}$$

The largest number of channels that can be used is

$$N = \frac{\Delta E}{\Delta E_{FWHM}} = R\frac{\Delta E}{E}, \tag{4.31}$$

where E is the energy span of the analyzer. Hence, the goodness of an analyzer using a multichannel array is[44]

$$G = TR^2\left(\frac{\Delta E}{E}\right).$$

For a single-detector analyzer and a multichannel analyzer having the same resolution and "goodness," the transmission of the single-channel type is $E/\Delta E_{FWHM}$ times larger.[44]

To minimize weight, the analyzer is constructed entirely of aluminum. Alignment of the hemispheres is critical. To make the alignment easier, the hemispheres are positioned on a baseplate by means of precisely drilled holes into which are placed 1/16th inch sapphire balls. Matching holes on the hemispheres produce the alignment. The inner hemisphere has a radius of 3.00 inches (7.62 cm), and the outer hemisphere has a 5.00-inch (12.7 cm) radius.

The large gap produces distortions in the electric potential at the entrance and exit apertures if no correction is made. A practical solution is to make the apertures equipotential surfaces. The effect of this arrangement has been considered in detail by Herzog[45] and by Wollnik and Ewald. [46] For the present case, two circular plates are installed in the baseplate onto which the electrostatic lens and detector assemblies, respectively, are installed. The baseplate's potential is then matched to the mean potential within the analyzer to minimize the distortion. Field shunts were not used as they would introduce problems of complexity and restricted pumping speed in the area of the detector.

An innovative approach to solving the problem of fringing fields was recently reported.[47] This approach uses a printed circuit board as the baseplate with ten concentric, metal rings etched into its surface. A voltage divider chain joining the two hemispheres and connected to the rings establishes the necessary $1/r^2$ electric field.

Electrostatic Lens

In order to achieve the highest resolution, the spectrometer is operated at the lowest possible pass energy. To reduce the energy of the electrons to this pass energy, a

four-element electrostatic lens capable of energy retardation is employed as shown in Figure 5 and Figure 6. Fortunately, the degree of retardation is not normally severe, as the typical photoelectron energies produced by the HeI light are less than 15 eV, and the lowest practical pass energy of the spectrometer for routine analysis is approximately 5 eV, resulting in a maximum retardation ratio of three. Use of the Helmholtz-Lagrange law in the form[48]:

$$\sqrt{E_1}\, w_1\, \alpha_1 = \sqrt{E_2}\, w_2\, \alpha_2 \qquad (4.33)$$

where w_i is the aperture width and α_i is the angular spread, with the half-angle for the emitted photoelectron of 0.05 radians, indicates that the lens system must be capable of a magnification of about one.

In the present apparatus, a four-element electrostatic lens capable of pre-retardation is used, and is based upon a design of Wannberg and Sköllermo.[49] They show that retarding the electrons' energy much beyond a factor of three for this lens system causes the aberrations of lens to increase rapidly.

Pre-retarding the energy of the electrons, i.e., reducing the energy of the electrons before they enter the analyzer has a number of advantages. First, it increases the luminosity of the analyzer by a factor of $(E_f/E_i)^{1/2}$, where E_f/E_i is the ratio of the electrons' final energy to the initial energy.[49] An additional benefit of slowing the electrons before they are analyzed, as discussed earlier, is that greater resolution is attained at lower pass energies. The signal intensity, however, falls off approximately[50] as the square of the energy width, ΔE^2.

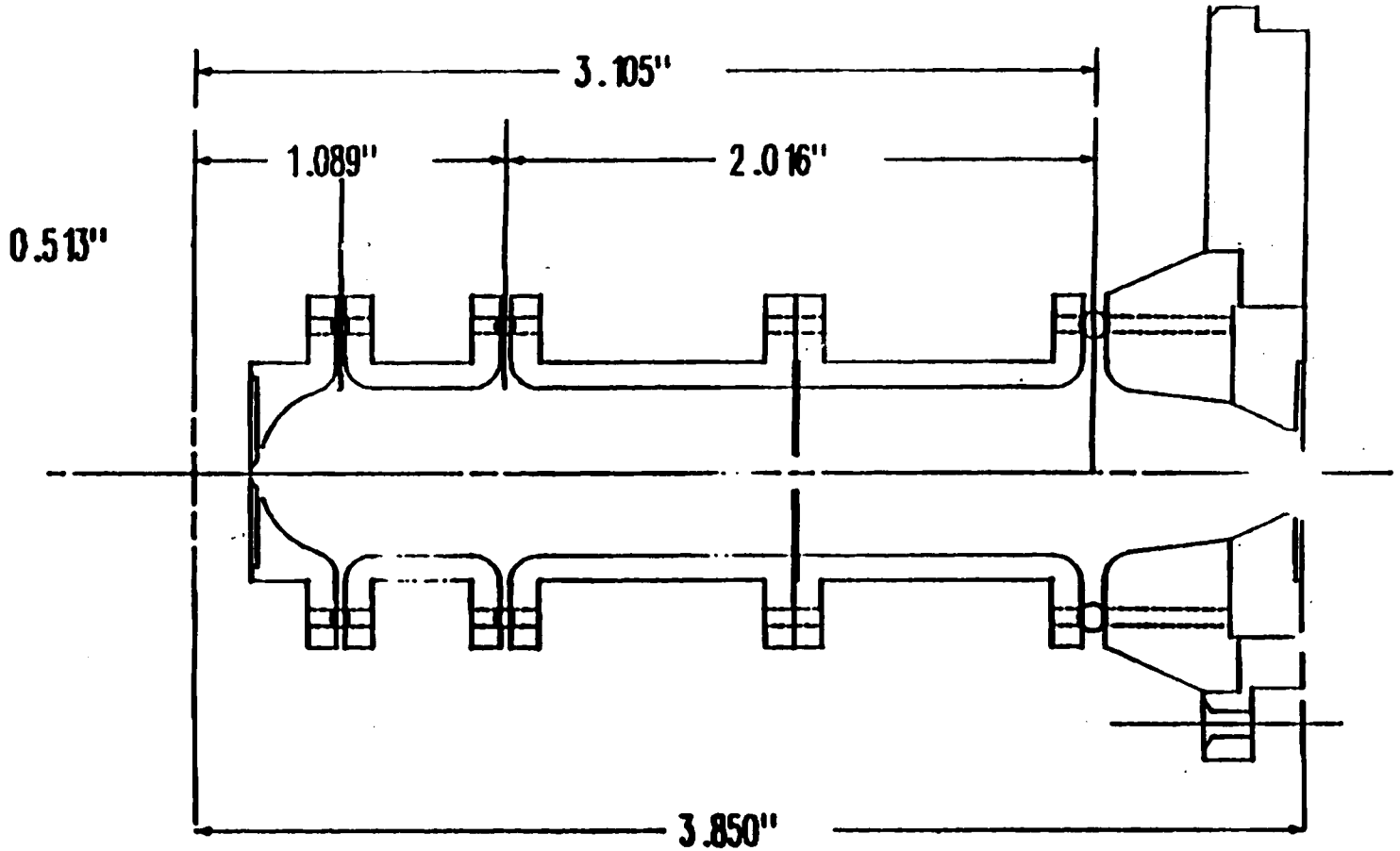

Figure 5. Diagram of the electrostatic lens used in the analyzer system.

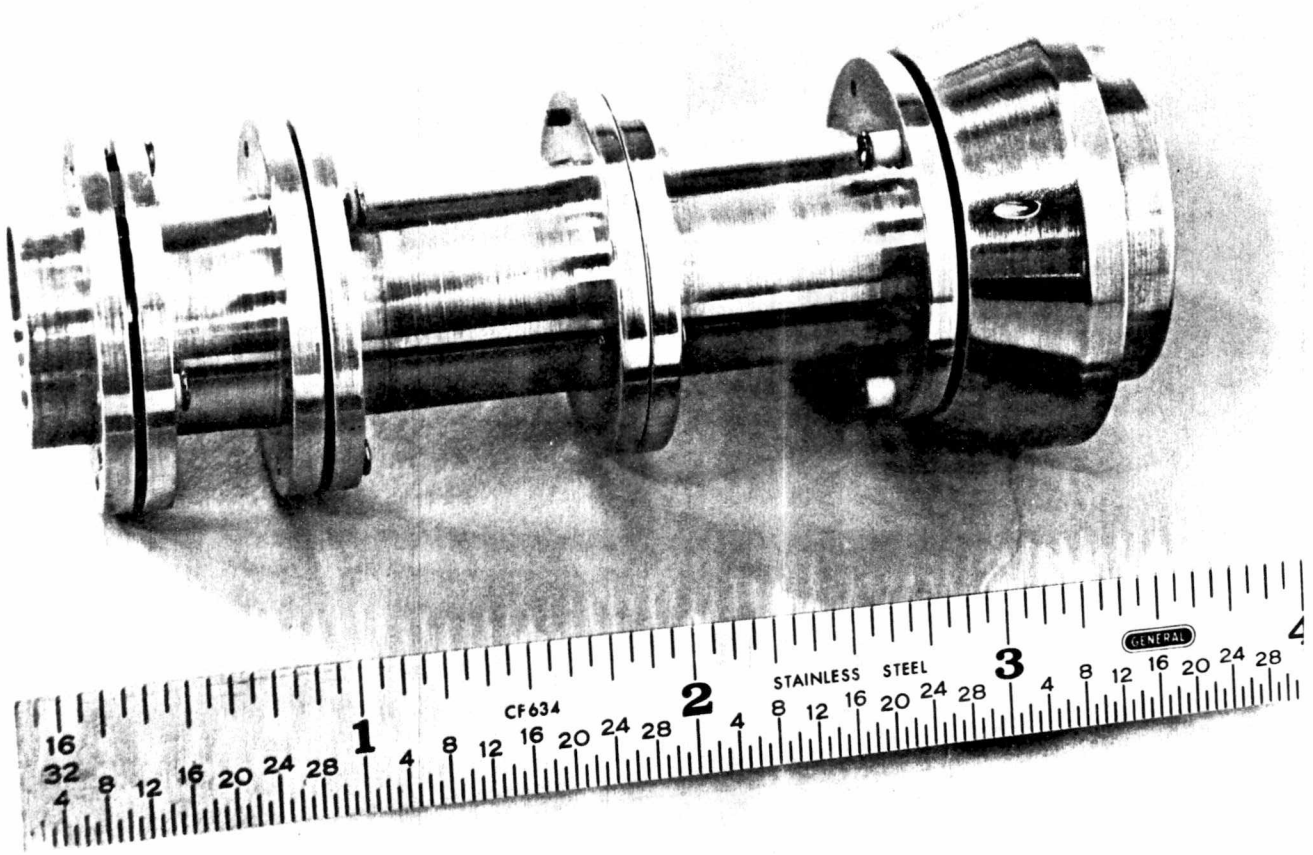

Figure 6. Photograph of the electrostatic lens.

The main purpose of the electrostatic lens, however, is to image the incident electrons at the entrance of the analyzer. Since it is nearly impossible to place the point of ionization at the object focal plane of the analyzer, which lies in a line determined by the exit slit and the center of curvature of the hemispheres,[5] it is necessary to have some means to focus the electrons at the entrance. The electrostatic lens' elements were machined out of cast aluminum, with the spacing between the elements maintained by 1/16th inch-diameter sapphire balls. The first element, containing the aperture with a nominal diameter of 5 mm, is at ground potential. Provision has been made to insert different-sized apertures into the first element. The second and third element form the focussing lenses. The third element is the longest and contains a 3.8 mm diameter field stop located midway between the ends. All of the lens' aluminum surfaces were coated with colloidal graphite to minimize surface charging. The fourth element, the entrance-to-the-analyzer aperture, is attached to the electrostatic lens, and forms the coupling potential between the lens and the hemispheres. The size of this aperture is 1.5 mm.

To obtain proper focussing, it is necessary to consider the energy of the incident electrons. Wannberg and Sköllermo[49] found the following equations provided one set of operating potentials for the lens:

$$\begin{aligned} V_2 &= 0.22E_i + V_r \\ V_3 &= 15.1E_i + V_r \end{aligned} \tag{4.34}$$

Because of the manifold factors influencing the focussing of electrons by the electrostatic lens, the operating potentials were arrived at empirically and their values

will be given later.

Power Supplies

Operating potentials were provided by a computer data acquisition board, a Microstar Laboratories model DAP™ 1200e/6, driving Kepco BOP power supplies. This board can acquire up to 16 channels of 12-bit data at 320 kHz, as well as simultaneously supply - with an analog output board - six 12-bit ±10 volt outputs. Once the analyzer operating parameters were determined, it was possible to pre-program the optimum potentials for a given expected electron energy.

Factors Affecting Resolution

Five major factors limit the resolution of the apparatus. As Dehmer and Dehmer[51] point out in their study of jet-cooled ethylene, the factors can be related to the FWHM, $\Delta E_{observed}$, by

$$\Delta E_{observed} \approx [\Delta E_o^2 + (\Delta E_{photon})^2 + (\Delta E_{Doppler})^2 + (\Delta E_{rotation})^2 + (\Delta E_{fields})^2]^{1/2}, \qquad (4.35)$$

where ΔE_0 is the analyzer's theoretical resolution; ΔE_{photon} is the photons' line width; $\Delta E_{Doppler}$ is the Doppler broadening term; $\Delta E_{rotation}$ is the broadening due to the rotational motion of the target molecules, and ΔE_{fields} is the term which incorporates the effects of stray fields.

First, let us consider ΔE_{fields}. These electromagnetic fields can affect the resolution either by directly acting on the electrons, or by acting through the instrumentation. In the first case, the forces on the electron are the electric force,

$$\vec{F} = q\vec{E} \tag{4.36}$$

and the Lorentzian force,

$$\vec{F} = q\vec{v} \times \vec{B} \tag{4.37}$$

For this analyzer, these fields were minimized by surrounding the entire analyzer with both grounded, electrostatic shielding and mu-metal shielding. In the second case, electromagnetic noise can be carried to the analyzer over the cables carrying the analyzer potentials. Here the analyzer potentials are affected, modifying the pass energy or the electrons' energy. To minimize this noise, all the cables were double-shielded, and the power-supply outputs incorporated low-pass filters.

Next, consider E_{photon}. Either a laser or an ultraviolet (UV) lamp, or both, are used to ionize the gases. Samson[52] showed that the pressure within the discharge capillary determines in part the line width associated with the emitted radiation, with the line width, i.e., ΔE_{phton}, varying proportionally from 3 meV to 5 meV over the typical operating pressure range of a 58.4 nm helium lamp.

A Quanta-Ray model DCRII Nd-YAG laser was used to produce the conditions necessary for MPI. The laser's fundamental 1.06 μm output was converted, either by sending it through frequency doubling and tripling crystals or by pumping a dye laser, to the desired wavelength. A laser has a much narrower line width (ΔE_{phton}) than the UV lamp with a typical value of ~ 0.2 meV.

$\Delta E_{Doppler}$ and $\Delta E_{rotation}$ can both be reduced by judicious choices of geometry and

analyte cooling. The Doppler broadening of an electron ejected with an energy ϵ from a molecule having a mass M, and at a temperature T is given by[2]

$$\delta\epsilon = 0.723\left(\frac{\epsilon T}{M}\right)^{\frac{1}{2}} \; meV \tag{4.38}$$

For argon at room temperature and excited by 21.22 eV photons, the Doppler width is 4.6 meV. Cooling the argon by supersonic expansion to 10K reduces the Doppler width to 0.85 meV. Rotational effects can be as large as 10 meV and also can be reduced by cooling.

The temperature of the gas entering the analyzer depends upon the pressure behind the inlet valve. As Fite[53] (1971) has shown, if the pressure behind the valve is low, the flow will be effusive, and the characteristics of the gas will be the same as that before it enters the chamber. For this condition to exist, the mean free path of the gas particles must be less than the size of the orifice through which they pass. On the other hand, if the mean free path is much greater than the size of the orifice, a free-jet expansion condition exists and the gas will cool adiabatically as it enters the chamber.

The gas-inlet system consists of a Lasertechnics pulsed gas valve crossed at right angles by the light beams (see Figure 7). This type of valve uses the piezoelectric effect in order to open and close the valve. This mode of operation is preferable to that using large, opposing electric currents or solenoids to open the valve in that the detrimental effect of large electromagnetic fields on low-energy electron trajectories is avoided.

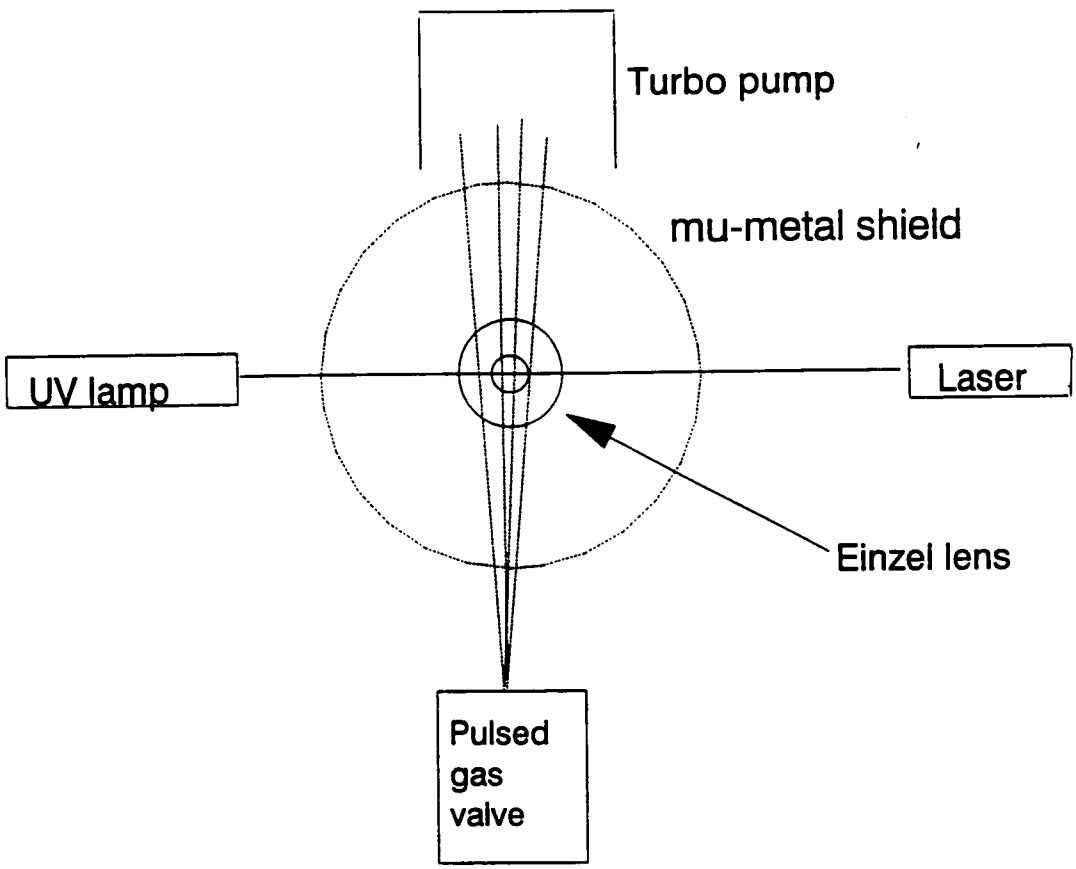

Figure 7. Schematic of ionization chamber as seen from above.

The valve can be operated in two modes. In the pulsed mode, the opening of the valve is timed such that the gas particles' arrival over the electrostatic lens coincides with the laser pulse. This mode not only permits the production of large gas densities in the interaction region with the light source without overloading the pumping system, but can also cool the gas substantially. Alternatively, the valve can remain open with the light continuously interrogating, in the case of continuous wave sources, the gas beam.

To keep the pressure in the system low, the inlet to a 200 liter/second turbomolecular pump is located directly in line with gas jet. This turbomolecular pump is backed by a 700 liter/minute rotary mechanical pump. The analyzer section is pumped by a 1,800 liter/second turbomolecular pump backed by a 200 liter/minute rotary mechanical pump.

The degree of cooling from a free jet expansion can be enormous. Fite has shown that for an adiabatic free expansion of a gas at constant entropy the following condition holds:

$$\frac{1}{2}mV^2 + c_pT = constant \qquad (4.39)$$

where m is the molecular mass; V is the velocity of the molecule; c_p is the specific heat of the gas at constant pressure; and T is the temperature.

If T_s is the temperature of the gas before expansion takes place (the stagnation temperature), then it is seen that the enthalpy of the stagnated gas transforms to the kinetic energy of the gas downstream from the orifice as

$$\frac{1}{2}mV^2 + c_pT = c_pT_s \tag{4.40}$$

Using the standard thermodynamic relations for an adiabatic expansion, Fite arrives at the following expression for the temperature of the downstream gas:

$$T = \frac{T_s}{1 + \frac{\gamma-1}{2}M^2} \tag{4.41}$$

where $\gamma = c_p/c_v$ and M is the Mach number of the expanded gas. For an ideal gas, c_p/c_v is 5/3.

The Mach number can be approximated by[52]

$$M \approx \left(\frac{\gamma + 1}{\gamma - 1}\right)^{\frac{\gamma+1}{4}}\left(\frac{z}{D}\right)^{\gamma - 1} \tag{4.42}$$

where z is the distance from the orifice, and D is the orifice diameter. Temperatures as low as a few degrees Kelvin are routinely achieved by such a method. In addition, noble gases can often be mixed with the analyte to cool further the analyte through collisions. This cooling allows inspection of spectra which might otherwise be obscured by the large number of rotational states at higher temperatures.

The density of gas particles at the ionization point also depends upon which of the two gas flow modes exist. As stated above, the gas emanating from an effusive source has the same characteristics as the gas behind the orifice, while the gas in a free

jet expansion has vastly different characteristics.

For effusive flow, Fite shows that the particle density downstream from the orifice is given by

$$n_b = \frac{n_s a}{4\pi L^2} \tag{4.43}$$

where n_s is the number density in the source; a is the orifice area; and L is the distance downstream from the orifice. For the present apparatus, the orifice diameter is 0.01 cm. Using a typical vapor pressure of an analyte of 40 torr, one obtains a particle number density of about 10^{19} cm^{-3} at 300K. The gas orifice is located 7.6 cm from the electrostatic lens aperture. Thus, the number density over the aperture is approximately 10^{10} cm^{-3}.

For supersonic flow, the density over the electrostatic lens aperture depends upon the specific heat of the gas, γ. Specifically, Fite shows that

$$\frac{n}{n_s}\left[1 - \left(\frac{n}{n_s}\right)^{\gamma-1}\right]^{\frac{1}{2}} = \left(\frac{2}{\gamma+1}\right)^{\frac{1}{\gamma-1}}\left(\frac{\gamma-1}{\gamma+1}\right)^{\frac{1}{2}}\frac{D^2}{L^2} \tag{4.44}$$

where D is the distance from the orifice at which the current density is uniform. For γ = 7/5,

$$\frac{n}{n_t} \approx \frac{1}{4}\frac{D^2}{L^2} \tag{4.45}$$

This leaves ΔE_{fields} for consideration. If one is not careful, this term can easily dominate the others and limit the achievable resolution at low electron energies. Because turbomolecular pumps are used in this system, a means to reduce the large amount electrical noise produced by them was needed. Low pass filters were constructed at the output of the DAP 1200e data acquisition card to reduce the noise on the lines providing the operating potentials. The filters in conjunction with double-shielded lines reduced the noise by 30 dB, cutting the noise on the lines from 1.5 volts to 50 millivolts. Further isolation was provided by commercial "surge suppressors" on the mains supply. These have rated 50 dB to 70 dB low pass filters. To supply a good conducting path to ground, thick copper braid connected the turbo pumps' housings to water lines.

With MPI, high laser power can create huge numbers of slow-moving ions. The electric field from this ion cloud can reduce the energy of the electrons leaving the ionization region.

Detection and Signal Processing

The position-sensitive detector (PSD) PSD consists of rectangular microchannel plates and a resistive anode. A photograph of the detector is shown in Figure 8 The useful area of the microchannel plates is 10mm x 53 mm. Approximately 1860

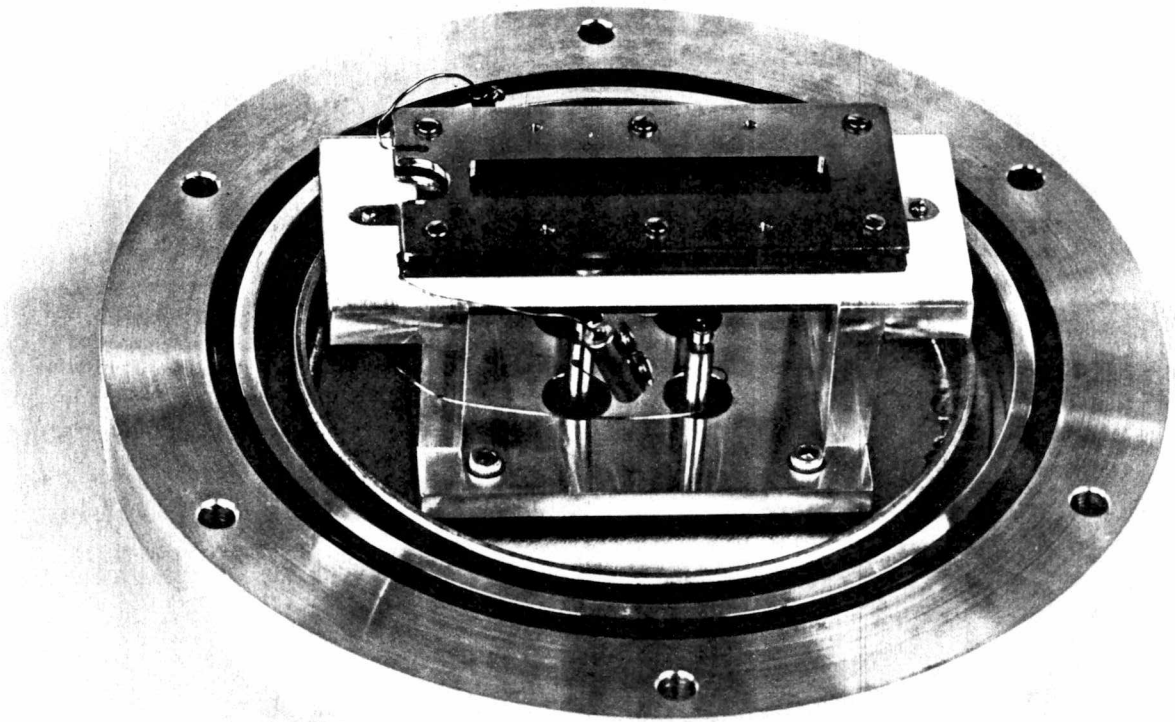

Figure 8. Photograph of the detector assembly.

channels, each with a diameter of 25 μm, can be found along the useful length of the microchannel plate. The channels are cut at a bias angle of 8 degrees, and the two plates are arranged such that the channels form a chevron when viewed from the side. This arrangement provides the highest gain, reducing the formation of ion clouds within the channels.[54] The resistive anode, having a uniform resistance of 240 kOhm across its length and located directly behind the microchannel plates, is the key for determining the impact position of the electrons.

Before the electrons arrive at the first MCP, they pass through a double-layer of 70 lines/inch, graphite-coated copper grids placed parallel to each other and separated by ~ 2 mm. The potential of these grids is set to the retardation voltage. After this, the electrons are accelerated toward the first MCP which has a potential of 25 volts applied to it.

The detection circuitry in conjunction with the resistive anode forms a distributed RC pulse-shaping network. For a network with neglible inductance, the voltage distribution along the network of length L is given by the differential equation:

$$\frac{d^2U}{dx^2} - R_oC_o\frac{dU}{dt} = 0 \qquad (4.46)$$

where R_o and C_o are the resistance and capacitance per unit length, with the total resistance and capacitance being $R=R_oL$ and $C=C_oL$. The solution to this equation is well known,[55] viz.,

$$U(x,p,T) = \frac{2Q_o}{C}\sum_{n=1}^{\infty} \sin(n\pi x)\sin(n\pi p)\exp(-n^2 T) \qquad (4.47)$$

where p is the impact position relative to the length of the anode, and T is the time in terms of the time constant, i.e., $T=t/RC/\pi^2$.

The charge, Q, delivered to the two ends of the wire is

$$Q_1(p,T) = \frac{2Q_o}{\pi}\sum \frac{\sin(n\pi p)}{n}[1 - \exp(-n^2 T)] \qquad (4.48)$$

$$Q_2(p,T) = -\frac{2Q_o}{\pi}\sum \frac{\sin(n\pi p)\cos(n\pi)}{n}[1 - \exp(-n^2 T)] \qquad (4.49)$$

An electron, striking the anode, creates two charge-pulses as described above to the ends of the anode. These pulses are amplified by two voltage-sensitive pre-amplifiers before the signal is sent to the time-to-pulse-height-converter (TPHC). The pulses have different rise times, and, therefore, the zero-crossing time of their filtered signals will be different, and given by[56]

$$t_{x1} \approx \frac{1}{2}R_o C_o (L - x)^2 - C_o R_o (L - x) + t_o \qquad (4.50)$$

and

$$t_{x2} \approx k - \frac{1}{2}R_o C_o x^2 - C_c R_o x + t_o \qquad (4.51)$$

where k is a filter-characteristic constant; x is the electron-impact position; L is the anode length; R_o and C_o are the anode resistance and capacitance, respectively; and C_c is

the load capacitance. The difference in crossover times after t_{x1} has been detected and after having been delayed by t_d, is given by the simple, linear expression

$$\Delta t_x = R_o(C_oL + 2C_c)x - \frac{1}{2}R_oC_oL(L + R_oC_o) + t_d \qquad (4.52)$$

A time-to-pulse-height converter (TPHC) converts the time-difference into a rectangular pulse whose amplitude is directly proportional to the time delay.

All of the position decoding circuitry can be found in a commercially available package. The Ordela, Inc. model AIM 206 position decoder contains the necessary amplifiers, pulse shaping and summing circuits, and a time-to-pulse-height converter.

After being processed the Position Decoder, the position information, in the form of a 1-microsecond-wide pulse with a height proportional to the position, is fed into a multichannel analyzer (Oxford Instruments, Inc, model PCA-III) which then stores the resulting spectrum.

The principle of operation can be more easily seen by looking at Figure 9 and Figure 10 showing the charge delivered to the ends as a function of position and time Figure 11 shows the difference between zero-crossing times of the two pulses. From these figures, it is obvious that the rise time of the pulses vary as impact position. Moreover, the overall response of the detection system is not truly linear, but approaches linearity for the middle portion of the detector.

Kopp[57] (1994), however, states that the response of the system is linear if the time constant of the resistive anode and associated cables is matched to the time constant of the pre-amplifiers via the empirical equation $R_oC_T/4 = t_A$, where R_o is the

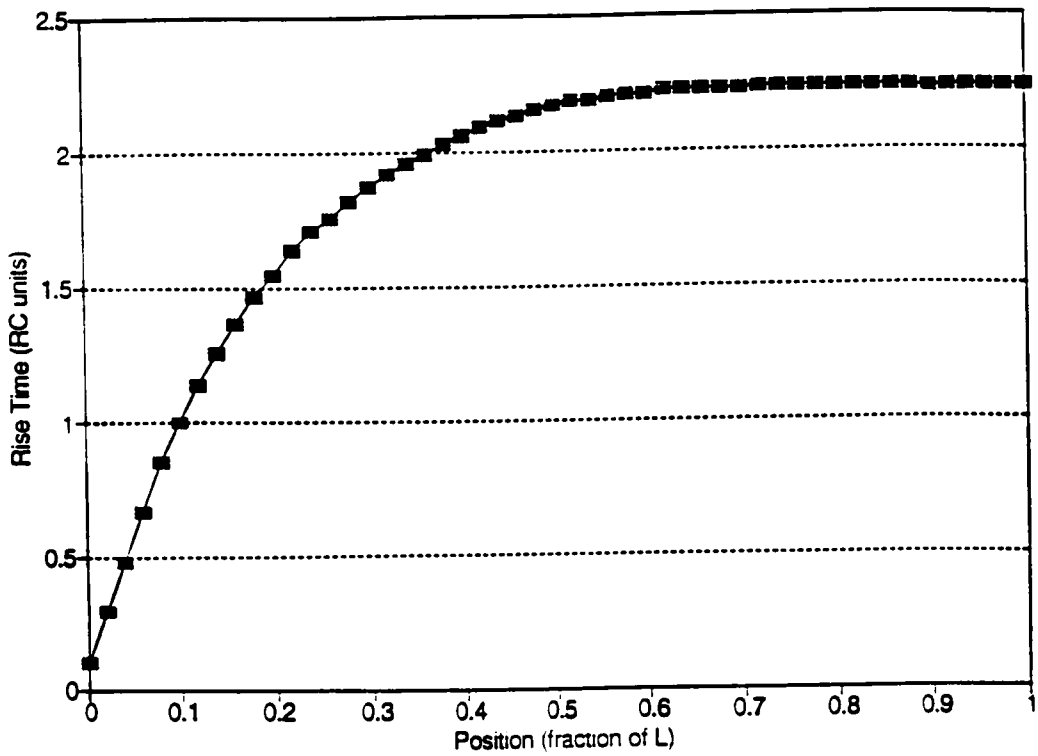

Figure 9. Rise time in pulses as a function of electron impact position.

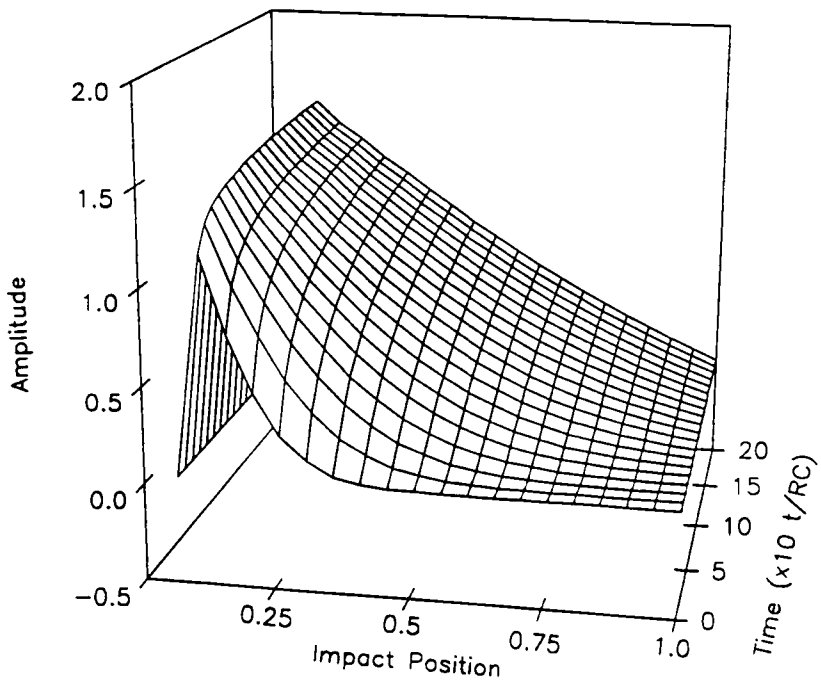

Figure 10. Three dimensional plot showing the response of the PSD at one end of the resistive anode as a function of impact position and time.

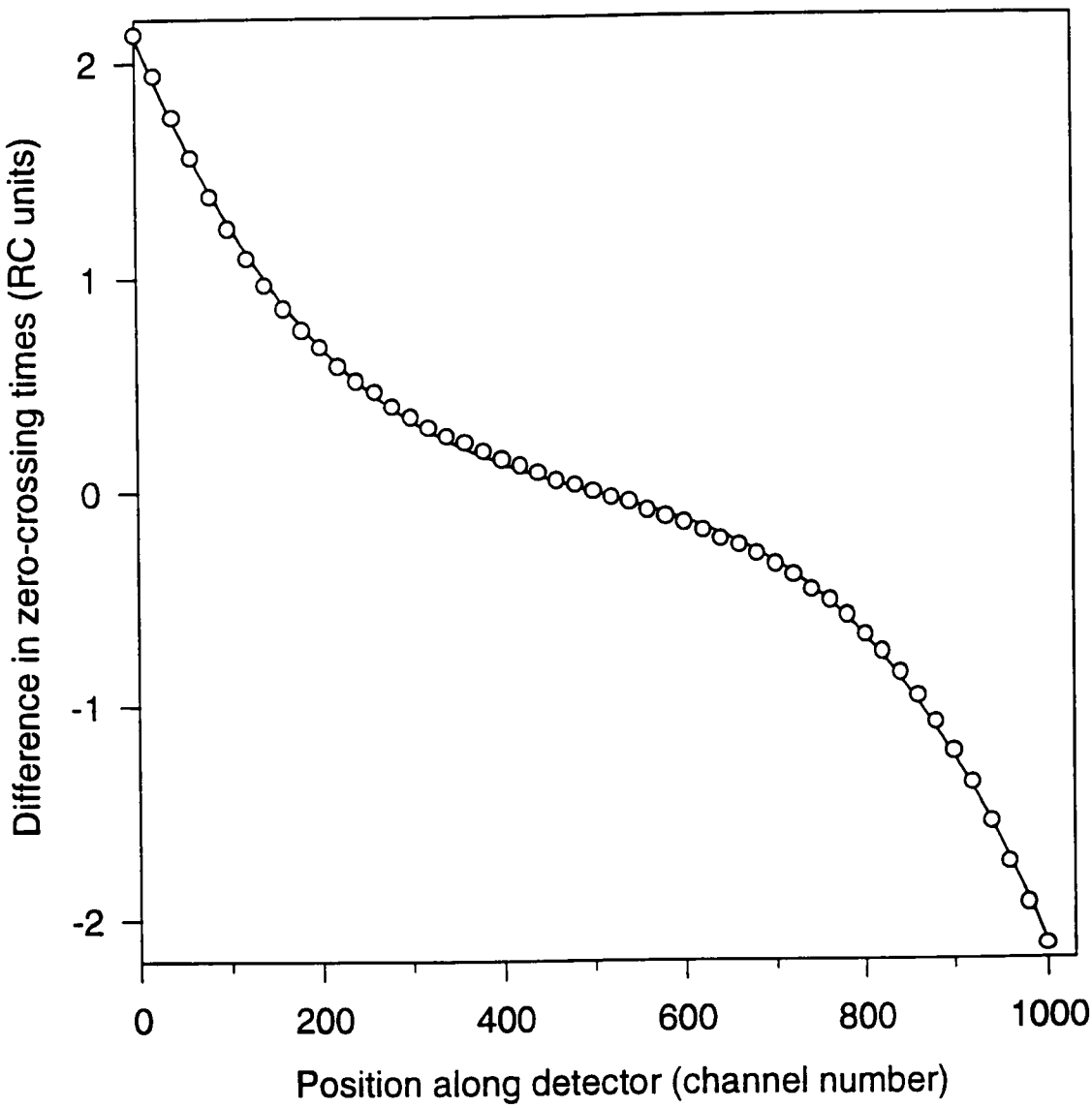

Figure 11. Difference in rise times as a function of electron impact position.

anode resistance; C_T is the capacitance of anode and cables; and t_A is the time constant of the pre-amplifiers. Matching the time constants is indeed crucial, but, as will be shown in a later section, further correction is needed to achieve an acceptable degree of linearity over the span of the detector.

CHAPTER 5

ANALYZER PERFORMANCE

One of the most difficult aspects of the development of an apparatus is getting it to work. The construction and operation of the analyzer described in this paper was no exception. First attempts to obtain any spectra with the UV lamp and the position sensitive detector were met with failure. In order to pinpoint which parts were not operating propertly, it was decided to dispense with ionizing gases with the UV lamp and directly introduce electrons into the analyzer. To this end, a small filament from a flashlight was positioned above the electrostatic lens' aperture. The enormous number of electrons produced by the heated filament traveled through the analyzer and struck the front plate of the microchannel assembly. The electrical current thus produced from the detector, through a picoammmeter, was more than ample to confirm that the analyzer was operating. This was a crude method since the voltage drop across the filament, in this case ~ 1 volt, gives a very broad electron-energy spread. When the position-sensitive detector was turned on, no signal was detected. The problem was traced to the fact that the microchannel plates had not been stored properly for over two years and, therefore, had deteriorated. Despite this, a set of detector-grade microchannel plates was substituted so that an initial calibration could be done until new image-quality plates arrived.

Once this this initial calibration was done and new microchannel plates received, further refinement was accomplished by photoionizing gases having well-

known characteristics and simple spectra. A large signal was needed since the sensitivity of the microchannel plates(MCP's) was unknown, and it was desirable to keep the applied voltages on the MCP to reasonable operating conditions, viz., less than 2000 volts across the plates. Furthermore, alignment of the UV lamp to the analyte beam was questionable. Therefore, it was decided to use laser-induced REMPI on xenon with a Nd-YAG-pumped dye laser instead of one-photon ionization with the lower-intensity UV lamp, because the alignment would be easier.

Initial MPI Studies

Xenon was chosen because it has a simple spectral structure. Xenon has two major, well-defined ionization potentials 12.130 eV and 13.436 eV corresponding to the j=3/2 and j=1/2 angular momentum states, respectively. These potentials are separated by 1.306 volts, providing a good inital test of the instrument's linearity. Xenon also has a low-lying intermediate state which can be reached with three photons of 440 nm wavelength, with only two additional photons needed to eject electrons from the two ^2P states.

The first photoelectron analysis of resonantly-enhanced multiphoton-ionization of Xenon was performed by Compton and co-workers[58] in 1980 who also used a spherical sector electron analyer.

For the present work, a 3 + 2 photon excitation of xenon was accomplished by illuminating it with 442 nm, 10 nsec laser light, produced by Nd:YAG pumped dye laser. Coumarin 440 was the dye used, with the grating set for an output wavelength of

440.88 nm. As stated earlier, three photons excite the ground-state electrons to the $6s(3/2)^0_{J=1}$ state, which corresponds[59] to the configuration $5p^5(^2P_{3/2}{}^o)6s$, where they are further excited into the continuum by two additional photons. The expected photoelectron energies were 0.66 eV and 1.97 eV for j=1/2 and j=3/2, respectively.

Since electron transmission through a hemispherical analyzer increases with higher pass energies, the analyzer was scanned first to detect the higher energy j=3/2 photoelectrons. These electrons were detected when the analyzer set to a pass energy of 1.85 eV. The energy bandwidth of the analyzer at this pass energy - viz., 0.3 eV - did not permit both peaks to be acquired simultaneously. Subsequently, the pass energy was lowered, and the j=1/2 peak was detected when the pass energy was set to 0.5 eV.

Since the resolution of the analyzer also depends upon the pass energy, it was necessary, in order to compare the relative intensities of the two peaks, to slow the j=3/2 photoelectrons to the pass energy of the j=1/2 electrons by adjusting the overall potential of the analyzer, i.e., the potentials were all made more negative by the same amount. A full-width, half-maximum value (FWHM) of 19 millielectron volts (meV) was obtained. (see Figure 12). This is somewhat higher than expected 6 meV theoretical resolution of the analyzer at a pass energy of 0.6 eV.

Contributions from Doppler broadening, 0.9 meV, and the laser linewidth, 0.02 meV, account for only a small portion of the FWHM. Most of the width, therefore, can be attributed to ΔE_{fields} and focussing error. As stated earlier, it is very difficult to eliminate stray fields, especially on the power supply lines. Typical voltages on the supply lines are on the order of 5 to 10 meV peak-to-peak. Using empirical formulas

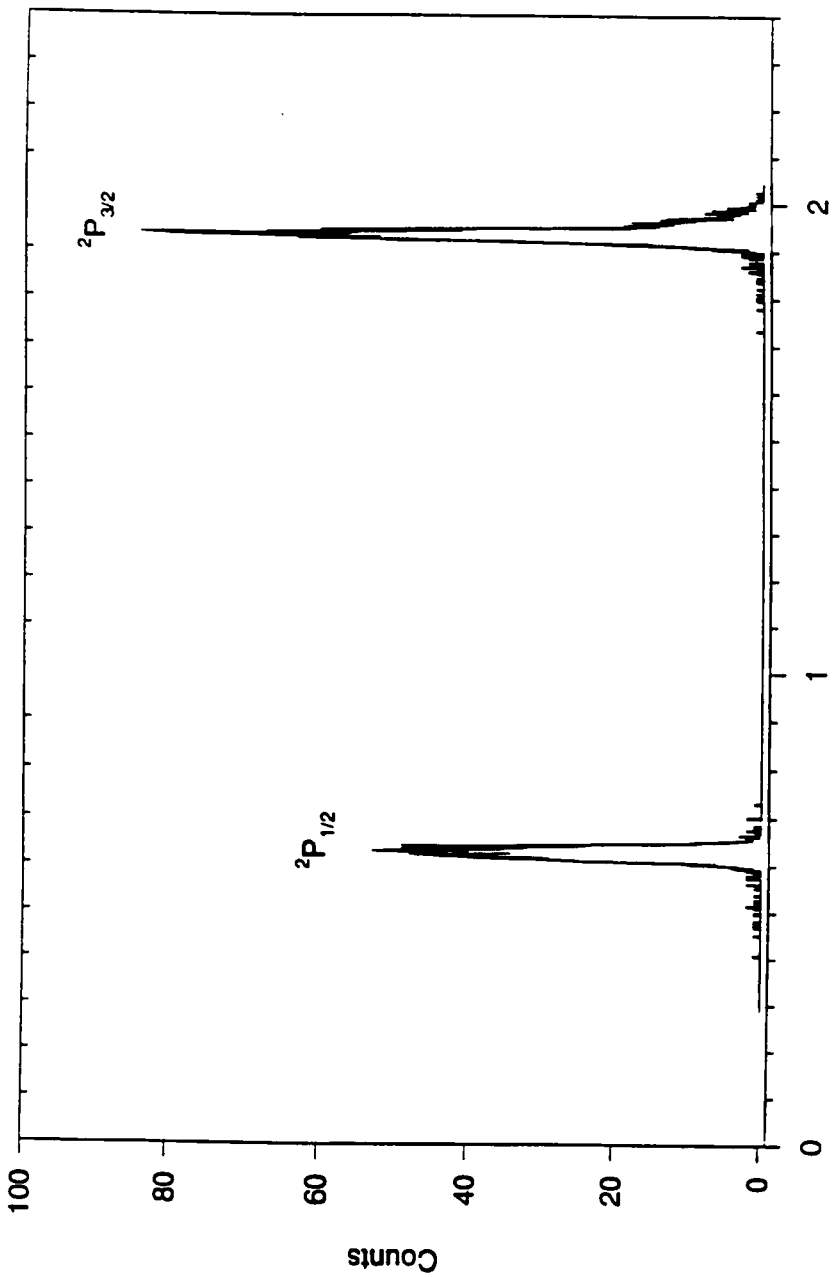

Figure 12. REMPI-PES of Xenon.

for the lens' voltages will produce satisfactory results, but to achieve the best focus, especially at very low electron energies (< 1 eV), requires the use of "look-up tables" stored in a computer. Another source contributing to width may be the a.c. Stark shift described in Chapter 3.

Next, the MPI photoelectron spectrum of nitric oxide was taken. Nitric oxide has been studied extensivley not only because of its simple electronic structure, but also because of its feature-laden spectrum. The electron configuration of nitric oxide is $(1\sigma)^2(2\sigma)^2(3\sigma)^2(4\sigma)^2(1\pi)^4(5\sigma)^2(2\pi)^1$. The ground state electronic state has been determined[60] (Jungen, 1970) to have a loosely bound electron having a wavefunction comprising a $3d\pi$ orbital mixed with a small amount $2p\pi$ character orbiting outside the filled core. This gives nitric oxide a more atom-like character, so that the single, orbiting electron's Rydberg nf and np series will contribute much more intensity to the spectrum than the lower-level nd and ns series (Carmen and Compton, 1989).[61] Because of this mixed nature of the ground state of nitric oxide, both even and odd numbers of photons can produce transitions to upper Rydberg states (Carmen and Compton, 1989).[61]

The first multiphoton ionization of nitric oxide, as stated earlier, by Johnson and co-workers[62] (1975) demonstrated that MPI greatly reduces the congestion in the nitric oxide spectrum. The same group showed later that the signal strength is greatly enhanced when the source illumination is in resonance with the aforementioned Rydberg series from two- and three-photon resonances through four-photon ionization of cold nitric oxide (Zakheim and Johnson, 1978).[62] This latter work was also

significant in that it was the first use of a supersonically cooled molecular beam in multiphoton ionization spectroscopy.

Subsequent work on nitric oxide has been extensive. Most notably, Compton and Miller[63] discovered the presence of zero-kinetic-energy electrons in 2+2 REMPI through the A $^2\Sigma^+$ state in their pioneering REMPI-PES study. The presence of these electrons has stirred much debate over their origin. Theories put forward include autoionization, valence-Rydberg mixing, and accidental double resonances (Compton and Miller, 1989).[63]

In much the same way, the present work produced electrons by 2 + 2 multiphoton ionization of nitric oxide through the A $^2\Sigma$state of nitric oxide. Again, Coumarin 440 was the dye used, but at a slightly higher energy, 451.33 nm. The spectrum revealed the expected, most-intense peak at 1.70 eV, corresponding to the v=0 level of the NO^+ ion. In addition, smaller peaks were observed at slightly lower energies which were assigned to the v=1 and v=2 levels, respectively (see Figure 13). [Although zero-energy electrons are also produced, these were not observed because there was no means to supply an external electric field to "coax" these electrons into the analyzer.] The presence of three peaks of known energy in a single "view" of the spectrum allowed a more precise estimate of the FWHM of the peaks than for the case of xenon. The FWHM was estimated to be 50 meV at a pass energy of 4.7 eV resulting in a calculated resolution of 90. Since the operational capability of the analzer in the multiphoton mode proved to have adequate sensitivity, it was decided to proceed to try to get the single-photon (UV lamp) section operational.

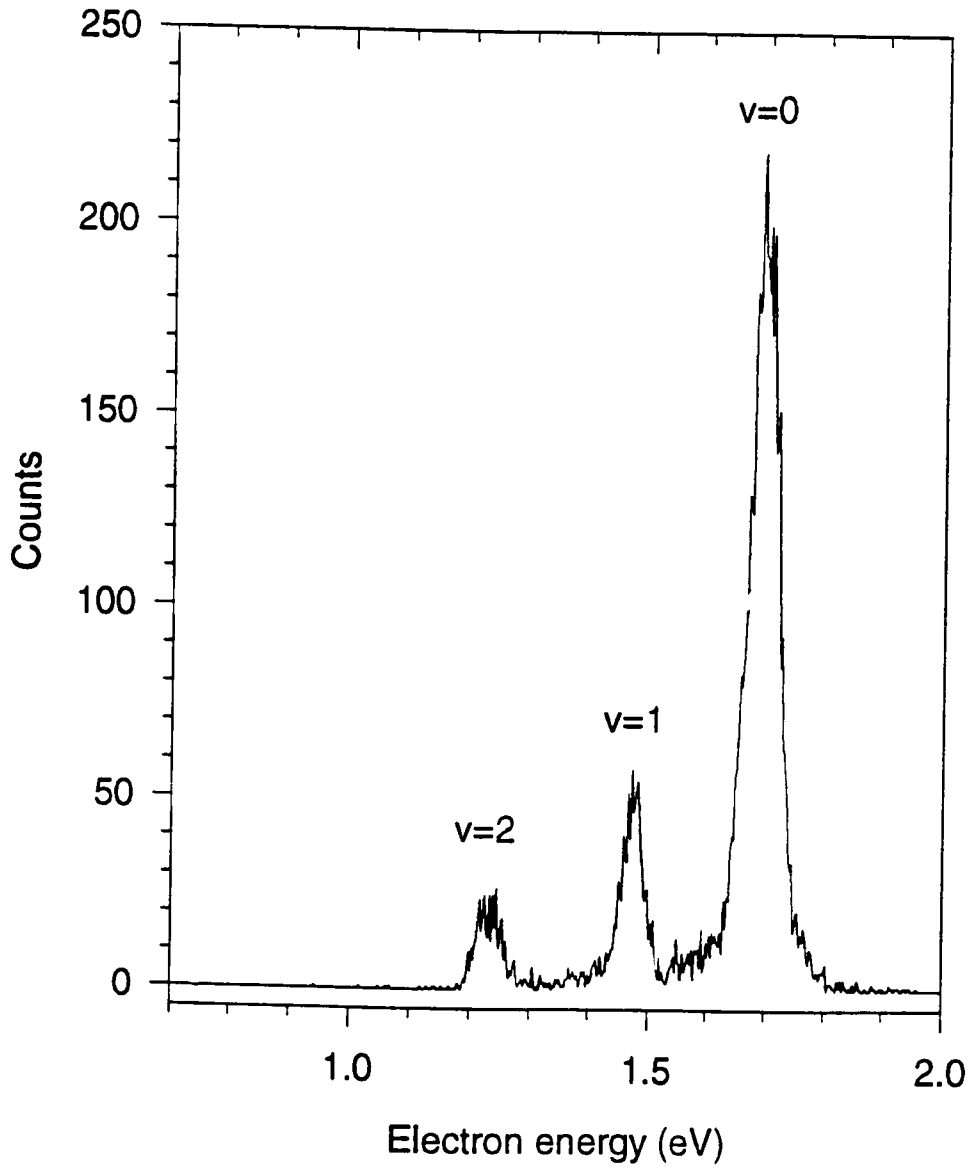

Figure 13. REMPI photoelectron spectrum of nitric oxide.

Single-Photon Spectra

To align the UV lamp so that ionization took place over the aperture of the electrostatic lens, a thin wire was suspended vertically so that the end of the wire was centered over the aperture, approximately 5 mm above the electrostatic lens. Illumination of the wire by the lamp caused photoemission of electrons, whose current was measured by a picoammeter. By monitoring where the current diminished, it was possible to place the light beam directly over the aperture.

The one-photon spectrum of argon supplied additional calibration information. Argon has an ionization potential of 15.759 eV with the other half of the ^2P doublet at 15.937 eV, thus not only providing electrons with a kinetic energy of 5.46 eV and 5.28 eV, just above those produced by the earlier REMPI studies, but also providing a good test of the resolution.

Varying the electrostatic lens' potentials revealed a substantial dependence of signal on these potentials. A nearly five-fold increase in signal was noted when the voltages were varied from 1.50 V and 75.0 V to 15.0 V and 160. V. Moreover, complete saturation and loss of resolution occurs when the electrostatic lens's potentials are substantially higher potentials than optimum. A surface plot of the response of the system signal to electrotatic lens voltages for the argon spectrum is shown in Figure 14 . It was found that the lens could accomodate electron energies which varied by a factor of four without serious degradation in resolution.

In order to determine the optimum lens settings, it was necessary to determine

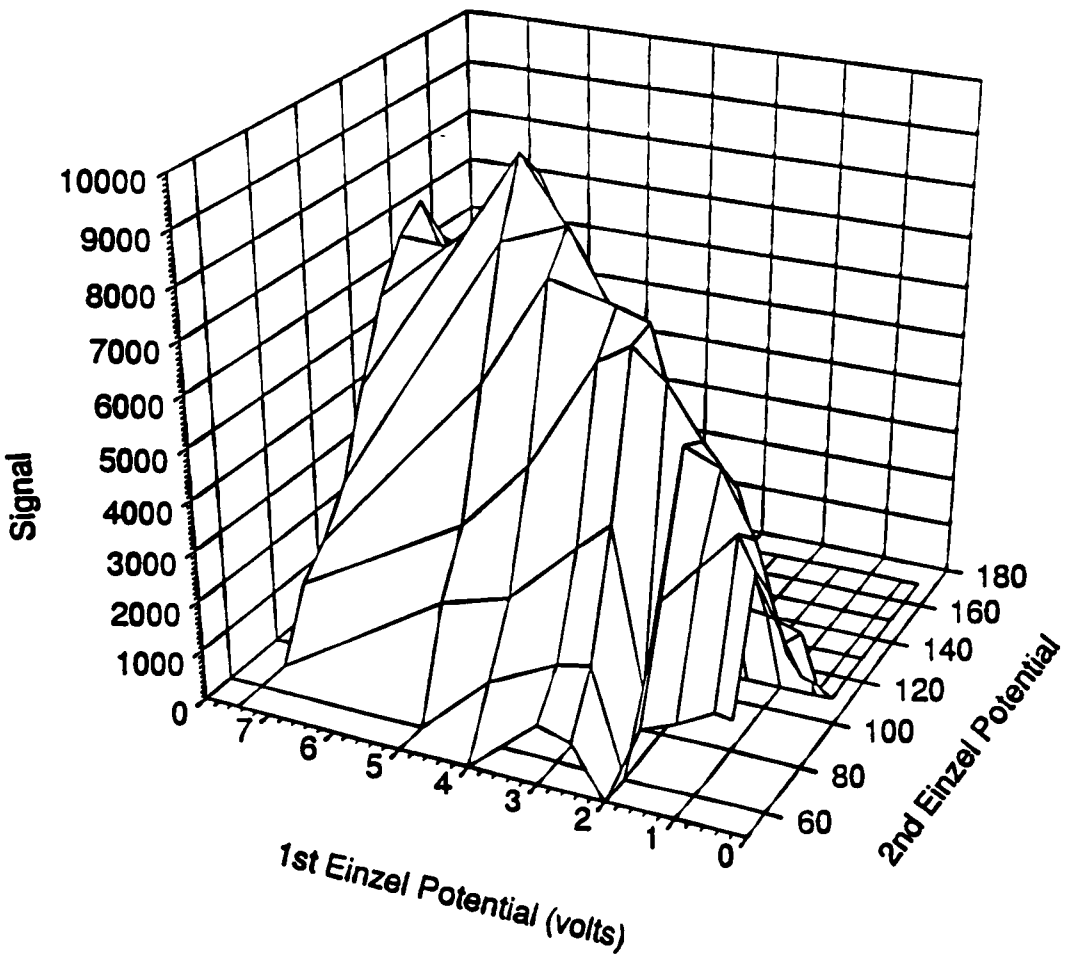

Figure 14 The effect of electrostatic lens voltages on the signal from argon photoelectrons.

the optimum settings at a few more electron energies so that enough statistics were gathered to permit chararcterization of the electron-energy versus the first- and second lens voltages. This is shown in Figure 15 . Taken together with the analyzer calibration curve (please see Figure 16), it was possible to set the potentials to the optimum without having to resort to experiment each time.

Determination of Resolution

Once these preliminary investigations were completed, it was necessary to resolve a major question - is it necessary to coat the the hemispheres with colloidal graphite to reduce surface patch potentials and thus increase resolution? When the analyzer was constructed, the hemispheres were deliberately left without a colloidal graphite coating.

Since the hemispheres are made of aluminum, the surfaces are essentially comprised of aluminum oxide, an insulator.

Fortunately, it was not necessary to take apart the analyzer and coat the hemispheres to make this determination. An analyzer, being used in Canada[64] (Westwood, 1992), of identical dimensions had been coated with graphite during its construction, and comparison to its resolution could be made.

The $a^4\pi_u$ band of oxygen was chosen for comparison for two reasons. First, the ionization for this band is in the neighborhood of 16 eV, allowing the use a modest pass energy of 5 eV without needing to retard the electrons' energy. Second, the band consists of many, closely-spaced peaks which allows examination of the detector's response over most of the useful length of the detector.

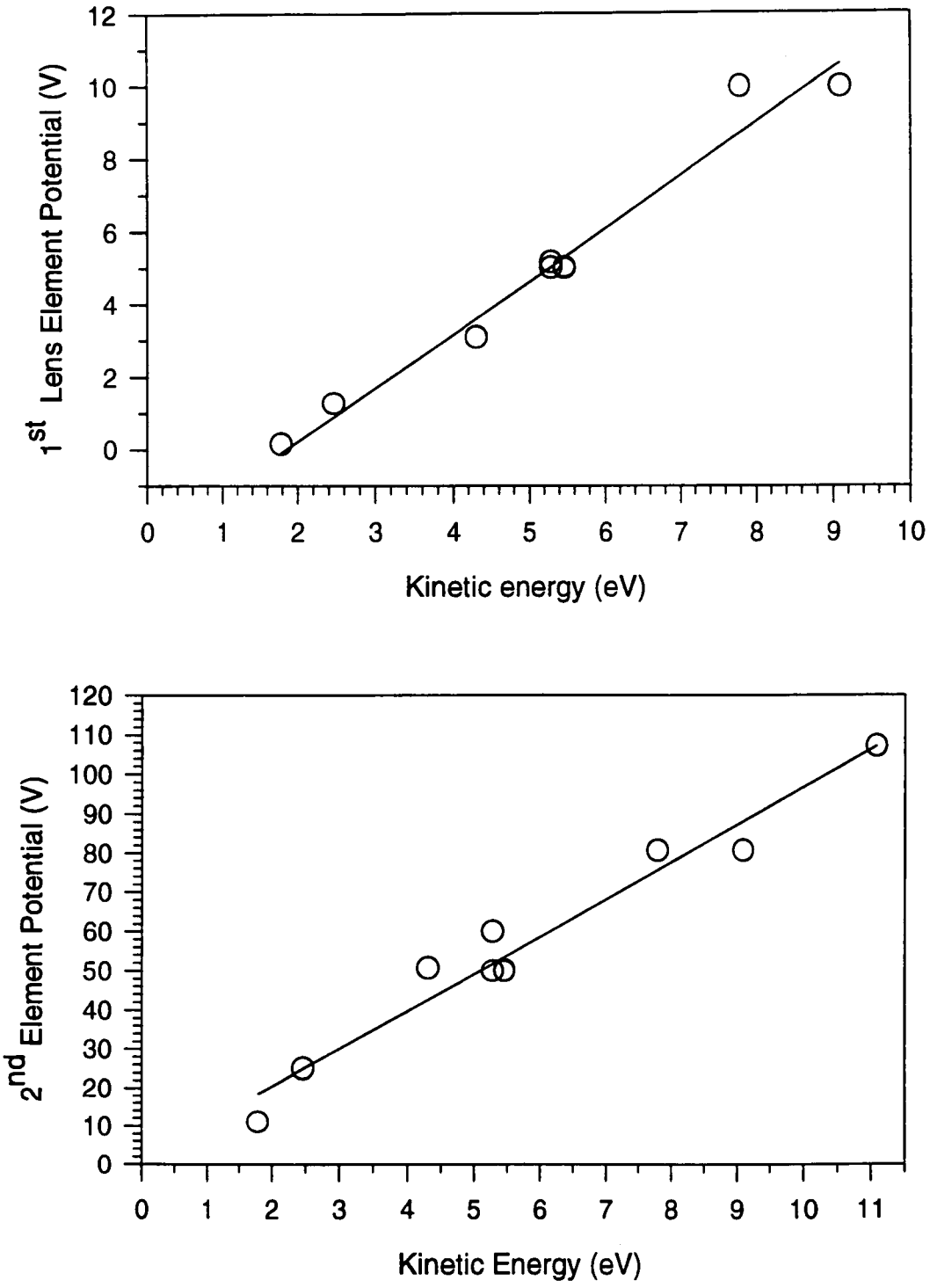

Figure 15. Calibration curve of electrostatic lens for optimum signals from different electron kinetic energies.

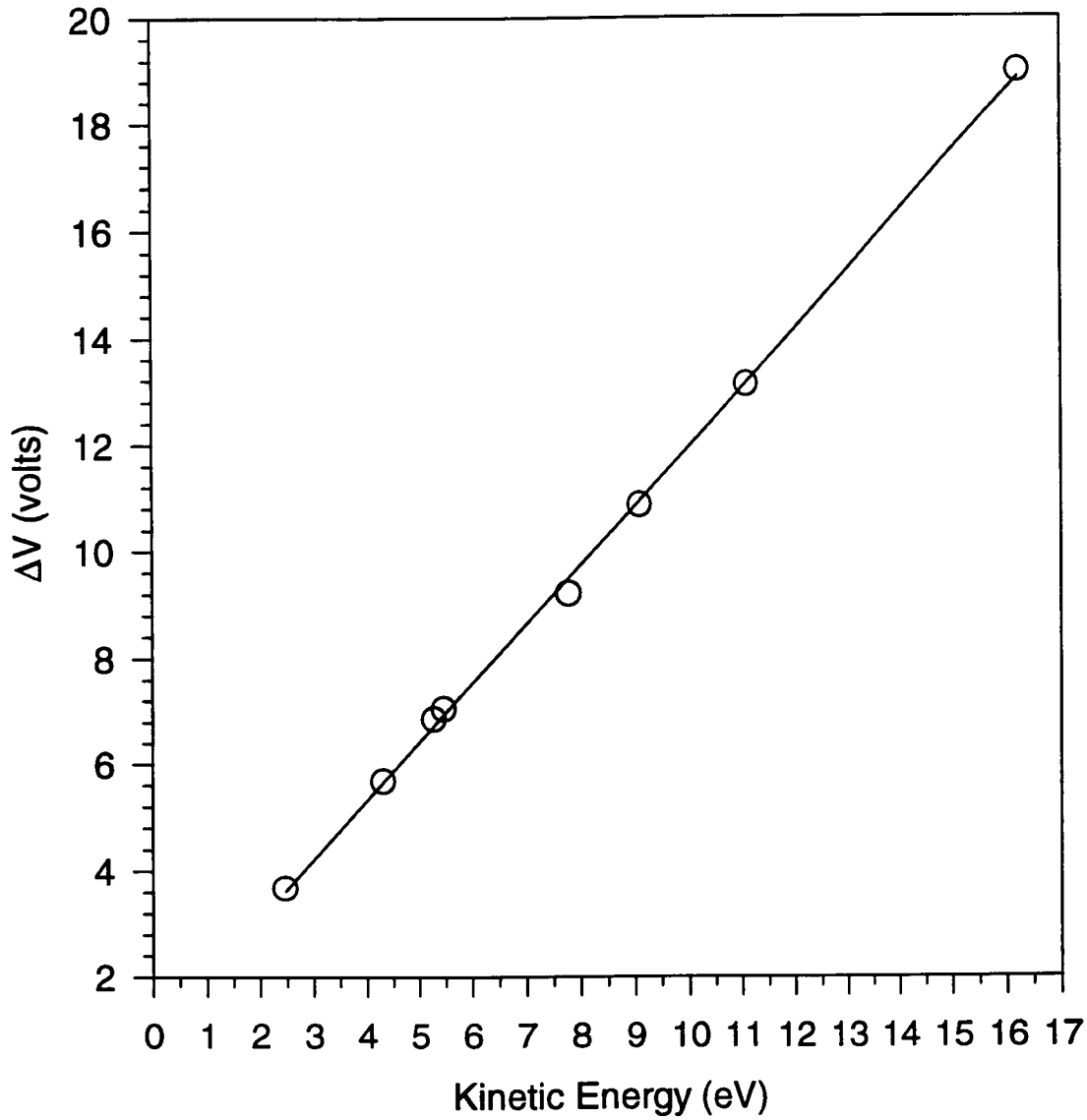

Figure 16. Calibration curve of hemispherical analyzer.

Surprisingly, the resolution was equal to that obtained by Westwood's group. Patch potentials for this apparatus apparently do not degrade the signal, and this is the case for all other spectra taken subsequently. A possible explanation is that the low electron current encountered - $\sim 10^{-17}$ amperes - is not suffieient to produce patch potentials of sufficient magnitude. Moreover, the large spacing between the hemispheres reduces the influence of these potentials on the electrons' trajectories. Despite this positive result, a more serious problem became readily apparent - the spacing between the second and third peaks was not the same as that for either between the first and second, or between the third and fourth. This problem was traced to the Position Decoder.

As stated earlier, the time constant of the Position Decoder must be matched to that of the detector and its cables. If it is not, then the response of the Position Decoder starts to assume third-order characteristics rather than the normal linear character. (Kopp, 1994). This was the case encountered as the Position Decoder had an initial time constant set to one microsecond, whereas the detector and cables had a nine microsecond time constant. The result of this can be easily seen in Figure 17 where the position output from the decoder is plotted against ΔV, which in turn is linearly related to the pass energy of the analyzer. A noticeable inflection occurs near channel 600 which corresponds to the midpoint of the detector.

The problem is more apparent when looking at more closely spaced lines. The $b^4\Sigma_g^-$ band shows this as it provides a longer progression with closer line spacings.

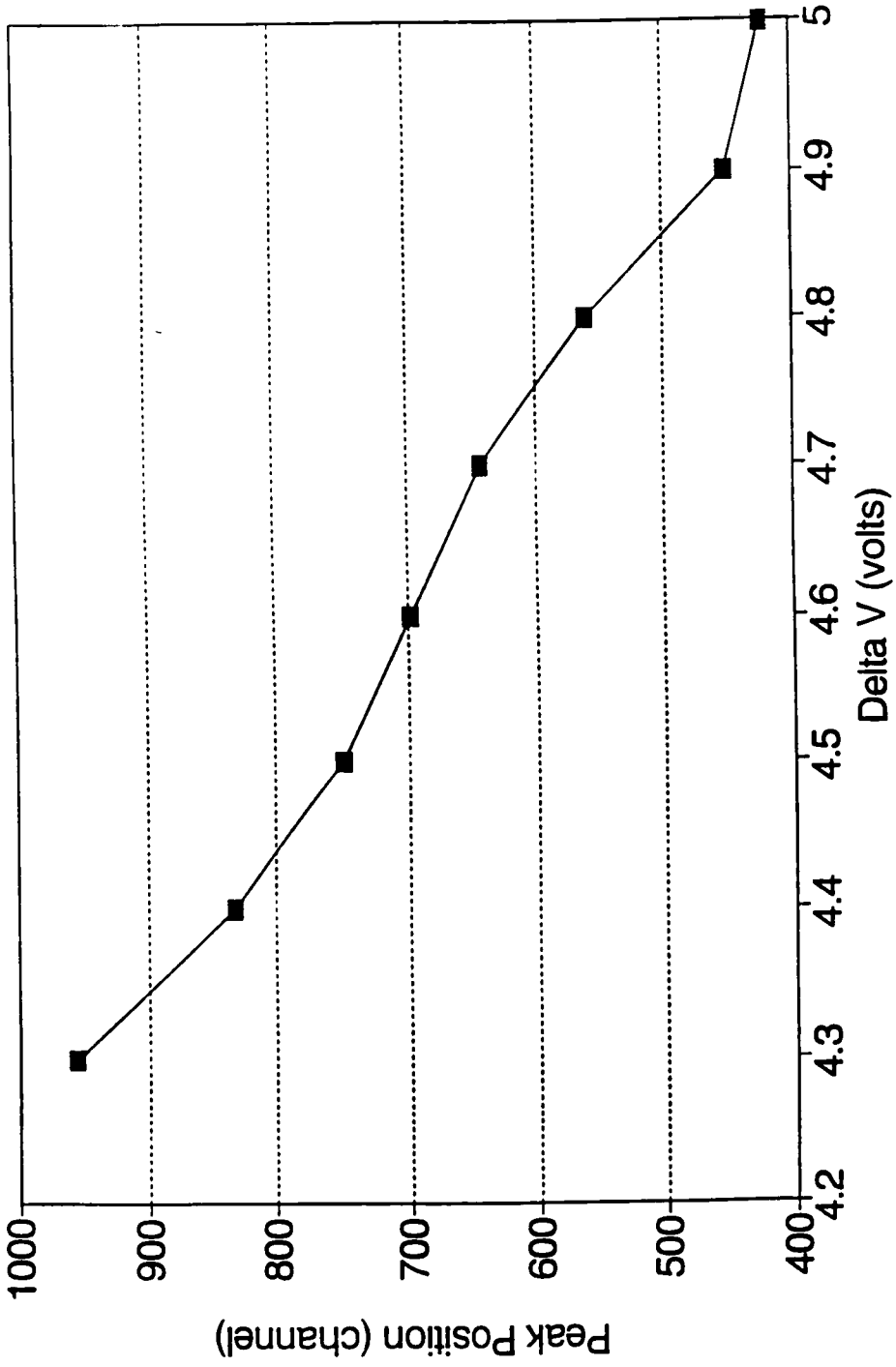

Figure 17. Indicated position as a function of electron energy.

After study of the situation by the manufacturer, it was decided to place a 10 kilohm resistor in parallel with the resistive anode so as to reduce the time constant of the system to that of the position decoder. But this new resistance was not sufficient to cause a linear response, and it was necessary to try a number of different resistors.

Trying a wide range of time constants revealed a peculiar effect. When the two time constants are grossly mismatched, peaks located in the low-energy half of the spectrum have greatly increased widths as compared to those in the upper half. In extreme cases, the peaks in the lower half are reduced to an amorphous signal resembling background noise. See Figure 18 for an example of this.

The proper time constant was found by using the two photoelectron peaks of xenon. The two lines arising from the spin-orbit coupling of the ^2P state of xenon were used as standards for the upper and lower halves of the detector response. Varying the time constant altered the widths of the lines. When the time constants matched, the two widths were nearly the same.

The time constant of the detector was reduced in two ways. First, the RG59 cables from the bias box to the detector were shortened from 130 cm to 26 cm. Shortening of the cables reduced the capacitance by 100 picofarads. Second, a resistance of 78 kilohm was placed in parallel with the detector, reducing the overall resistance of the detector.

Further examination of the oxygen $a^4\Pi_u$ band revealed grossly distorted peaks. This distortion was traced to the potential on the first microchannel plate altering the

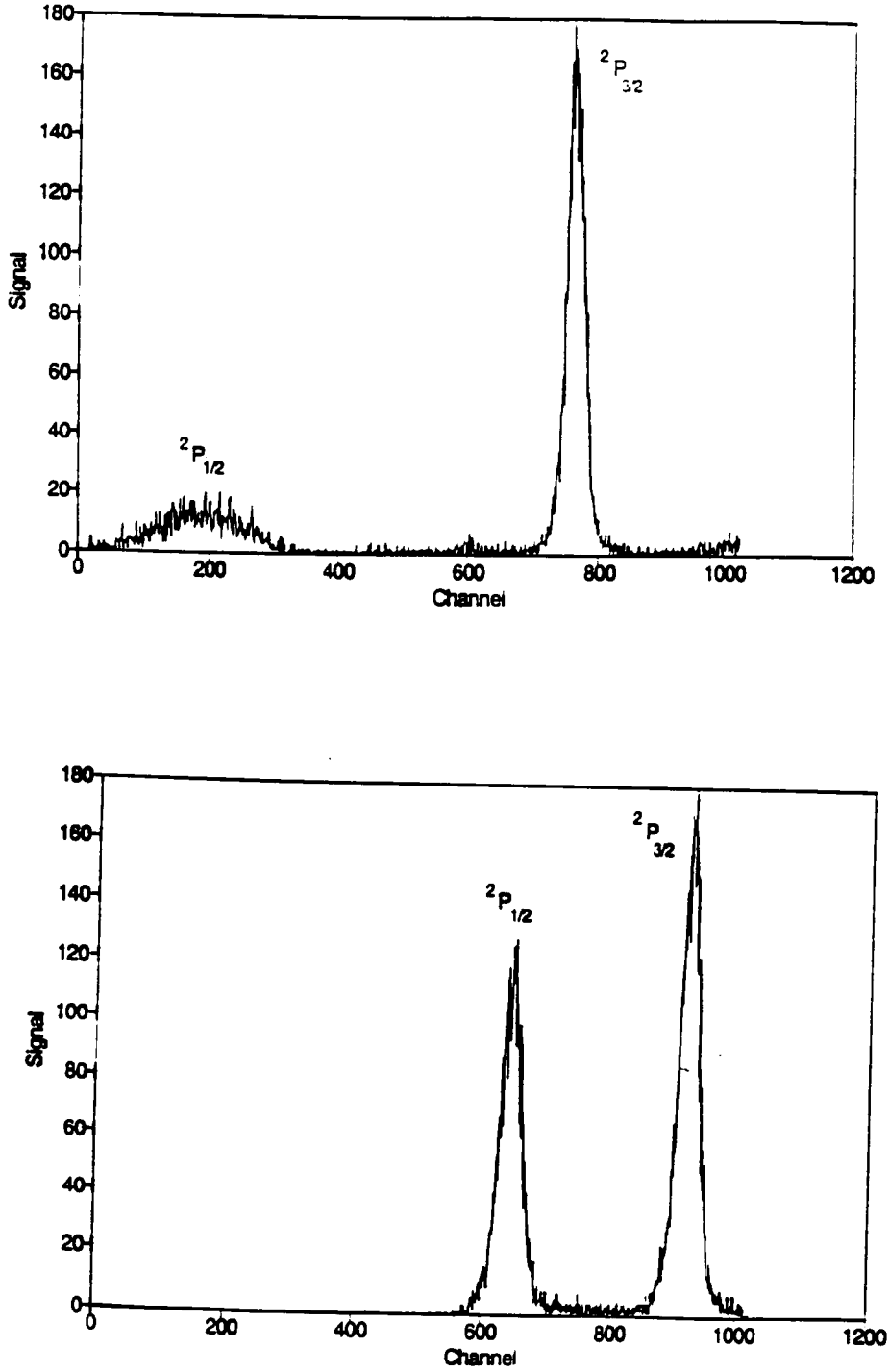

Figure 18. Xenon spectrum when time constants are grossly mismatched (top), and when time constants are matched (bottom).

path of the electrons as they exited the analyzer. Although the potential on the plate was only +138 volts when 2,000 volts was applied to the MCP assembly, this was sufficient to penetrate the double layer of 70-line-per-inch copper mesh. Reducing the voltage on the first microchannel plate to 25 volts resulted in a cleaner spectrum, but reduced the sensitity by a factor of six. Although this step improved the appearance of the spectrum, the peak spacing still was not correct.

In order to make the detector response more linear, a stepwise multiple regression was performed using the oxygen $a^4\Pi_u$ spectrum as a calibration source. Polynomials representing the detector channels up to the nineth order were systematically added as independent variables until the adjusted correlation coefficient showed no further improvement. The final model representing the corrected position, called the index, consisted of only three terms, viz.,

$$index = \alpha_0 + \alpha_1(channel) + \alpha_3(channel)^3$$

$$index = \alpha_0 + \alpha_1(channel) + \alpha_2(channel)^2 + \alpha_3(channel)^3$$

The coefficients obtained from this fit are given in Table 4.1. Applying thsee coefficients to the other bands of oxygen yields spectra with correct peak spacing. The fit nearly agrees with a polynomial regression analysis of the theoretical response of the position decoder which showed that a third-order polynomial fit the response with an R^2 of 0.9996 (please see Table 4-1 for a comparison)

The results of this regression of the theoretical response are shown in Figure 19.

Table 4-1. Comparison of regression results between experimental and theoretical PSD responses.

Coefficient	Experimental	Theoretical
α_0	1.0612	2.1137
α_1	-8.906×10^{-4}	-1.0302×10^{-2}
α_2	-	1.8223×10^{-5}
α_3	-4.9425×10^{-10}	-1.2149×10^{-8}
R^2	0.998	0.9996

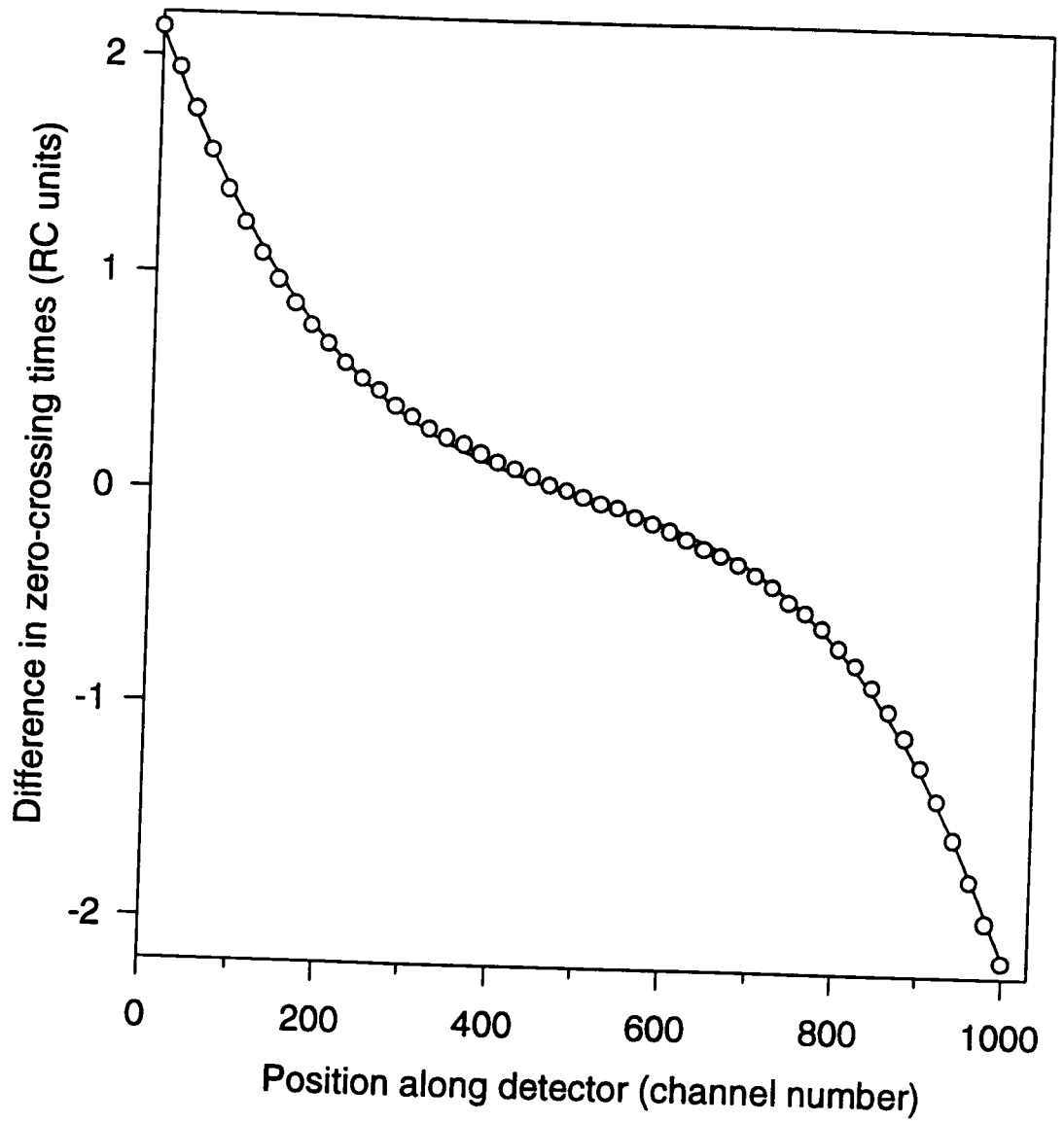

Figure 19. Fit of third-order polynomial regression to theoretical response of PSD. The circles represent the theoretical response, and the line is the regression result.

The improvement in the detector response can be easily seen by examining the residuals of the two cases (see Figure 20).

Once these corrections were made, it was decided to measure the resolution uniformity across the detector. This was done by varying the pass energy while monitoring the FWHM of the Xe $^2P_{3/2}$ peak. As can be seen in Figure 21, the resolution varies by about 20 percent across most of the detector, with deviations growing larger as the inner hemisphere is approached. Accordingly, it is estimated that the middle 90 percent of the detector is suitable for spectroscopic purposes. A model of the electric fields within the analyzer was made using the SIMION program and is shown in Figure 22 . Another noticeable feature of the $B^2\Sigma_g^-$ spectrum is the non-conformance of the relative peak heights to accepted values. A careful study[65] of the photoelectron spectrum of oxygen revealed that the vertical transition for this band occurs for v=6. In constrast, the present study has the vertical transition occurring for v=3. This discrepancy can be traced to the detector's non-uniform response over its length. This problem can be corrected and still retain the advantages of position-sensitive detection by "dithering" the signal over the detector. In this procedure, the potential of the analyzer is varied by an integer fraction of the number of channels in the data acquisition device; in this case, the fraction would be 1/1024. A computer would be needed to control this fine adjustment. The output from each of the 1024 channels is summed in the same number memory locations each time the potential is changed. The potential is scanned until the total width of the energy bandwidth at a particular pass energy has been traversed. The software included with the multichannel analyzer made

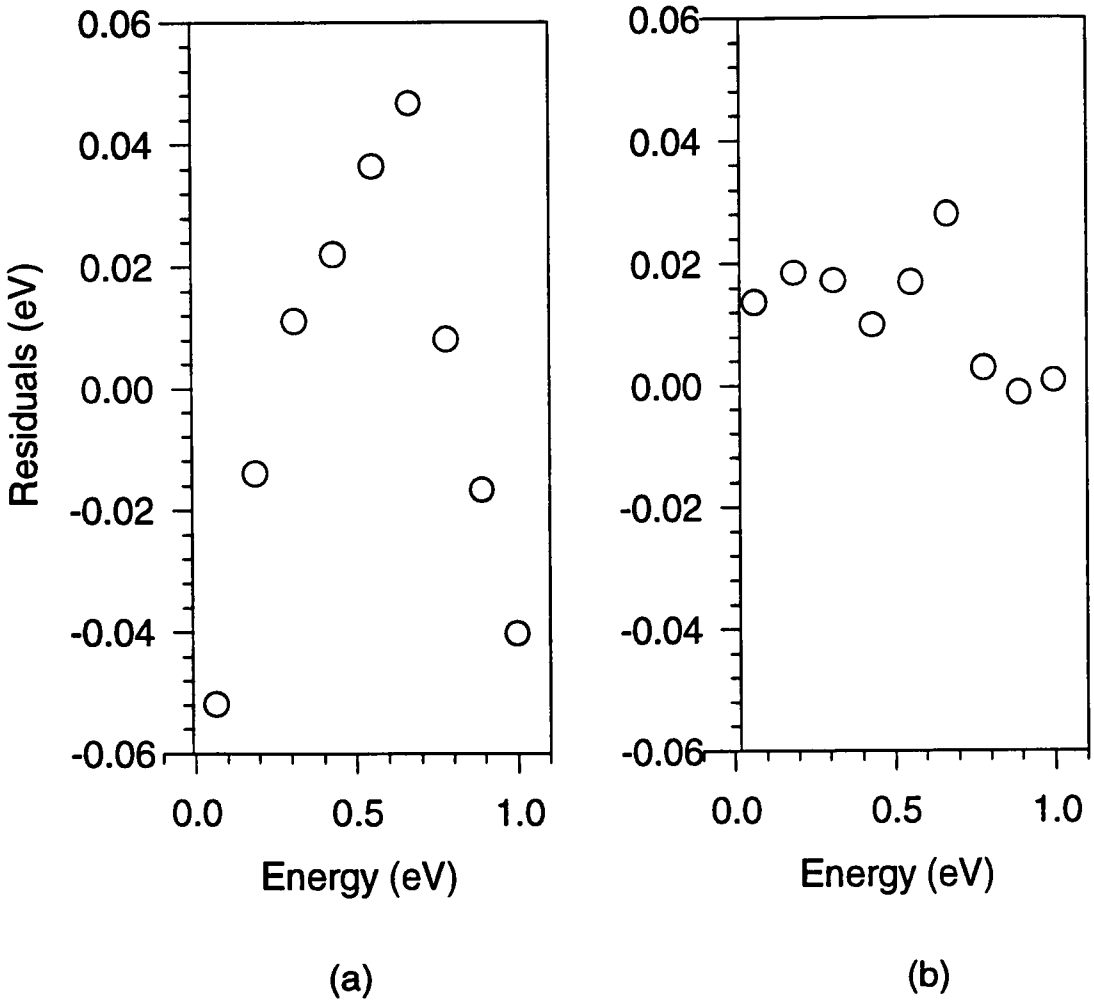

Figure 20. Energy residuals of the oxygen a $^4\Pi_u$ band: (a) before third-order polynomial correction applied, (b) after correction applied.

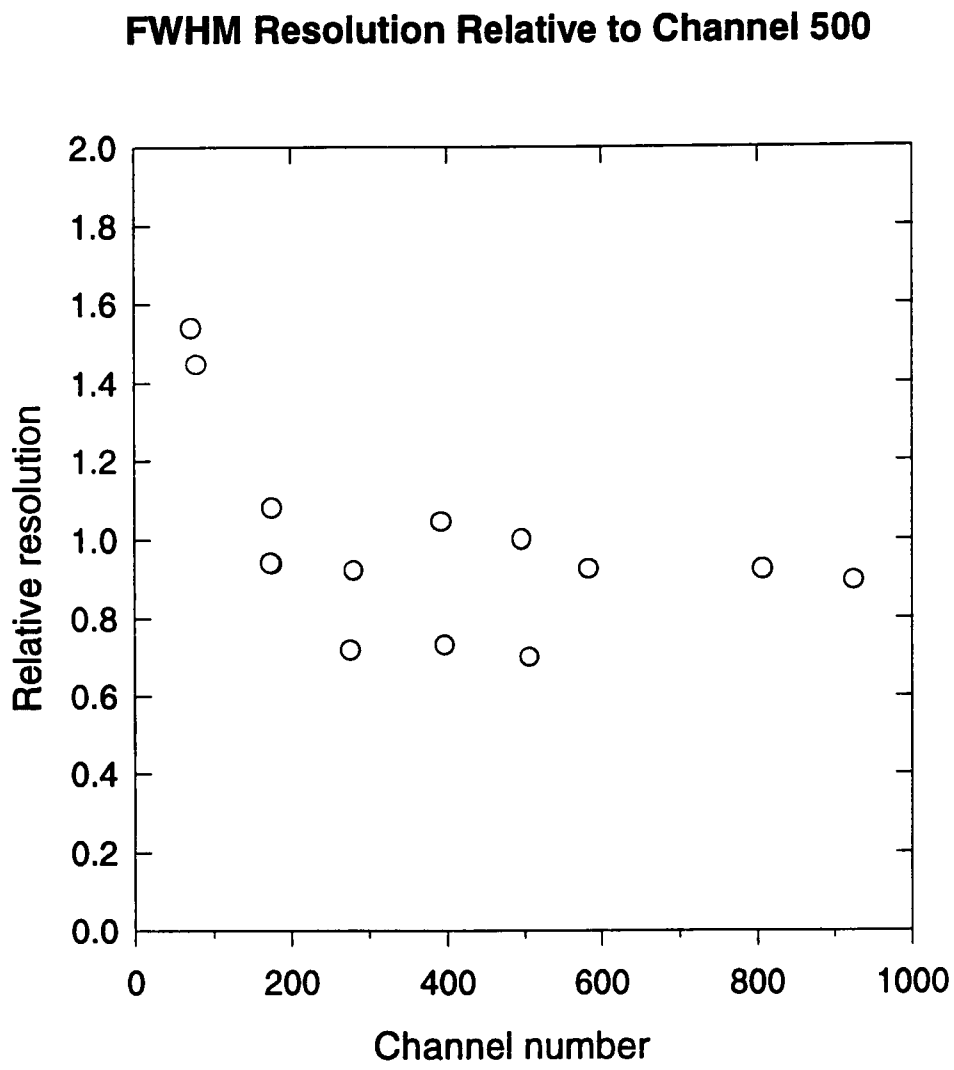

Figure 21. Variation in resolution across the detector relative to Channel 500.

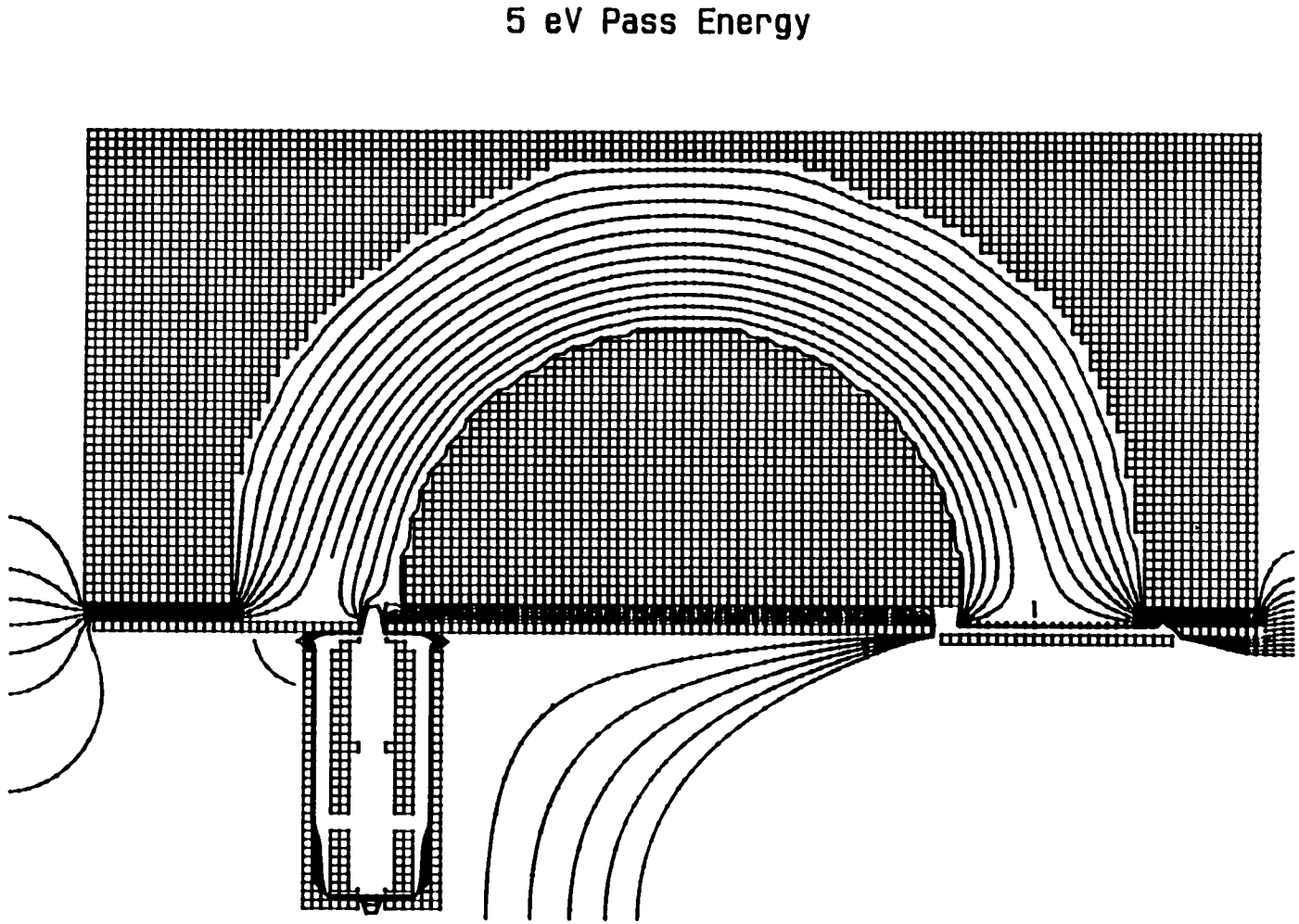

Figure 22. Electric fields within the analyzer as calculated by using the SIMION computer program. Contours are at 0.5 V intervals, and the pass energy is 5 eV.

development of this type of programming difficult. A new software version has been recently released by Oxford Instruments, Inc. which should make it easier to implement the dithering technique.

An additional benefit of noticing the non-linear response was a close examination of the operating conditions of the analyzer. Up to this point, the spectrometer was operated in the normal mode in which the potentials applied to the inner and outer hemispheres were calculated according to the condition that the midpoint between the hemispheres matched the energy of the incoming electrons. This is valid when the entrance aperture also coincides with the analyzer midpoint. The present design, however, has the entrance aperture offset by 19.4 mm toward the inner hemisphere. According to Joseph Swenson,[66] the designer of the analyzer, a computer model of the analyzer generated by SIMION indicated that the electrons experienced a "kick" towards the outer hemisphere as they entered the analyzer. The entrance aperture was thus offset to compensate for this. The model seems to be correct as the coefficient of the TE for the inner hemisphere, equation (4.16),

$$V_1 = \frac{1}{e}\left(TE(2\frac{r}{R_1} - 1) - KE \right), \qquad (5.3)$$

is consistent with a radius nearly the same as if the electron started at the midpoint, 3.80 inches versus 4 inches.

Work on a greater variety of electron energies further modified the optimum operating potentials of the hemispheres. Ionization of helium by the HeII line of the

UV lamp provided an additional calibration point for an electron kinetic energy of 16.22 eV. The HeII line is produced by the ^2P-^1S transition in ionized helium, and produces photons with an energy of 40.8 eV. By carefully reducing the helium flow in the lamp, it is possible to increase HeII light production. The dramatic increase in the HeII line is seen in Figure 23 where the 16.22 eV signal was monitored while changes in the lamp's helium flow rate were made. The flow rate was measured by measuring the pressure drop across a 0.2 mm diameter aperture with a Baratron™ capacitance manometer. Viscous flow existed throughout the measurement range, so the flow rate, in torr-liters/s, could be calculated by using the equation[67]

$$Q = \frac{9.13A(P_1 - P_2)}{1-(P_2/P_1)}\left(\frac{P_2}{P_1}\right)^{\frac{1}{\gamma}}\left[\frac{2\gamma}{\gamma-1}\left(\frac{T_1}{M}\right)\left[1-\left(\frac{P_2}{P_1}\right)^{\frac{\gamma-1}{\gamma}}\right]\right]^{\frac{1}{2}}$$

where P_1 and P_2 are the pressures across the aperture in units of torr; and A is the area of the aperture in cm^2; γ is the ratio of the specific heat at constant pressure, c_p, to the specific heat at constant volume, c_v; M is the gram-molecular weight; and T_1 is the temperature (in Kelvin) on the high pressure side, P_1.

The culmination of this characterization of the electron spectrometer was the test to determine its best resolution at a moderate pass energy (10 eV). Iodomethane (methyl iodide) was chosen as the target as it has two sharply defined peaks due to the spin-orbit splitting ($^2E_{1/2}$, $^2E_{3/2)}$ of the iodine. These peaks are separated by approximately 0.6 eV. The analyzer settings were as follows:

Electrostatic lens aperture: 1.0 mm

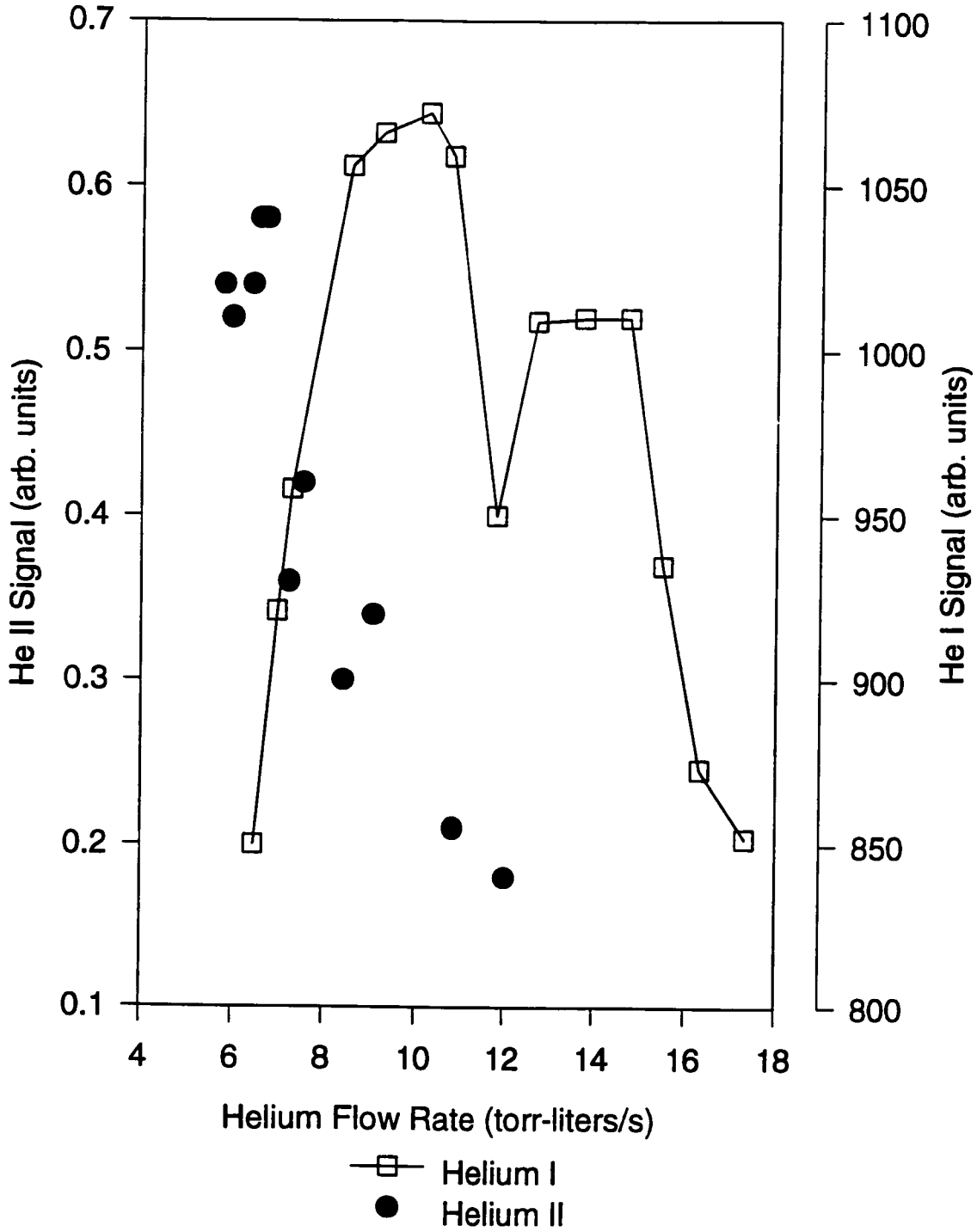

Figure 23. Production of He I and He II light as function of helium flow through the UV lamp.

Entrance slit potential: 0.000V

Hemispheres' potentials: 5.596, -7.528V

Electrostatic lens potentials: 8.05V (first lens), 107.05V (second lens)

As shown in Figure 24, both peaks are well resolved as well as the much smaller vibrational mode peaks. The full-width-half-maximum (FWHM) of the major peaks are 51.4 meV and 55.6 meV for the $^2E_{3/2}$ and $^2E_{1/2}$ states, respectively.

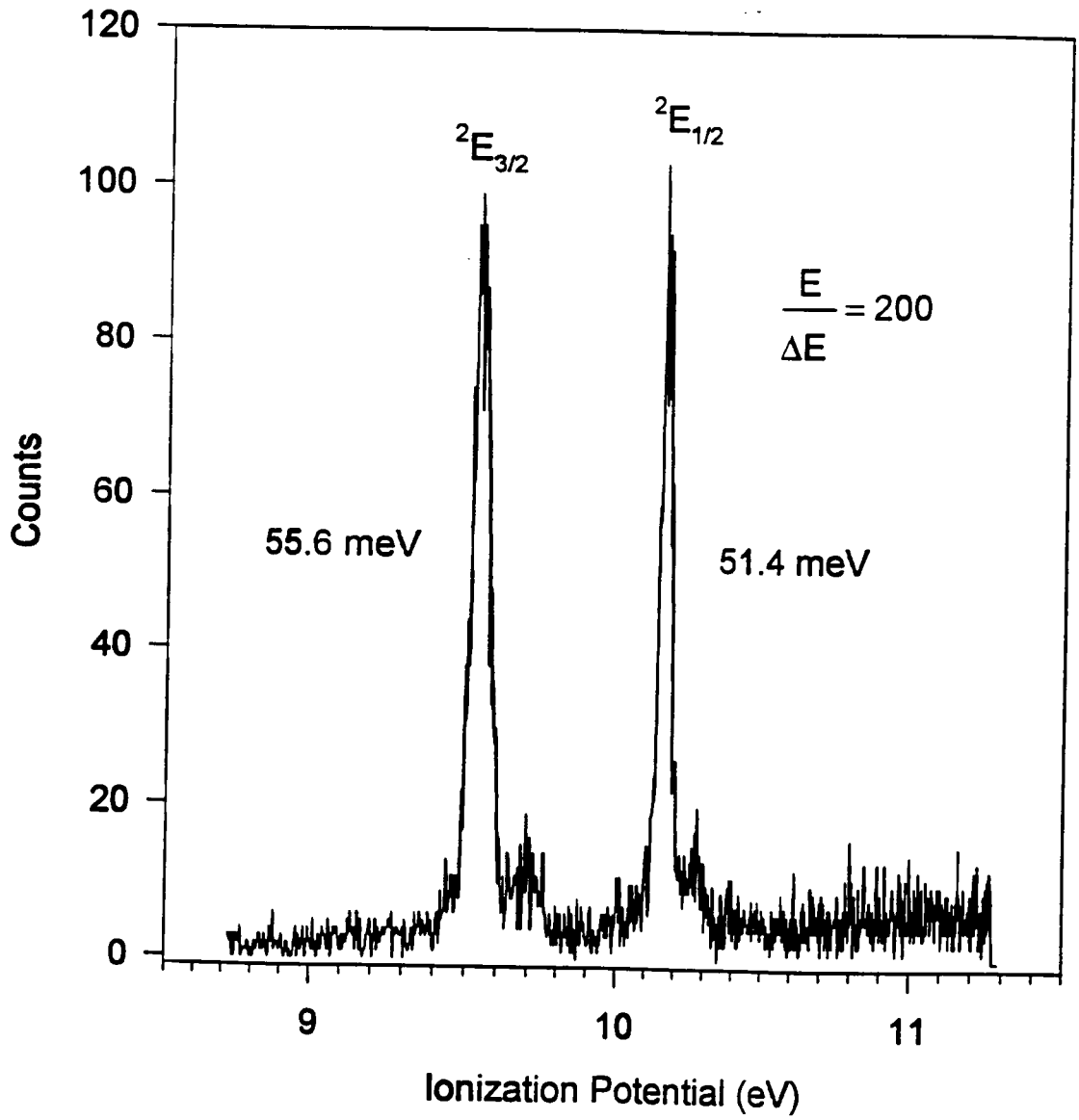

Figure 24. Portion of HeI spectrum of CH_3I showing the resolving power of the analyzer.

CHAPTER 6

TRIETHYLAMINE MPI:PES

Introduction

Triethylamine, $(C_2H_5)_3N$, has been the subject of numerous single and multiphoton ionization photoelectron spectroscopy (MPI:PES) studies. Triethylamine (henceforth denoted as TEA) exhibits two strong, overlapping absorption bands in the ultraviolet[68] centered near 45,000 cm^{-1}. Furthermore, triethylamine (TEA) and other tertiary amines are also found to fluoresce strongly in the UV region. TEA has been used as a medium for ultraviolet radiation detection[69] and suggested as a possible lasing medium.[70] Strong absorption by its excited states, however, preclude its use as a lasing medium.[71] The strong fluorescence of the amines surprised early researchers[72,73,74,75] since all the bonds are saturated. As pointed out by Halpern,[76] the high-lying excited states of saturated molecules normally would be unbound, resulting in short-lived, dissociative states. This is indeed the case for amines for which hydrogen atoms are directly bonded to the nitrogen atom, e.g. ammonia, where predissociation occurs along the N-H bond.[77] The alkylated amines, however, resist predissociation resulting in a weakly allowed transition to the ground state.[78] These longer lived states dominate intermediate-state transitions under multiphoton excitation.

Numerous studies of multiphoton ionization of TEA have appeared. However, competing views emerge as to the mechanisms leading to MPI of TEA. Cureton *et al.*[79]

have shown that rapid internal conversion takes place from an S_2 state to an S_1 state during fluorescence. Building upon this result, Kawasaki *et al.*[80] studied the MPI:PES of TEA. These authors report that photo-ejected electrons originate only from the S_2 level when TEA is illuminated with laser light having less than 3.2 eV energy per photon. A study by Parker *et al.*[81] produced an accurate model of the fragmentation process of TEA in which fragmentation competes with ionization.

The study described in this dissertation was designed to examine the multiphoton ionization processes in TEA through studies of the single (HeI, HeIII PES) and multiphoton ionization photoelectron spectroscopy (MPI:PES) at wavelengths common to both the study of Kawasaki *et al.*[80] and Parker *et al.*[81]

Like ammonia, the ground state of TEA belongs to the C_{3v} point group. The doubly-occupied $3a_1$ nitrogen lone pair orbital forces the alkyl groups out of the D_{3h} planar geometry.[77] A two-photon fluorescence study by Kasatani *et al.*[82] using polarized light confirmed that the excited states of TEA have A_2'' symmetry within the D_{3h} point group. The excited states consist of two singlet Rydberg states arising from a (3s ← n) transition, the S_1 state, and from a (3p ← n) transition, the S_2 state.[77] The S_1 state lies relatively close to the S_2 state as compared to simpler amines; this is typical for amines as the 3s state's term value varies with the degree of alkylation, while the 3p's does not.[77]

Upon excitation, the non-bonding electrons on the nitrogen atom can make a transition either to the S_1 state (3s ← n) transforming as a_2'', or to the S_2 state (3p ← n) and transforming as e"; in either case, the molecule changes from the ground-state

pyramidal geometry to a planar D_{3h} geometry.[77] As Goodman and Philis point out,[83] one can determine the symmetry of the excited states by measuring the ratio, Ω, of fluorescence intensity for circularly polarized light to that of linearly polarized light. If Ω is less than one, the ground and excited states have the same symmetry, and if Ω = 3/2, the states have different symmetry. The Kasatani *et al.* [82] study finds that Ω is less than one for both Rydberg states, showing that the transition occurs between states of the same symmetry. The upper states, however, have a different symmetry than the ground state, and the transition should not be allowed. This suggests that the transition occurs through coupling via the a_2'' "umbrella-inversion" vibrational mode.

Early fluorescence studies[84,79] revealed more about the upper states of TEA suggesting that multiple decay rates exist for TEA. Cureton *et al.*[85] present convincing evidence that rapid internal conversion takes place, and that only two decay rates exist. The dual nature arises only when the two singlet states, S_1 and S_2, are populated simultaneously. Both states can be populated only when the excitation energy exceeds that of S_2. The S_2 state then internally converts quickly to the S_1 state, but the total energy is, of course, greater than for the states formed directly at the S_1 level. Hence, the rates of decay back to the ground state are different. When the excitation energy is below the S_2 threshold, only the S_1 state is populated, and only one rate of decay is observed. For the first case, Cureton *et al.*[85] proposed the following scheme:

$$A + h\nu \rightarrow {}_1A_i^*$$
$${}_1A_i^* \rightarrow {}_1A_r^* \qquad (fast)$$
$${}_1A_r^* \rightarrow A + h\nu_F$$

where A is the ground-state TEA; $_1A_i^*$ represents A in an initially excited state of S_1, and $_1A_r^*$ is the vibrationally reorganized excited state.

And for excitation of the neutral above the S_2 state,

$$A + h\nu \rightarrow {}_2A^*$$
$${}_2A^* \rightarrow {}_1A_n^*$$
$${}_1A_n^* \rightarrow A + h\nu_F$$
$${}_1A_n^* \rightarrow \textit{non-radiative decay}$$

where the set of emitting levels, $_1A_n^*$, is different from $_1A_r^*$. These schemes are shown in Figure 25. From the absorption spectrum of TEA, they determined the S_1 level to be approximately 38,500 cm^{-1} (4.77 eV) above S_0, while S_2 lies about 41,660 cm^{-1} (5.16 eV) above S_0.

Kawasaki *et al.*[80] performed an MPI:PES study of TEA using time-of-flight (TOF) electron spectrometry. They measured the energy of ejected electrons from TEA as they varied the exciting laser wavelengths between 450.9 nm to 381.5 nm. For the range of wavelengths used, they obtained a linear relationship between the kinetic energy of the photoelectron and the laser photon energy. The calculated threshold energy, however, suggested a common level from which ionization proceeded. They proposed the following scheme for the ionization: TEA is first excited to a vibrational level of S_2; at this level, it absorbs an additional photon to arrive at the ionization continuum, leaving the excess vibrational energy in TEA^+.

Using these data, they concluded that the these electrons resulted from photoionization of a state located 41200 cm^{-1} above the ground state (the S_2 state). It

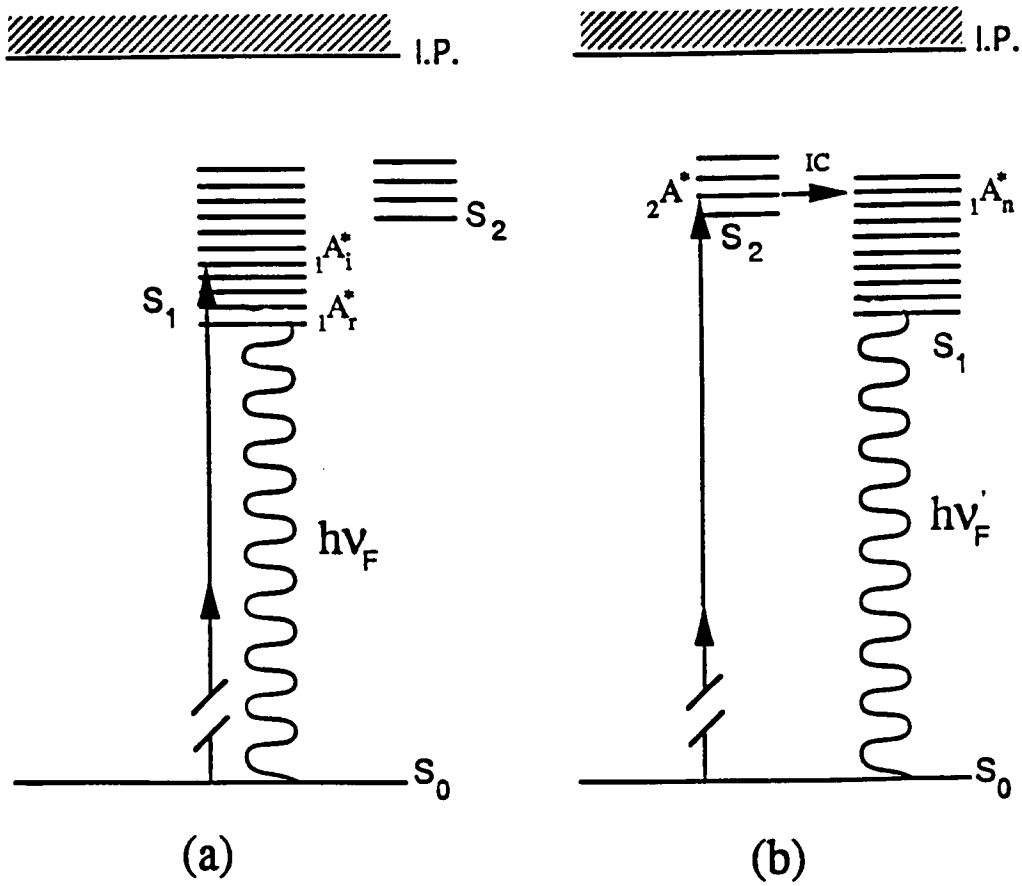

Figure 25. The two fluorescence pathways proposed by Cureton *et al.*[85] to account for the observed dual rates of decay for TEA. In (a), the first photon excites TEA to a point between S_1 and S_2. In (b), the first photon excites TEA above S_2, after which rapid internal conversion to S_1 takes place.

will be shown in this dissertation that this assignment is in error as a result of the use of an incorrect adiabatic ionization potential for TEA and that photoionization, instead, originates from the S_1 state. Previous photoelectron studies have shown that photoelectrons can be emitted from vibrationally excited S_1 and S_2 states of naphthalene,[86] and trimethylamine[87] with internal conversion to the S_1 state competing with ionization from the S_2 state in the latter case.

Parker and co-workers[81] examined the multiphoton ionization and fragmentation of TEA by use of time-of-flight (TOF) mass spectrometry. In their study, multiphoton ionization of TEA was found to fragment the molecule leaving only TEA^+ and TEA^+ minus a CH_3 group in the MPI mass spectrum for wavelengths longer than 390 nm. Surprisingly, the branching ratio for the daughter ion was found to be independent of laser power for wavelengths between 390 nm and 450 nm. The loss of a methyl group is consistent with a conventional photolysis study[88] which reported that the primary photolysis product of TEA is hydrogen atoms with ethyl and methyl radicals combining to form simple alkanes. Parker *et al.*[81] also noted a wavelength dependence on the fragmentation pattern. At wavelengths shorter than 390 nm, a greater fraction of fragments appear, accounting for more than fifty percent of the total mass spectrum.

An accurate value for the adiabatic ionization potential is important for determining whether ionization proceeds from the S_1 or S_2 states in the MPI of TEA. The first step in the present investigation was to determine accurately both the vertical and adiabatic ionization potentials of TEA.

Experimental

Samples of TEA, obtained from J. T. Baker Company (>99 percent pure), were placed in a glass bulb and thoroughly degassed using a freeze-pump-thaw procedure before being introduced into the all-stainless-steel inlet manifold. Checks for impurities were made by an electron-impact-ionization quadrupole mass spectrometer. The inlet valve was operated in a manner such that the flow through it was supersonic.

Photoelectron energy analysis was performed with a custom-built, 180-degree, hemispherical-geometry electron spectrometer as described earlier. Briefly, this spectrometer has a 10 cm effective radius and employs position-sensitive detection. The electron energy resolution at pass energies below 2 eV is better than 15 meV. Ionization is accomplished either by focussed laser light or by the output a HeI-HeII discharge lamp manufactured by VSW, Ltd. Light from either source intersects the molecular beam at right angles. The ions are produced approximately 5 mm in front of a retarding, four-element electrostatic lens, which focusses the photoelectrons into the spectrometer.[89,90]

A relatively short (30 cm) TOF mass spectrometer was used to monitor the ions produced in the MPI study. High mass resolution is not a requirement in this study, however, and this arrangement produced sufficient resolution ($m/\Delta m \approx 100$) to determine accurately ion branching ratios.

For ionization potential measurements, the HeI photoelectron spectra of argon and xenon were used as calibration standards. Once the calibration pass energy was set, the TEA photoelectrons were accelerated to the pass energy by uniformly increasing the

potential of the entire analyzer assembly. All potentials were measured with a calibrated, Fluke model 8840A voltmeter.

For the MPI studies, a Quanta-Ray dye laser system consisting of a dye laser (PDL II) pumped by Nd-YAG laser (DCR II) was used. The laser output was focussed by a 20 cm focal length lens at the entrance to the four-element electrostatic lens of the PES. The laser pulse length was 8 ns with a 10 Hz repetition rate. For wavelengths longer than 355 nm, a Quanta-ray PDL tunable dye laser provided the excitation photons. At and below 355 nm, the third and fourth harmonics of the Nd-YAG laser (355 nm and 266 nm, respectively) were used.

Results and Discussion

Figure 26 shows the HeI photoelectron spectrum of TEA. The feature beginning at 7.5 eV and peaking at 8.3 eV corresponds to ionization proceeding from the lone-pair electrons on the nitrogen atom. The peak associated with this is rather broad which makes the precise determination of the adiabatic ionization potential difficult. In this case, the onset of ionization was determined by noting the point where the signal rose to three standard deviations above the mean baseline value, giving an adiabatic I.P. of 7.47±0.04 eV (all uncertainties reported in this dissertation are at the $\alpha = 0.05$ level of statistical significance). This I.P. value is very close to the photoionization studies of Watanabe[91,92], but exceeds that of Aue *et al.*[93] and is considerably lower than that reported by Al-Joboury and Turner[94] (see Table 6.1). The vertical ionization potential, 8.24±0.03 eV, was located by locating the "center-of-mass" (centroid) of the first major

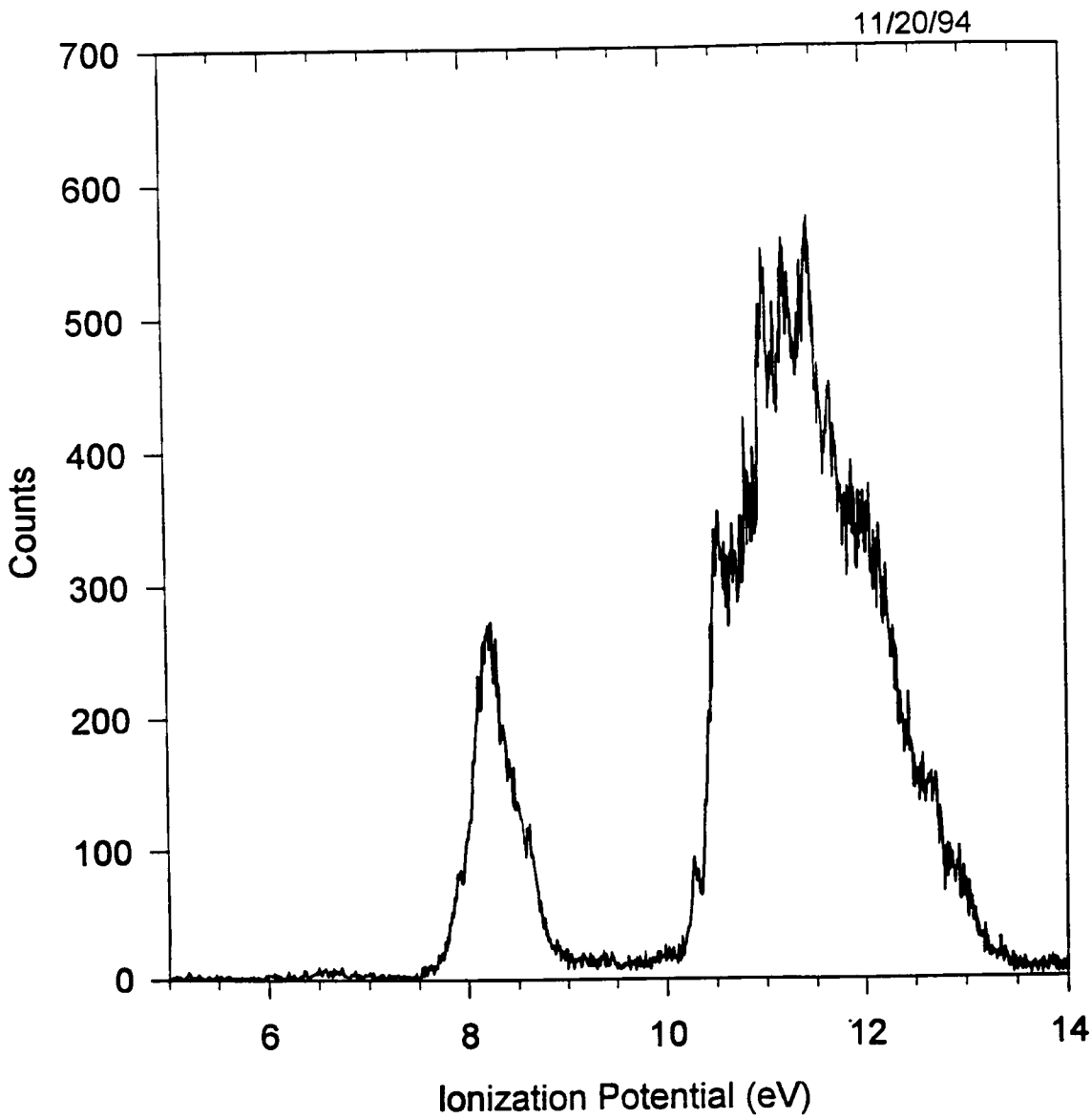

Figure 26. HeI photoelectron spectrum of triethylamine.

Table 6.1. Measured first ionization potentials of TEA using HeI light.

Source	Adiabatic Ionization Potential (eV)	Vertical Ionization Potential (eV)
Watanabe *et al.*[91]	7.50 ± 0.05	
Watanabe *et al.*[92]	7.50 ± 0.02	
Aue *et al.*[93]	7.20	8.05
Al-Joboury and Turner[94]	7.84	
Robin[77]		8.14
This work	7.47 ± 0.04 7.53 ± 0.10[a]	8.24 ± 0.04

[a]non-resonant two-photon ionization

peak. This value is also close but larger than that reported in the above-referenced studies. The precision of the calibration is very high, with a 0.05 percent relative standard deviation being typical for argon and xenon.

Calibration of the electron energy scale for the MPI:PES was accomplished in a novel manner. A major problem in MPI:PES is finding a calibrant with a sufficient number of well-known photoelectron peaks in the region of interest in order to get a statistically accurate energy scale. The single-photon HeI ionization of oxygen produces a series of low-energy (0.2 - 1 eV) photoelectron peaks, leaving the O_2^+ ($B^2\Sigma_g^-$) ion in various states of vibrational excitation. This band encompasses seven peaks in the electron energy range from 0.16 eV to 0.92 eV as shown in Table 6.2 and Figure 27. These seven vibrational peaks of the $B^2\Sigma_g^-$ state have been previously well determined[95] and were used to calibrate the photoelectron energy scale for the laser MPI:PES. Although the photoelectrons typically were accelerated by a modest amount - ~ 3 eV (~4 eV pass energy) - after they entered the analyzer, the potential in the ionization region was fixed at zero for all experiments. This calibration procedure was further checked against the 3 + 2 REMPI electron spectrum via the 6s $[3/2]_0^1$ state of xenon. The photoelectron energies corresponding to leaving $Xe^+ {}^2P_{3/2}$ and $Xe^+ {}^2P_{1/2}$ are 1.931 and 0.625 eV. For this calibration both the $B^2\Sigma_g^-$ and the $b^4\Sigma_g^-$ bands of oxygen were used. Using this procedure, the accuracy in ionization potential was found to be better than one percent (0.02 eV). This calibration procedure eliminated the need to change laser wavelengths for calibration purposes, and provided many more energy calibration points.

Table 6.2. Ionization energies of the O_2^+ $B^2\Sigma_g^-$ state.[95]

v′	Energy (eV)	Electron K.E (eV) (HeI light)
0	20.296	0.922
1	20.434	0.784
2	20.566	0.652
3	20.693	0.525
4	20.815	0.403
5	20.930	0.288

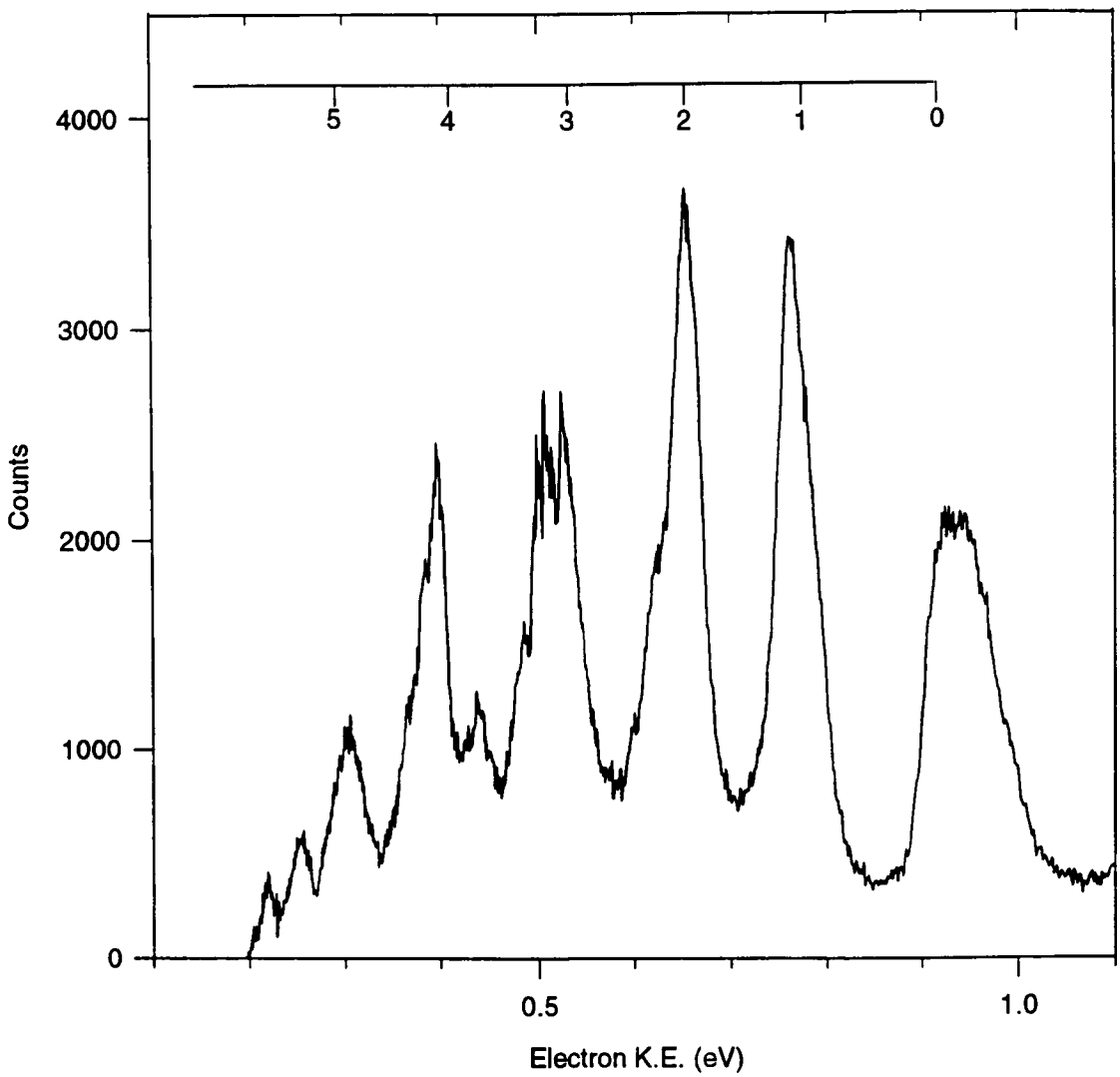

Figure 27. HeI spectrum of the oxygen $B^2\Sigma_g^-$ band. Relative peak heights are not correct because the electrostatic lens was adjusted to emphasize lower-energy electrons.

Photoelectron spectra were taken with photon energies ranging from 18800 cm^{-1} (2.33 eV) to 37559 cm^{-1} (4.66 eV) (see Figure 28). The photoelectron spectrum data corresponding to two-photon-internal conversion - resonant one photoionization (which will be designated 2 IC 1) shows close agreement with that of Kawasaki *et al.*[80] over most of the common range of wavelengths studied (see Figure 29). The electron energies show a linear relationship with the electron originating from a level positioned 21900 ± 790 cm^{-1} (2.72 ± 0.10 eV) below the ionization threshold. This term value is statistically the same (22,200 ± 400 cm^{-1}) as obtained by regressing the reported data from the Kawasaki group, although an apparent typographical error in their paper put this value at 23,200 cm^{-1}. When used with the adiabatic I.P. of 7.47 eV, this result shows that ionization proceeds from a level which is 4.75 ± 0.17 eV above S_0. This energy level corresponds very closely (4.77 eV) with the S_1 state as determined by Cureton *et al.*[85] The slope of the linear regression of photon energy versus electron energy (in eV) for the data from 23000 cm^{-1} to 24600 cm^{-1} is also statistically the same as that of Kawasaki et al,[80] viz., 1.06.

The data from the two studies, however, diverge at the highest photon energy. The kinetic energy of the ejected electrons drops off rapidly with wavelength as shown in Figure 30. This drop off coincides rather closely with the almost complete fragmentation of the TEA parent molecule as determined by Parker *et al.*[81] and here.

The fragmentation pattern of TEA obtained in this study closely matches that reported by Parker *et al.*[81] The fragments observed at wavelengths of 355.0 nm and

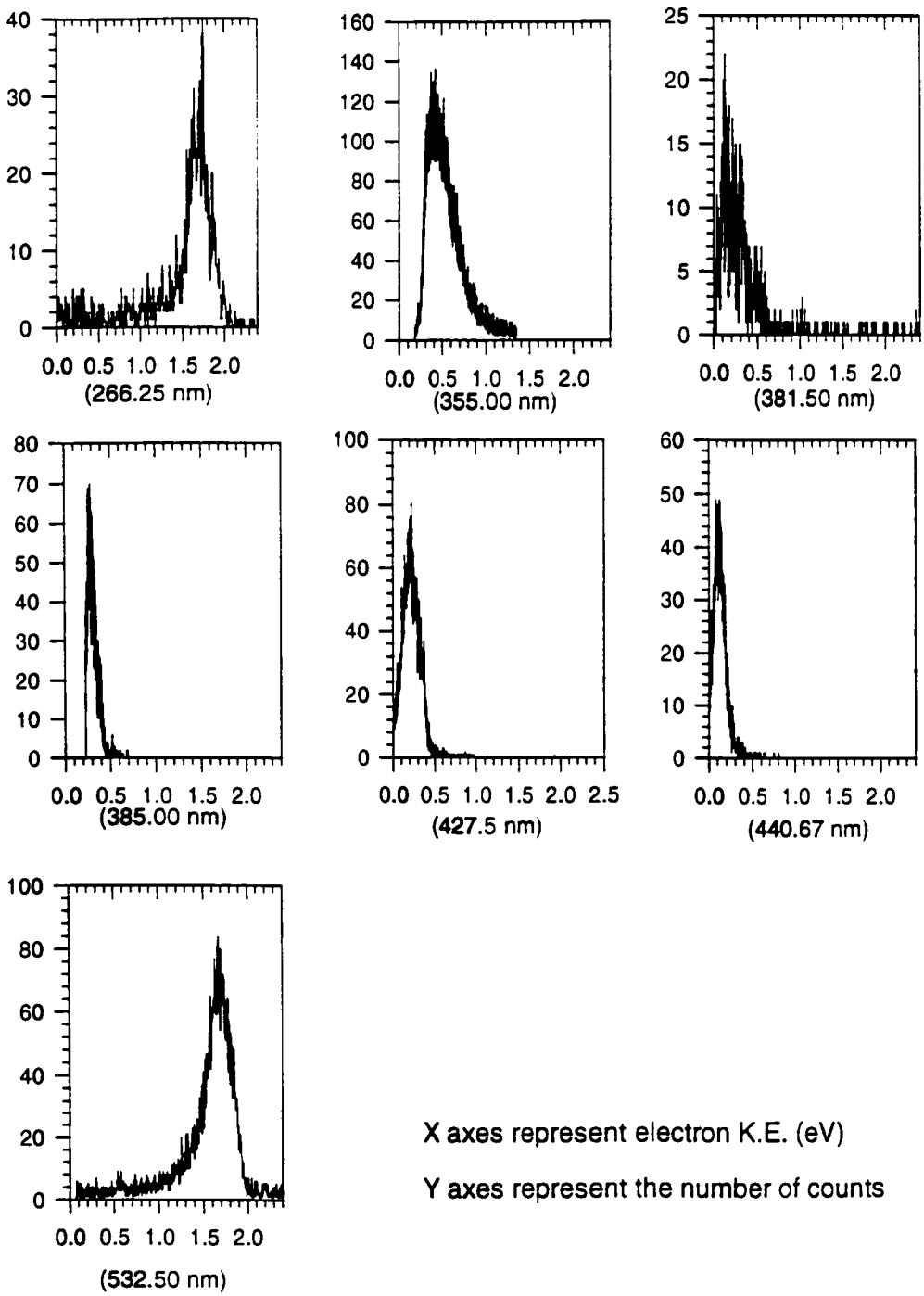

Figure 28. MPI photoelectron spectra of TEA taken at the wavelengths indicated.

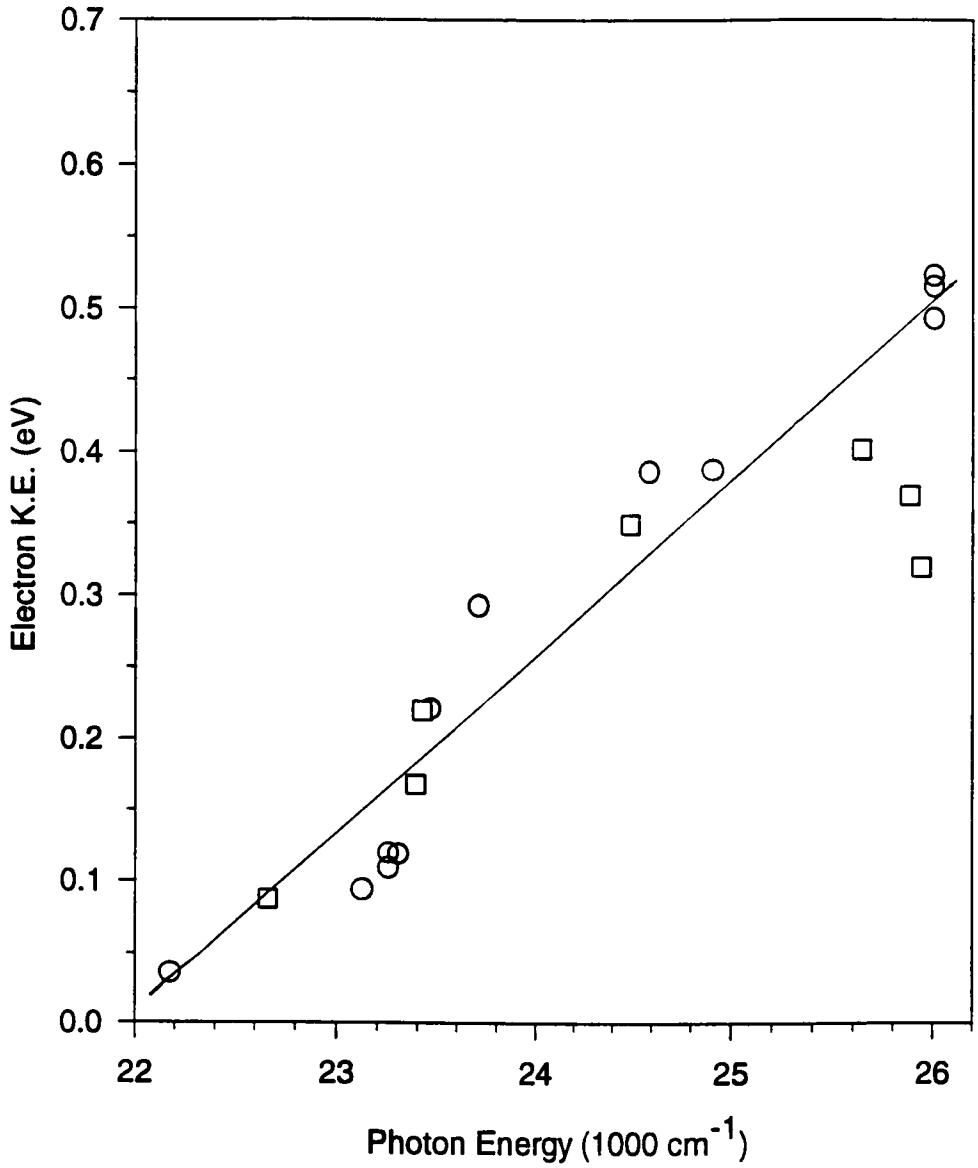

Figure 29. TEA photoelectron energies generated by photons with energy from 22700 cm^{-1} to 26200 cm^{-1}. Squares indicate present work; circles are data from Kawasaki *et al.*[80]

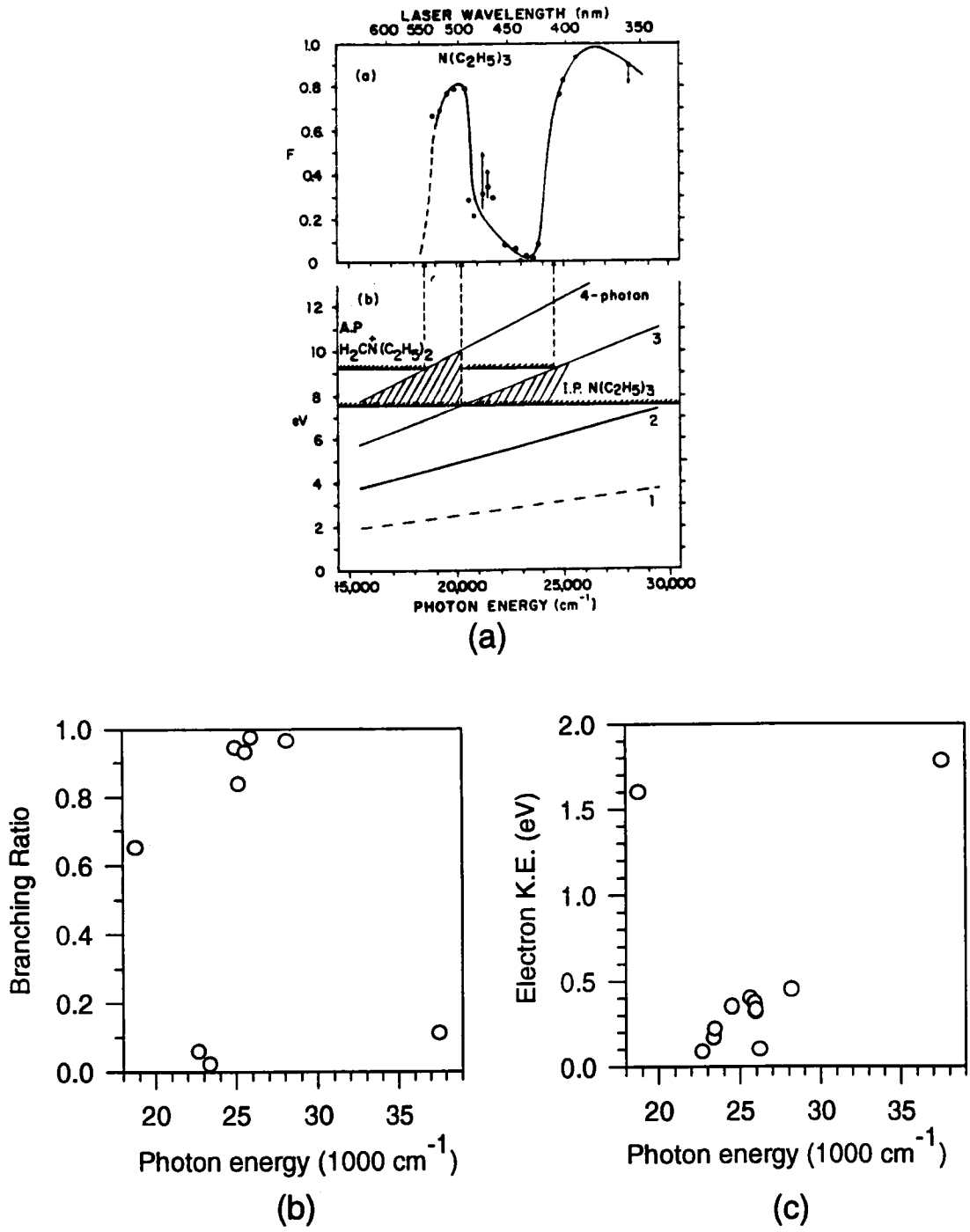

Figure 30. Comparison of (a) the framentation pattern obtained by Parker *et al.* (diagram taken from their figure7), (b) the fragmentation pattern (branching ratio), and (c) the kinetic energies of the photoelectrons as a function of photon energy. The photoelectron energies are taken as the statistical mode of the photoelectron energy distribution.

532.5 nm consist of the parent ion together with the parent with successive numbers of methyl groups removed. However, the fragmentation patterns seen at the other wavelengths are different. In most cases, the parent peak predominates, with only one daughter peak (mass 86) observed.

The degree of fragmentation, indicated by F, the branching ratio, is defined as F = D/(D+P), where D is the total signal arising from the daughter ion fragments, and P is the parent ion signal. The fragmentation of TEA for a wavelength of 355 nm is shown in Figure 31. As the photon energy is increased from 18800 cm^{-1}, F increases from approximately 0.65 to a maximum of 0.98 in the neighborhood of 20500 cm^{-1}.(Parker *et al.*) At this point, F falls rapidly to a value of 0.02 at 23400 cm^{-1} where it remains until the photon energy approaches 24600 cm^{-1}. When the photon energy reaches this level, F increases extremely rapidly to 0.98, i.e., almost total fragmentation occurs. This high degree of fragmentation hardly decreases at 28000 cm^{-1} where it is 0.96. In contrast to the Parker group's results, however, a laser power dependence was noted for fragmentation at many wavelengths between 450 nm and 420 nm as Figure 32 shows, indicating that additional photons are being absorbed by the ion.

At the highest MPI photon energy studied, 4.657 eV, non-resonant MPI is seen to occur with little fragmentation. The energy of the first photon is slightly (0.09 eV) below S_1. The second photon then excites the molecule to an energy level slightly beyond the calculated[79] appearance potential of the daughter ion. The fact that the degree of fragmentation is small suggests that the appearance potential is higher than

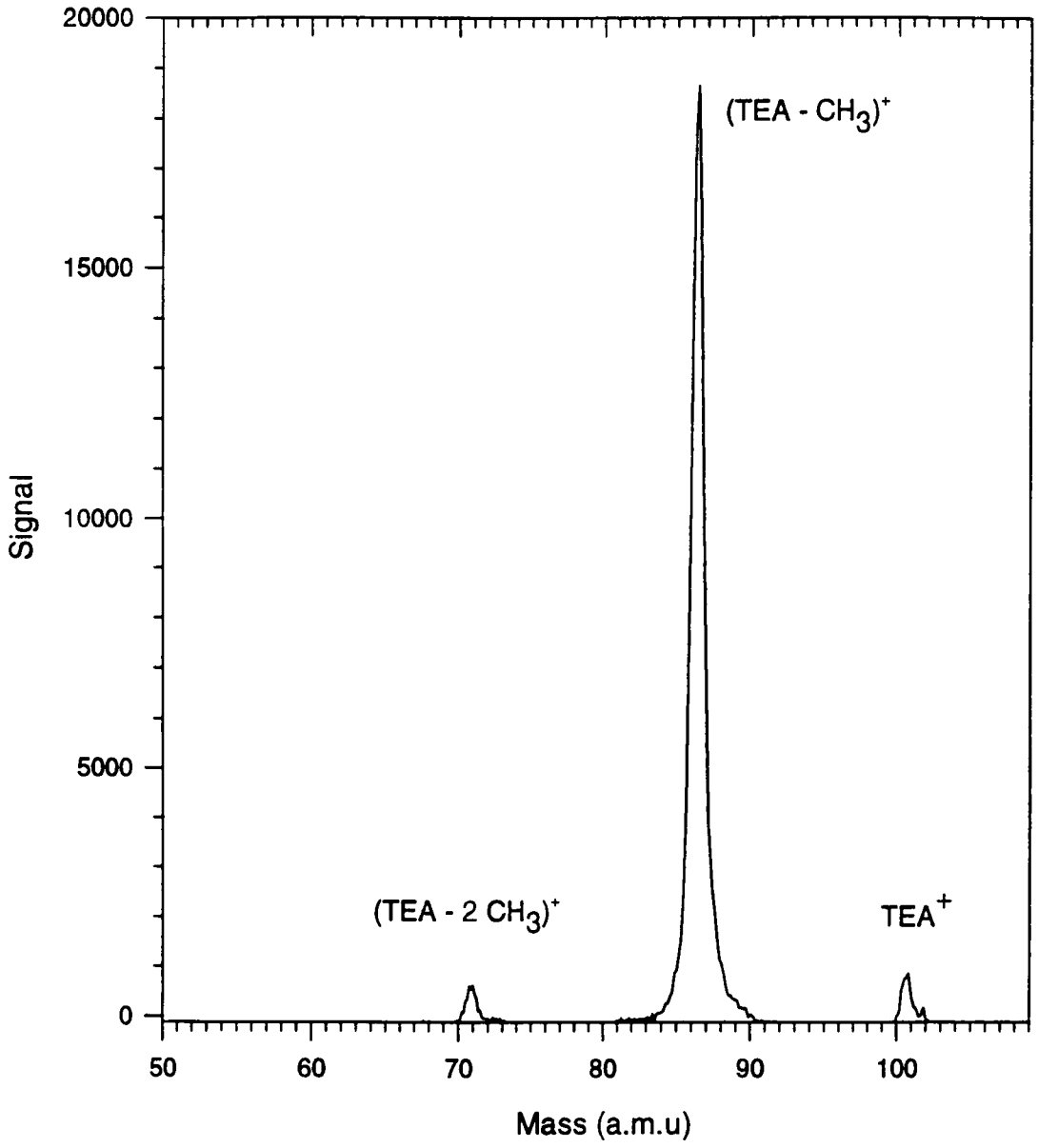

Figure 31. TOF mass spectrum of TEA at a laser wavelength of 355.0 nm.

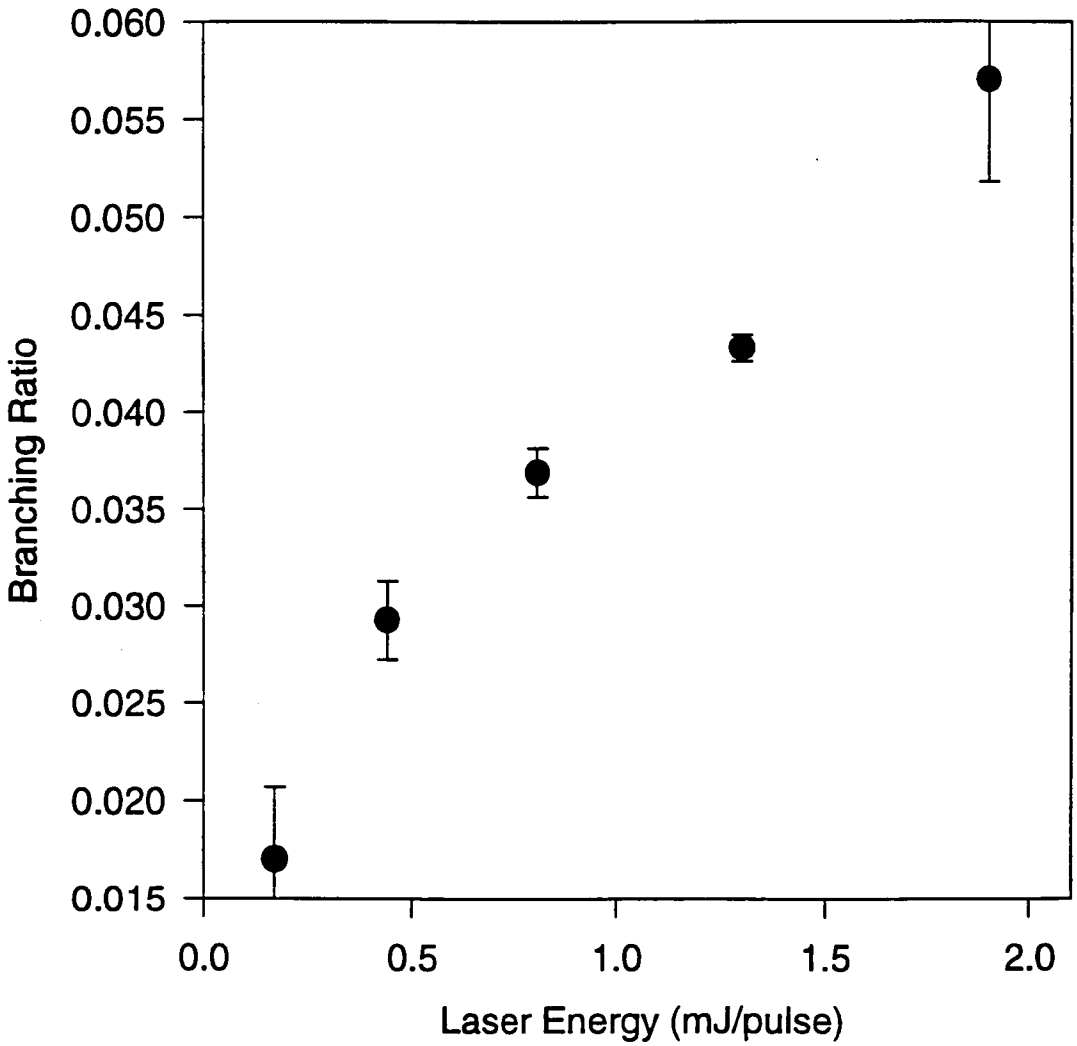

Figure 32. Branching ratio dependence on laser power at a wavelength of 440.8 nm.

twice the photon energy, i.e., 9.3 eV. The measured photoelectron energy, 1.78 eV, provides an additional and more direct means for determining the adiabatic I.P. of TEA. From the two-photon PES, the adiabatic ionization potential is found to be 7.53 ± 0.10 eV (9.313 eV - 1.78 eV). The fact that this photoelectron peak is relatively narrow and steeply rising at this energy is surprising since it is expected that the Franck-Condon overlap between the pyramidal-geometry ground state and the planar-geometry ion would be very small. This difference in geometries between the ground state and the ion is similar to the case of ionization of the non-bonding nitrogen electrons by HeI light where the resulting photoelectron peak at the vertical ionization potential of 8.24 eV is very broad. But just as in the case of two-photon fluorescence experiments mentioned earlier,[79, 82, 85] the argument can be invoked that vibrational coupling through the umbrella-inversion mode may enable this transition. Another way around this problem is to consider the uncertainty associated with the energy of the S_1 state. It can be argued that the S_1 state is at, or slightly below, 4.66 eV, since the 95 percent confidence interval for S_1 in this study is 4.58 eV to 4.92 eV. Finally, the possibility exists that the ground state has populated excited vibrational levels, supplying the necessary 0.09 eV to reach S_1. A likely vibrational mode would be the symmetric CN stretching mode[96] at 736 cm^{-1} (0.0912 eV). At 25 °C, however, only 3 percent of the TEA ground state population would occupy this level.

At the lowest extreme in photon energy for this study, 2.33 eV (532.5 nm), the degree of fragmentation is much greater, and the width of the photoelectron spectrum peak is somewhat broader reflecting this partitioning between fragmentation and

ionization. The resemblance of this photoelectron peak to that resulting from MPI with 4.66 eV photons is noteworthy.

To account for the variation in the fragmentation pattern as a function of the laser wavelength, Parker *et al.*[81] proposed that TEA is non-resonantly ionized, and that fragmentation occurs when the appearance potential of the first daughter ion, 9.2 eV, is exceeded. In their view, the degree of fragmentation decreases in the transition region where the number of photons required for ionization decreases: more photons are required for fragmentation than for ionization. For example, according to this hypothesis, one should see a sharp fall-off in fragmentation in the region of 495 nm (photon energy = 2.5 eV), where the number of photons required for ionization drops from four to three, but the number of photons required for fragmentation remains at four. Furthermore, as the laser wavelength is decreased, fragmentation should greatly increase in the region around 400 nm (photon energy = 3.1 eV) where, for the first time, the energy of the three photons causing ionization also exceeds 9.2 eV. This is exactly what happens.

As stated earlier, the photoelectron energies in the region from 450 nm to 385 nm show that the ionization process in TEA at these wavelengths can be best described in terms of a two-photon absorption into S_2, followed by internal conversion to the S_1 state from which ionization occurs (2 IC 1). This process is different from the typical REMPI process in that an internal conversion step takes place just before the ionization step as shown in Figure 33. The (2 IC 1) process is proposed because no evidence for non-REMPI photoelectrons was observed for these wavelengths. Moreover, at points

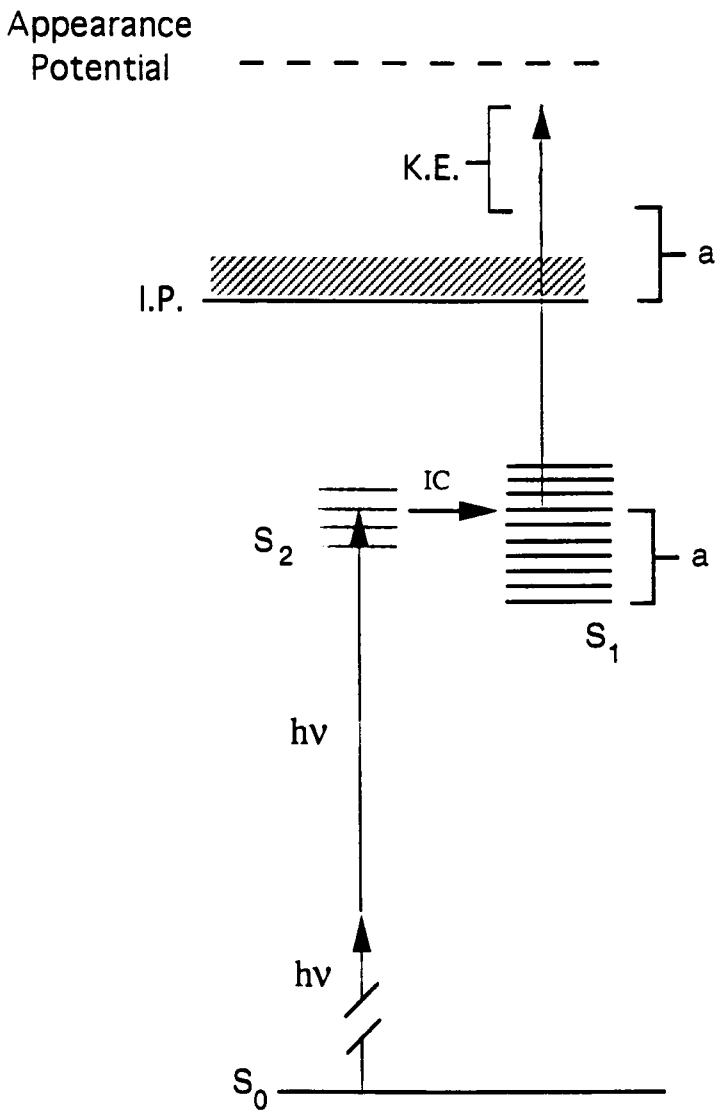

Figure 33. Diagram of 2 IC 1 process in TEA.

where the fragmentation is not extensive, and, consequently, the photoelectron peaks are narrow, the photoelectron energies are seen to be much too low for a non-resonant MPI process.

For photon energies in which the last photon is above 25000 cm^{-1} (i.e., in the region where fragmentation increases greatly), the photoelectron energies first fall almost to 0 eV and then rise. At 355.0 nm (28160 cm^{-1}), extensive fragmentation is still occurring, but the centroid of the photoelectron energy distribution, 0.45 eV, now has a value lower than that expected for (2 IC 1) through S_1. The photoelectron peak is quite broad, however, with photoelectron energies extending to 0.85 eV. The highest photoelectron energy corresponds to the maximum energy expected for (2 IC 1) through S_1. Much the same situation is observed at 385.0 nm. Here the centroid of the photoelectron energy distribution is 0.35 eV with photoelectron energies extending to 0.47 eV. The latter energy, again, matches the highest energy expected with REMPI through S_1. At the other photon energy region where extensive fragmentation takes place, 18800 cm^{-1}, the photoelectrons, again, have a very broad energy distribution with the highest observed photoelectron energy corresponding to ionization out of S_1.

To account for the broad range of the photoelectron energies observed at single photon wavelengths, one could conclude that photoionization of the S_1 state leaves the TEA^+ ion with some internal energy as shown in figure 25. Unlike a photoelectron of study of trimethylamine[87], no evidence for photoelectrons from the S_2 state was found.

Conclusions

In order to elucidate the nature of MPI of TEA, this study has used both single-

photon, HeI PES and multiphoton PES. A custom-built, hemispherical, electron energy analyzer incorporating position-sensitive detection was employed to determine from which of TEA's two singlet states, S_1 or S_2, the ionization step proceeds. The one-photon vertical and adiabatic ionization potentials of TEA are 8.24 ± 0.04 eV and 7.47 ± 0.04 eV, respectively. The determination of the adiabatic I.P. is crucial is assigning the origin of MPI photoelectrons, and measurements of the MPI photoelectron energies as a function of photon energies prove that the photoelectrons are ejected from S_1 and not S_2. Thus, the MPI of TEA can be described as a process in which internal conversion to S_1 is an intermediate step. This remarkable result holds even if the molecule is initially excited to energies above S_2 but below the ionization threshold.

Fragmentation and electron energy data suggest the existence of a dissociative state 7.8 eV above S_0. The primary evidence of this state is that the degree of fragmentation, in terms of the ratio of fragment signal to total signal, is nearly 100 percent in the neighborhood of this state. Although the energies of the fastest electrons near this state still reflect their S_1 origin, the widths of the asymmetric photoelectron peaks are very wide compared to photoelectron spectra taken at photon energies further away, showing that considerable internal energy has been added to the ion.

The use of previously determined, well-defined HeI photoelectron spectra provides improved energy calibration of electron spectrometers used in MPI:PES when compared to the sparse number of peaks normally associated with MPI energy calibration.

CHAPTER 7

BROMOCHLOROFLUOROMETHANE

Introduction

A one-photon photoelectron study of bromochlorofluoromethane (BCFM) was conducted as a prelude to more extensive polarization studies of chiral molecules. BCFM is one of the simplest chiral molecules, and several theoretical studies[97,98,99] have been conducted on it. But because of the difficulty in preparing samples of it with a net optical activity, only a few experimental studies of the optically-active form had been performed until recently. Improved methods for its synthesis and separation into optically active forms were reported[100,101] in 1985.

The first spectroscopic study of BCFM was reported by Glockler and Leader[102] who, in 1940, reported on the liquid Raman spectrum. Infrared spectroscopic data was not reported until 1951 when Plyler and Lamb[103], conducting both gas- and liquid phase studies, gave fundamental assignments. Not long after this, Pitzer and Gelles[104] used a product rule to confirm these assignments. Because this molecule lacks symmetry, no normal coordinate treatment was ever carried out until El-Sabban and Zwolinski[97] used a force-field treatment with 55 force constants to perform the calculation. Using infrared and Raman data on isotopic variants of bromochlorfluoromethane, Diem and Burow[98] refined the previous force-field calculation to develop a valence force field. An electron diffraction study by Jacob[105] reported the main carbon-halogen structural parameters.

The optically active forms of BCFM have been isolated only within the last quarter-century. In 1969, Hargreaves and Modarai[106] isolated the (+) and (-) forms of BCFM with $[\alpha]_D$ +0.20° and -0.13°. Shortly thereafter, Wilen *et al.*[107] reported having isolated fractions with $[\alpha]_D$ up to 0.128°. An improved method for isolating the enantiomers by inclusion within the cavity of a chiral host molecule allowed the enantiomeric excess, ee, to be measured for the first time by ^1H NMR spectroscopy.[100] With this information, Wilen *et al.*[101] determined that an enantiomerically pure sample would have $[\alpha]_D^{25}$ +1.6°. Moreover, Wilen *et al.*[101] found that the optical activity remained unchanged for over a period of ten years.

A photoelectron spectroscopy (PES) study of BCFM by Novak *et al.*[108] determined the vertical ionization potential to be 11.16±0.03 eV. They observed vibrational fine structure in only the $\tilde{B}$ electronic system, the electronic system which is attributable to the non-bonding chlorine lone-pair ionization. They explained the large splitting in the chlorine $3p^{-1}$ bands, $\tilde{B}$ and $\tilde{C}$, as the "CHF effect" in which the presence of a single fluorine atom causes a significant splitting to occur while two fluorine atoms quenches the effect by cancellation.

Any splitting in BCFM is unexpected given that the molecule belongs to the C_s symmetry group. A paper by Brogli and Heilbronner[109] showed that the splitting is result of two opposing effects. First, any splitting that may arise from the cylindrical symmetry of the halogen field is reduced by the conjugation of the halogen $p_{x,y}$ oribitals with the bonds of the other groups attached to the central carbon atom. Second, the fact that the degree of conjugative interaction is different for the different halogen p oribitals

creates an opposing effect so as to increase the splitting. They also pointed out that the shapes of the two spin-orbit peaks should be different, with one showing more vibrational structure (because of its stronger interaction with the bonding orbitals) than the other.

Experimental

The apparatus used has been described earlier in Chapter 4. In brief, a UV lamp producing 21.22 eV photons illuminated a supersonic gas beam at right angles. The kinetic energies photoelectrons produced by this interaction were analyzed by a large-radius hemispherical electron spectrometer.

The bromochlorofluoromethane was synthesized by R. Pagni of The University of Tennessee. Approximately 5 ml of the original sample remained after transporting it to the electron spectroscopy laboratory. The sample was placed in a glass bulb and subjected to four freeze-pump-thaw cycles before it was admitted to the all-stainless-steel inlet manifold.

Calibration of the spectrometer was done with the $Xe^+ {}^2P_{3/2}$, $^2P_{1/2}$, and the CH_3I^+ $^2E_{3/2}$, $^2E_{1/2}$ HeI calibration lines. FWHM resolution at a pass energy of 11 eV is better than 52 meV as measured by the $^2E_{1/2}$ line of CH_3I.

Results and Discussion

The vibrational structure of the bromine and chlorine peaks, which had been heretofore unresolved, was determined. Because the BCFM was subjected to a supersonic expansion, its temperature was greatly reduced by the time it reached the

entrance to the electrostatic analyzer. The degree of cooling can be estimated with the aid of equations (4.42) and (4.43). The ratio c_p/c_v was estimated by taking an average of this ratio[110] for five chlorofluorocarbons ranging from Freon 11™ to Freon 22™. The average was estimated to be 1.13±0.04. From this, it is estimated that the Mach number is 10, and that the temperature over the entrance is approximately 40K.

The full spectrum of BCFM was obtained by applying an accelerating potential of 35 volts to the entire spectrometer. This enabled the position-sensitive detector to measure electron energies from 0 to 9 eV (ionization potentials from 12 to 21 eV), which encompassed the expected ionization potential of bromine's lone pair. The resulting photoelectron spectrum matched that of Novak *et al.*[108] (see Figure 34 and table 7.1). Assignments are based upon those of Novak et al.[108]

Next, the pass energy was reduced to 15 eV to measure more closely the adiabatic and vertical ionization potentials. As can be seen in Figure 35, the spin-orbit splitting of the bromine peaks is clearly seen, and the vibrational structure of the $\tilde{B}$ band is just resolved. The adiabatic ionization potential was determined by finding the point where the signal rose three standard deviations above the mean baseline level, and the vertical ionization potential was taken as the highest point on the peak. Using these criteria, the adiabatic ionization potential of BCFM is 11.05±0.05 eV, and vertical ionization potential is 11.28±0.05 eV.

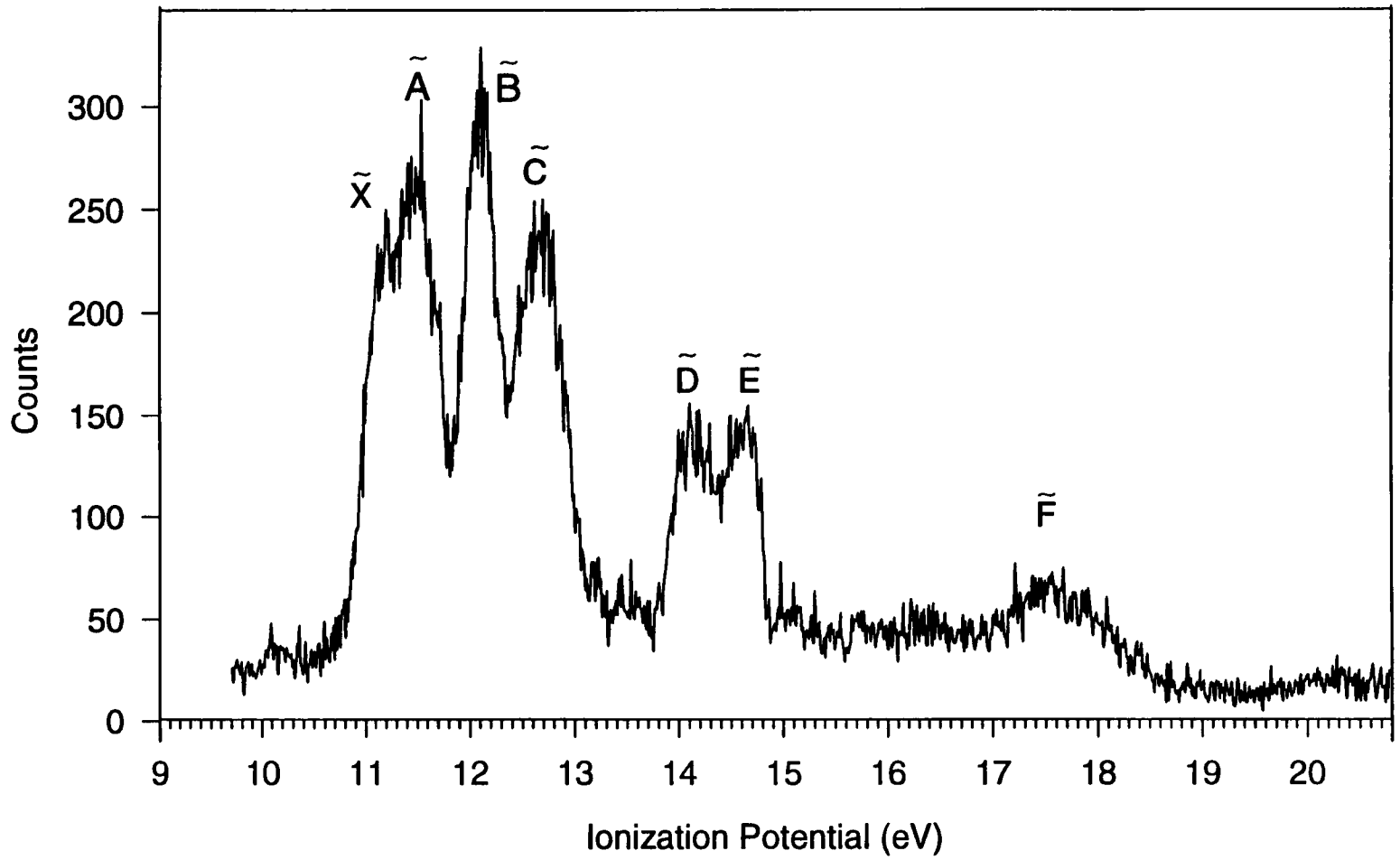

Figure 34. HeI photoelectron spectrum of bromochlorofluoromethane.

Table 7.1. Vertical ionization potentials and assignments of BCFM

State	This work	Novak *et al.*	Assignment
$\tilde{X}$	11.28	11.16	n_{Br}
$\tilde{A}$	11.60	11.49	n_{Br}
$\tilde{B}$	12.03	12.05	n_{Cl}
$\tilde{C}$	12.62	12.60	n_{Cl}
$\tilde{D}$	14.23	14.02	CH/CBr
$\tilde{E}$	14.63	14.47	CF/CCl
$\tilde{F}$	17.40	17.56	n_F/CF

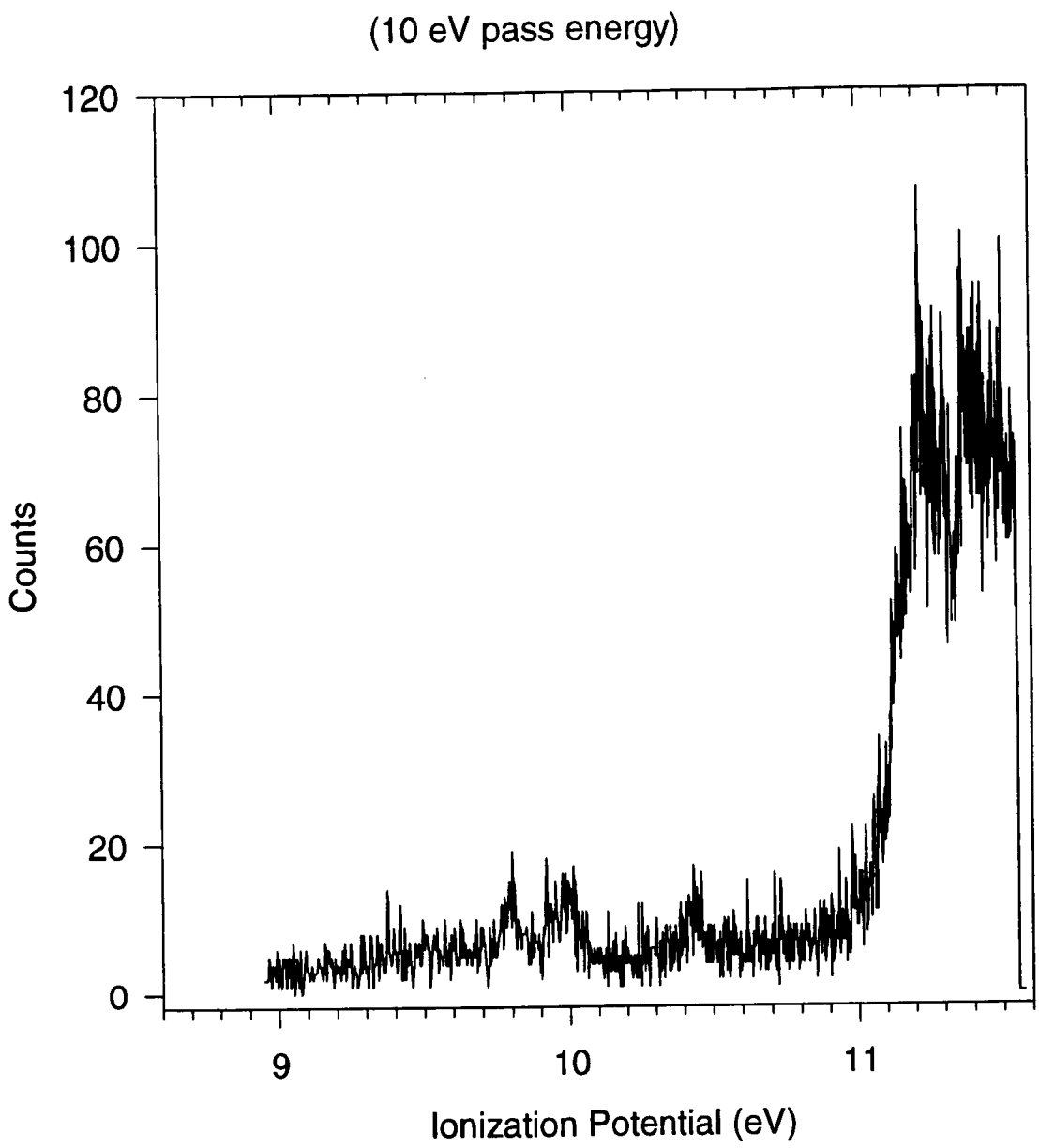

Figure 35. Portion of photoelectron spectrum used for ionization potential determination. Vibrational structure is just resolvable.

To determine both the spin-orbit splitting and the vibrational structure of the bromine peaks, the pass energy was further reduced to 5.00 eV. The $^2A'$ band of NH_3^+ was used for calibration. At this energy, it appears that some vibrational structure is present on the Br peaks as shown in Figure 36, but the vibrational spacing could not be reliably measured. The spin-orbit splitting of the Br atom in this study (0.32 eV) is statistically the same as that measured by Novak *et al.* (0.33 eV), and consistent with the spin-orbit coupling factor, δ, for bromine (0.305).[1] The observed splitting of the chlorine peaks, 0.59eV, is much larger than the δ for chlorine (0.073), and can be attributed to through-space interactions between the chlorine 3p lone-pair electrons with the other orbital species of BCFM.

The two chlorine peaks differ greatly in appearance as shown in Figure 37. This area of the photoelectron spectrum was taken at a higher resolution with the analyzer pass energy set to 8.00 eV. The $\tilde{B}$ band is rather sharp, indicating that a small change in BCFM's geometry occurred as this 3p electron was removed. The pass energy was further reduced to 6.00 eV to determine the vibrational spacing. As seen in Figure 38, three vibrational peaks can be discerned. The vibrational spacing of the first two peaks of 730±50 cm^{-1} fits the C-Cl stretching mode (ν_5 = 772 cm^{-1}).[98] The other chlorine peak was examined at an even lower pass energy, 3.00 eV, to determine its vibrational spacing. This peak, denoted as $\tilde{C}$, is broad, and has a smaller vibrational spacing of 570±30 cm^{-1}. The broadness of this band is in concert with the higher stabilization (higher I.P.) of this orbital caused by the interaction of it with the bonding orbital. In other words, the chlorine 3p orbital responsible for the $\tilde{B}$ band has very little overlap

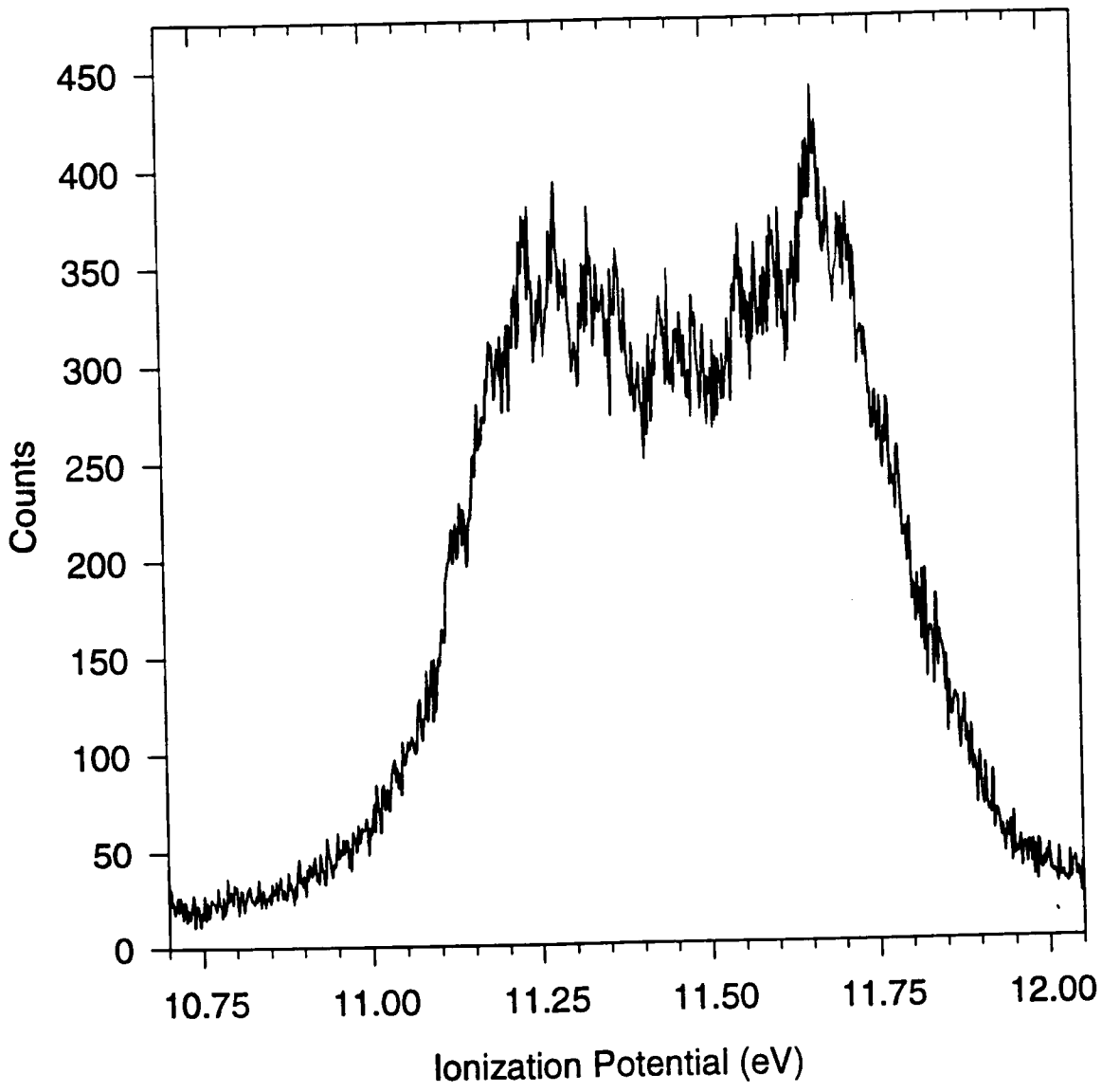

Figure 36. Bromine peaks seen at a pass energy of 5.00 eV.

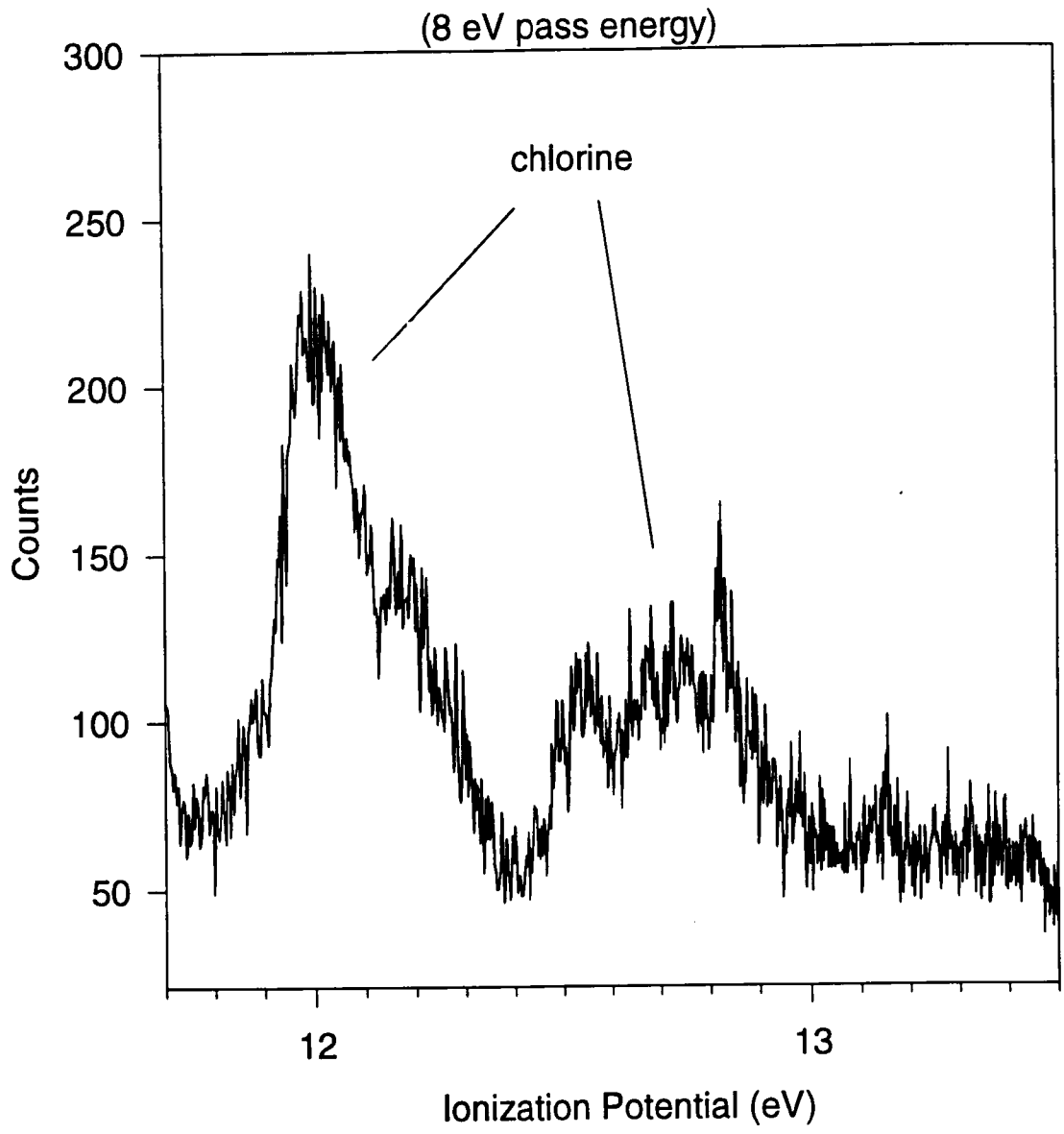

Figure 37. Portion of photoelectron spectrum showing the chlorine peaks.

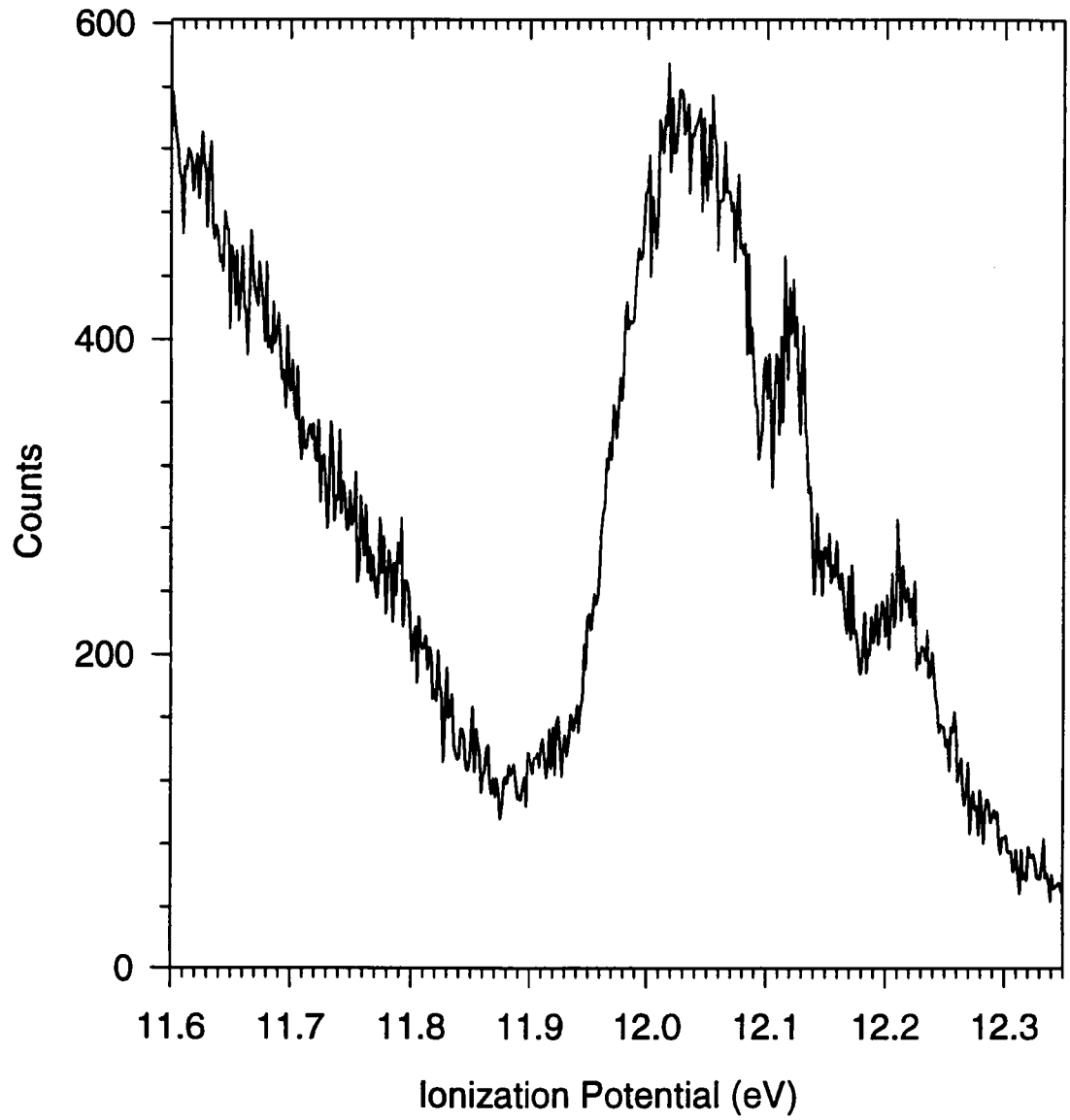

Figure 38. Portion of the HeI photoelectron spectrum of BCFM showing the part of the second Br peak and all of the first Cl peak. The vibrational structure on the Cl peak is clearly seen.

with a sigma bonding orbital, while the other 3p electron, because of its more favorable orientation, has a greater overlap with a sigma bonding orbital and is thus stabilized.

Either the C-H stretching mode (ν_1 = 1202 cm^{-1}), or the bending mode (ν_2 = 1299 cm^{-1}) might be responsible for the observed vibrational spacings on $\tilde{D}$. The spacing (1300 cm^{-1}) was easily observed as shown in Figure 39, even though the pass energy was set to 24 eV in order to encompass the Ar and Xe peaks used for calibration.

The band corresponding to ionization of the non-bonding F atom has a very broad profile, indicating a large change in geometry takes place upon going from the neutral to the ion. This large change in geometry makes assignment of its vibrational spacing of 1100 cm^{-1} to a given mode in the neutral difficult, although the nearest mode which has some F influence is the C - F stretch at 1060 cm^{-1}.

Conclusion

The electron spectrometer used in this study has shown that it has the capability of performing high-resolution spectroscopy on molecules with a multitude of features. The photoelectron vibrational fine structure of the bromine and chlorine peaks of BCFM has, for the first time, been resolved. Future work with this analyzer using polarized UV and laser light will further elucidate the structure of BCFM, one of the simplest chiral molecules.

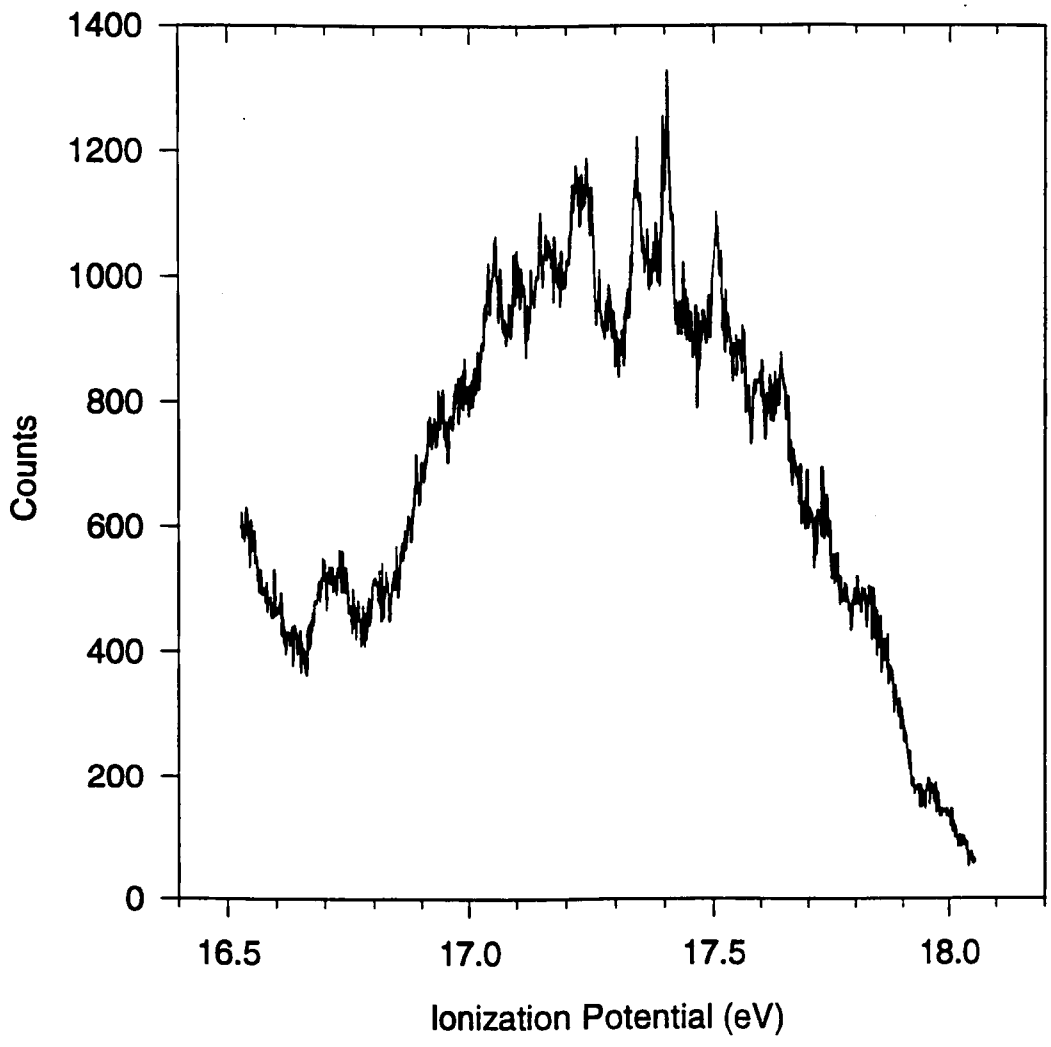

Figure 39. Portion of HeI spectrum of BCFM showing the peaks due to F and CH.

CHAPTER 8

CONCLUSIONS

The hemispherical electron spectrometer described in this dissertation has been shown to be capable of meeting its theoretical maximum resolving power of 200. Although the aluminum hemispherical surfaces are not coated with colloidal graphite, this does not seem to affect the overall performance of the spectrometer at pass energies greater than 5 eV. These surfaces, however, will be coated in the event that slower electrons are being affected. For the position decoding method described in this dissertation, it is very important to recognize that the response of the system across the detector's length is not truly linear. Fortunately, the response can be accurately modeled such that non-linearities can be eliminated. The versatility of having both the single-photon UV lamp and the multiphoton-capable laser was demonstrated in the two studies conducted for this work.

By using the single-photon source, it was possible to measure accurately the adiabatic ionization potential of triethylamine. This information was used to determine the origin of the ionization step in the multiphoton ionization of the molecule. During three photon ionization, it was shown that triethylamine undergoes internal conversion from the S_2 state to the S_1 state. This process was designated as 2 IC 1.

A single-photon ionization study of bromochlorofluoromethane demonstrated the high resolving power of the spectrometer: vibrational structure on the chlorine and

fluorine-CH peaks of the ionic species was observed for the first time. The vibrational frequencies measured on these ionic peaks is consistent with those found in the neutral species.

LIST OF REFERENCES

1. J. H. D. Eland, Photoelectron Spectroscopy, (London, Butterworths: 1982).

2. J. Wayne Rabelais, Principles of Ultraviolet Photoelectron Spectroscopy, (New York: John Wiley and Sons, 1977).

3. D. L. Andrews, "Fundamental Principles of Laser Spectroscopy," in Applied Laser Spectroscopy: Techniques, Instrumentation, and Applications, edited by D. L. Andrews, (New York: VCH Publishers, 1992).

4. R. C. Williamson, "The Ionization of Potassium Vapor by Light," Physical Review 21 (1923) 127.

5. P. D. Foote and F. L. Mohler, "Photo-electric ionization of caesium vapor," Physical Review 26 (1925) 195.

6. K. Siegbahn and K. Edvarson, "β-ray spectroscopy in the precision range of $1:10^5$," Nuclear Physics 1 (1956) 137.

7. C. Nordling, E. Sokolowski, and K. Siegbahn, "Precision Method for Obtaining Absolute Values of Atomic Binding Energies," Physical Review 105 (1957) 1676.

8. F. I. Vilesov, B. L. Kurbatov, and A. N. Terenin, "Energy Distribution of Electrons in Photoionization of Aromatic Amines in the Gaseous Phase," Soviet Physics-Doklady 8 (1961) 490.

9. D. W. Turner and M. Al Joboury, "Determination of Ionization Potentials by Photoelectron Energy Measurement," Journal of Chemical Physics 37 (1962) 3007.

10. M. Göppert, "Über die Wahrscheinlichkeit des Zusammenwirkens zweir Lichtaquanten in einem Elementararkt," Die Naturwiss. (1929) 932.

11. M.Göppert-Mayer, "Über Elementarakte mit zwei Quanternsprüngen," Annalen der Physik 9 (1931) 273.

12. V. Hughes and L. Grabner, "The Radiofrequency Spectrum of $Rb^{85}F$ and Rb^{87} by the Electric Resonance Method," Physical Review 82 (1951) 561

13. P. Kusch, "Some Observations of Double- and Triple-Quantum Transitions," Physical Review 93 (1954) 1022.

14. W. L. Peticolas and K. E. J Rieckhoff, "Double-photon Excitation of Organic Molecules in Dilute Solutions," Journal of Chemical Physics 39 (1963) 1347.

15. W. L. Peticolas, John P. Goldsborough, and K. E. J. Rieckhoff, "Double Photon Excitation in Organic Crystals," Physical Reviw Letters 10 (1963) 43.

16. D. Fröhlich and H. Mahr, "Two-photon spectroscopy in anthracene" Physical Review Letters 16 (1966) 895.

17. D. L. Stockman, W. R. Mallory, and K . F. Tittel, "Stimulated Emission in Aromatic Organic Compounds," Proceedings of the IEEE 52 (1964) 318.

18. P. P. Sorokin and J. R. Lankard, "Stimulated Emission Observed from an Organic Dye, Cloro-aluminum Phthalocyanine," IBM Journal (March, 1966).

19. B. B. Snavely, "Blue Laser Emission from a Flashlamp-excited Organic Dye Solution," Applied Physics Letters 11 (1967) 275.

20. A. Bergman and Jortner, "Two-photon spectroscopy using dye lasers," Chemical Physics Letters 15 (1972) 309.

21. R. M. Hochstrasser, H. N. Sung, and J. E. Wessel, "Moderate Resolution Study of two-photon Spectrum of Benzene," Chemical Physics Letters 24 (1974) 7.

22. R. G. Bray, R. M. Hochstrasser, and J. E. Wessel, "Continuously tunable two-photon spectroscopy," Physics Letters 27 (1974) 167.

23. P. M. Johnson, M. R. Berman, and D. Zakheim, "Nonresonant multiphoton ionization spectroscopy: The four-photon ionization spectrum of nitric oxide" Journal of Chemical Physics 62 (1975) 2500.

24. L. S. Vasilenko, V. P. Chebotaev, and A. V. Shishaev, "Line Shape of Two-Photon Absorption in a Standing-Wave Field in a Gas," Journal of Experimental and Theoretical Physics 12 (1970) 113.

25. M. D. Levenson and N. Bloembergen, "Observation of Two-Photon Absorption Without Doppler Broadening on the 3S-5S Transition in Sodium Vapor," Physical Review Letters 32 (1974) 645.

26. F. Biraben, B. Cagnac, and G. Grynberg, "Experimental Evidence of Two-Photon Transitions Without Doppler Broadening," Physical Review Letters 32 (1974) 643.

27. D. Pritchard, J. Apt, and T. W. Ducas, "Fine Structure of Na 4d ^{2}D Using High-Resolution Two-Photon Spectroscopy," Physical Review Letters 32 (1974) 641.

28. R. G. Evans and P. C. Thonemann, "Laser produced dissociation and ionisation of residual hydrocarbons in a high vacuum system," Physics Letters 38A (1972) 398.

29. G. Petty, C. Tai, and F. W. Dalby, "Non-linear resonant photoionization in molecular iodine" Physical Review Letters 34 (1975) 1207.

30. J. A. R. Samson. "Line Broadening in Photoelectric Spectroscopy." The Review of Scientific Instruments. 40 (1969) 1174.

31. T. Koopmans, "Über die Zuordnung von Wellenfunktionen und Eigenwerten zu den einzelnen Elecktronen eines Atoms," Physica 1 (1933) 104.

32. F. H. M. Faisal, Theory of Multiphoton Processes, (New York: Plenum Press, 1987).

33. P. Lambropoulos, "Topics on Multiphoton Processes in Atoms," in Advances in Atomic and Molecular Physics ,vol. 12, edited by D. R. Bates and B. Bederson (New York: Academic Press, 1976).

34. L. Goodman and J. Philis, "Multiphoton Absorption Spectroscopy," in Applied Laser Spectroscopy: Techniques, Instrumentation, and Applications, edited by D. L. Andrews (New York: VCH Publishers, 1992).

35. Ammon Yariv, Quantum Electronics (New York: John Wiley and Sons, 1975).

36. J. E. Bjorkholm and P. F. Liao, in Laser Spectroscopy, eds. S. Haroche, J. C. Pebay-Peyyroula, T. W. Haensch, and S. E. Harris, (Berlin: Springer-Verlag, 1977), pg. 84.

37. P. Kruit, W. R. Garrett, J. Kimman, and M. J. van der Wiel, "Influence of AC Stark shifting on relative rates for two-colour multiphoton ionisation of Xe and Cs," Journal of Physics B: Atomic and Molecular Physics 16 (1983) 3191.

38. E. M. Purcell, "The Focusing of Charged Particles by a Spherical Condenser," Physical Review, 54 (1938) 818.

39. C. E. Kuyatt and J. A. Simpson, "Electron Monochromator Design," The Review of Scientific Instruments, 38 (1967) 103.

40. D. Roy and J. D. Carette, "Design of Electron Spectrometers for Surface Analysis," Topics in Current Physics, edited by H. Ibach 4 (1977) 13.

41. M. E. Rudd, in Low Energy Electron Spectroscopy, ed. K. D. Seroer, (New York: Wiley Interscience, 1972).

42. B. Wannberg, U. Gelius, and K. Siegbahn, "Design parameters in electron spectrometry," Journal of Physics E 7 (1974) 149.

43. H. Hafner, J. A. Simpson, and C. E. Kuyatt, "Comparison of the Spherical Deflector

and the Cylindrical Mirror Analyzers," The Review of Scientific Instruments, 39 (1968) 33.

44. P. Dahl, Introduction to Electron and Ion Optics, (New York: Academic Press, 1973).

45. R. Z. Herzog, Zeitschrift Physik 41 (1940) 18.

46. H. Wollnik, Optics of Charged Particles, (Orlando, Florida: Academic Press, 1987).

47. S. G. Anderson, K. W. Sohlberg, S. L. Howard, A. K. Shukla, and J. H. Futrell, "A High Transmission Hemispherical Energy Analyzer for Ion Spectrometry," Journal of the American Society of Mass Spectrometry 2 (1991) 506.

48. T. E. Everhart, "Simplified Analysis of Point-Cathode Electron Sources," Journal of Applied Physics 38 (1967) 4944.

49. B. Wannberg and A. Sköllermo, "Computer optimization of retarding lens systems for ESCA spectrometers," Journal of Electron Spectroscopy and Related Phenomena, 10 (1977) 45.

50. H. Ibach and D. L. Mills, Electron Energy Loss Spectroscopy and Surface Vibrations, (New York: Academic Press, 1982).

51. P. M. Dehmer and J. L. Dehmer, "Photoelectron spectroscopy using a supersonic molecular beam source. The $^2B_{3u} + e^- \leftarrow {}^1A_g$ transition in ethylene." Journal of Chemical Physics, 70 (1979) 4574.

52. J. A. R. Samson, "Line Broadening in Photoelectric Spectroscopy," The Review of Scientific Instruments, 40 (1969) 1174.

53. W. L. Fite, "Expansion of Gases from Molecular Beam Sources," Research Note #1 Extranuclear Laboratories, Inc. (January, 1971).

54. Hamamatsu Photonics, "Construction and Operating Principles of MCP," Catalog No. TMCP9001E01, (Shizuoka-ken, Japan: September, 1991).

55. J. L. C. Ford, "Position Sensitive Proportional Counters as Focal Plane Detectors," Nuclear Instruments and Methods 162 (1979) 277.

56. C. J. Borkowski and M. K. Kopp, "Position Sensitive Detector," IEEE Transactions for Nuclear Science, NS-15 (1970) 340.

57. M. Kopp, Interview by author, 7 September 1994.

58. R. N. Compton, J. C. Miller, A. E. Carter, and P. Kruit, "Resonantly Enhanced Multiphoton Ionization of Xenon: Photoelectron analysis," Chemical Physics Letters, 71 (1980) 87.

59. C. E. Moore, Atomic Energy Levels, vol 3. Circular of the National Bureau of Standards 467 (1958).

60. C. Jungen, "Rydberg Series in the NO Spectrum: An Interpretation of Quantum Defects and Intensities in the s and d Series," Journal of Chemical Physics, 53 (1970) 4168.

61. H. S. Carmen and R. N. Compton, "High-order multiphoton ionization photoelectron spectroscopy of nitric oxide," Journal of Chemical Physics, 90 (1989) 1307.

62. D. Zakheim and P. Johnson, "Two and three-photon resonances in the four- photon ionization spectrum of nitric oxide at low temperature," Journal of Chemical Physics. 68 (1978) 3644.

63. R. N. Compton and J. C. Miller, "Multiphoton Ionization Photoelectron Spectroscopy: MPI:PES," in Laser Applications In Physical Chemistry, ed. by D. K. Evans (New York: Marcel Dekker, 1989).

64. N. Westwood, private communication (1992).

65. O. Edqvist, E. Lindholm, L. E. Selin, and L. Åsbrink, "On the Photoelectron Spectrum of O_2," Physica Scripta 1 (1970) 25.

66. J. Swenson, private communication (1994).

67. A. Roth, Vacuum Technology, 3rd ed., (Amsterdam: North Holland, 1990).

68. E. Tannenbaum, E. M. Coffin, and A. J. Harrison, "The Far Ultraviolet Absorption Spectra of Simple Alkyl Amines," Journal of Chemical Physics, 31 (1953) 311.

69. D. F. Anderson, "A Photoionization Detector for the Detection of Xenon Light," IEEE Transactions for Nuclear Science 28 (1981) 842.

70. M. Asscher and Y. Haas, "Tertiary Amines as Possible Tunable Laser Materials in the Ultraviolet," Applied Physics 20 (1979) 291.

71. W. Zapka and F. P. Schäfer, "Excited-state Absorption and Two-Step Photoionization of Tertiary Amines," Applied Physics 20 (1979) 287.

72. F. Hirayama and S. Lipsky, "Fluorescence of saturated hydrocarbons," Journal of Chemical Physics 51 (1969) 3616.

73. F. Hirayama, W. Rothman, and S. Lipsky, "Fluorescence of saturated hydrocarbons. II. The effect of alkyl substituents," Chemical Physics Letters 5 (1970) 296.

74. W. Rothman, F. Hirayama, and S. Lipsky, "Fluorescence of saturated hydrocarbons. III. Effect of molecular structure," Journal of Chemical Physics 58 (1973) 1300.

75. C. G. Freeman, M. J. McEwan, R. F. C. Claridge, and L. F. Phillips, "The reaction of NH_3 with $Hg(^3P_o)$," Chemical Physics Letters 5 (1970) 555.

76. A. M. Halpern, "Fluorescent Properties of Saturated Systems: Hydrocarbons and Amines," Molecular Photochemistry 5 (1973) 517.

77. M. R. Robin, Higher Excited States of Polyatomic Molecules, Academic Press. New York and London. (1974).

78. A. M. Halpern, "Fluorescent Properties of Saturated Systems: Hydrocarbons and Amines," Molecular Photochemistry 5 (1973) 517.

79. C. G. Cureton, D. V. O'Connor, and D. Phillips, "Fluorescence Decay of Tertiary Aliphatic Amines," Chemical Physics Letters 73 (1980) 231.

80. M. Kawasaki, K. Kasatani, H. Sato, Y. Achiba, K. Sato, and K. Kimura, "Multiphoton ionization of triethylamine: Determination of the vibrationless S_2 level by laser photoelectron spectroscopy," Chemical Physics Letters 114 (1985) 473.

81. D. H. Parker, R. B. Bernstein, and D. A. Lichtin, "Multiphoton ionization-fragmentation patterns of tertiary amines," Journal of Chemical Physics 75 (1981) 2577.

82. K. Kasatani, M. Kawasaki, H. Sato, Y. Murasawa, K. Obi, and I. Tanaka, "Two-photon fluorescence excitation spectra of trialkylamines," Journal of Chemical Physics 74 (1981) 3164.

83. L. Goodman and J. Philis, "Multiphoton Absorption Spectroscopy," in Applied Laser Spectroscopy: Techniques, Instrumentation, and Applications, edited by D. L. Andrews, VCH Publishers, New York. (1992).

84. Y. Matsumi and K. Obi, Paper A11-305, Proceedings of the International Conference on Photochemistry, Tokyo (1979) pp. 130-131.

85. C. G. Cureton, K. Hara, D. V. O'Connor, and David Phillips, "The Photophysics of Tertiary Aliphatic Amines," Chemical Physics 63 (1981) 31.

86. A. Hiraya, Y. Achiba, N. Mikami, and K. Kimura, "Vibrationally resolved photoelectron spectra of jet-cooled naphthalene: Intramolecular relaxation

processes in S_1 and S_2 states.

87. H. Sato, M. Kawasaki, K. Toya, K. Sato, and K. Kimura, "Photoelectron Spectroscopic Evidence for the Competition of Ionization and Internal Conversion at the S_2 Excited State of Trimethylamine," Journal of Physical Chemistry 91 (1987) 751.

88. P. J. Kozak and H. Gesser, "The Photolysis of Triethylamine, and Reactions of Methyl Radicals with Triethylamine and Diethylamine," Journal of the American Chemical Society 86 (1960) 448.

89. U. Gelius, L. Asplund, E. Basilier, S. Hedman, K. Helenellund, and K. Siegbahn, "A high resolution multipurpose ESCA instrument with X-ray monochromator," Nuclear Instruments and Methods in Physics Research B1 (1984) 85.

90. B. Wannberg and A. Sköllermo, "Computer optimization of retarding lens systems for ESCA spectrometers," Journal of Electron Spectroscopy and Related Phenomena 10 (1977) 45.

91. K. Watanabe and J. R. Mottl, "Ionization potentials of ammonia and some amines," Journal of Chemical Physics 26 (1957) 1773.

92. K. Watanabe, T. Nakayama, and J. R. Mottl, "Ionization potentials of some molecules," Journal of Quantitative Spectroscopy and Radiative Transfer 2 (1962) 369.

93. D. H. Aue, H. M. Webb, and M. T. Bowers, "Quantitative Proton Affinities, Ionization Potentials, and Hydrogen Affinities of Alkylamines," Journal of the American Chemical Society, 98 (1976) 311.

94. M. I. Al-Joboury and D. W. Turner, "Molecular photoelectron spectroscopy. Part II. A summary of ionization potentials." Journal of the Chemical Society. (1964) 4434.

95. O. Edqvist, E. Lindholm, L. E. Selin and L. Åsbrink, "On the Photoelectron Spectrum of O_2," Physical Scripta 1 (1970) 25.

96. C. Crocker and P. L. Goggin, "Infrared and Raman Spectroscopic Studies of Conformations of Solid Triethyl- Diethyl(methyl)- and Ethyldimethyl -amines, -phosphines, and arsines," Journal of the Chemical Society, Dalton Transactions (1978) 388.

97. M. Z. El-Sabban and B. J. Zwolinski, "Normal Coordinate Treatment, Mean Square Amplitudes of Vibration, Coriolis Coupling Coefficients, and Thermodynamic Properties for Fluorochlorobromomethane," Journal of Molecular Spectroscopy 19 (1966) 231.

98. M. Diem and D. F. Burow, "Vibrational spectra and normal coordinate analysis of bromochlorofluoromethane," Journal of Chemical Physics 64 (1976) 5179.

99. B. B. Neto and R. E. Bruns, "A Sum Rule for the Vibrational Intensities of Substituted Methanes," Journal of Physics Chemistry 94 (1990) 1764.

100. J. Canceill, L. Lacombe, and A. Collet, "Analytical Optical Resolution of Bromochlorofluoromethane by Enantioselective Inclusion into A Tailor-Made 'Cryptophane' and Determination of Its Maximum Rotation," Journal of the American Chemical Society 107 (1985) 6993.

101. S. H. Wilen, K. A. Bunding, C. M. Kascheres, and M. J. Wieder, "On the Optical Activity of Bromochlorofluoromethane," Journal of the American Chemical Society 107 (1985) 6997.

102. G. Glockler and G. R. Leader, "Raman Effect of Fluorochlorobromomethane," Journal of Chemical Physics 8 (1940) 125 and 699.

103. E. K. Plyler and M. A. Lamb, Journal of Research of the National Bureau of Standards (U.S.) 46 (1951) 382.

104. K. S. Pitzer and E. Gelles, "The Vibration Frequencies of the Halogenated Methanes and the Subsitution Product Rule," Journal of Chemical Physics 21 (1953) 855.

105. E. J. Jacob, "Structure of bromochlorofluoromethane by electron diffraction," Journal of Molecular Structure 52 (1979) 63.

106. M. K. Hargreaves and B. Modarai, Journal of the Chemical Society D (1969) 16.

107. S. H. Wilen, K. A. Bunding, C. M. Kasheres, and C. M. Wieder, Table of Resolving Agents and Optical Resolutions, edited by E. L. Eliel (South Bend, Indiana: University of Notre Dame Press, 1972).

108. I. Novak, S. C. Ng, and A. W. Potts, "The photoelectron spectrum of a chiral molecule CHFClBr," Chemical Physics Letters 215 (1993) 561.

109. F. Brogli and E. Heilbronner, "The Competition between Spin Orbit Coupling and Conjugation in Alkyl Halides and its Repercussion on their Photoelectron Spectra," Helvetica Chimica Acta 54 (1971) 1423.

110. Y. S. Touloukian and T. Makita, Specific Heat, Thermophysical Properties of Matter, vol. 6 (New York: IFI/Plenum, 1970).

VITA

John Eilef Mathis was born in Vermillion, South Dakota. He attended public schools there, and in Mt. Pleasant, Michigan, where he and his family had moved. After graduating from Central Michigan University with a Bachelor of Science degree in physics, he attended graduate school at Purdue University where he received his Master of Science degree in physics.

He began his professional employment with Union Carbide's Nuclear Division in Oak Ridge, Tennessee. There, he worked on improving analytical instrumentation used in process control. He received a U.S. patent for helping to develop an improved apparatus for calibrating mass spectrometers.

While at Oak Ridge, he started his work on a Master of Arts degree in economics at The University of Tennessee - Knoxville with an emphasis in industrial organization and econometrics. He left Union Carbide to concentrate on his studies. His master's thesis studied the effect of mandatory fuel efficiency standards on gasoline consumption. While completing this thesis he taught mathematics and physics at Lord Fairfax Community College in Middletown, Virginia. His thesis was later published in and had an influence on governmental policy decisions.

He continued his scientific career with the Riverside Research Institute in Arlington, Virginia. At Riverside Research Institute, he analyzed space-borne remote sensing systems for the Defense Advanced Research Programs Agency (DARPA).

Later, he joined the Eastman Kodak Company in Rochester, New York as a

research engineer in their special programs division. His worked on a variety of image processing projects, and received an award for his achievements in one particularly difficult project.

He attained further advancement in his scientific career by becoming a senior scientist at Technology Development Corporation in Huntsville, Alabama. There, he helped develop a number of laser radar systems. One of the most interesting systems he helped develop was a dual-frequency, mode-locked laser radar transmitter that used only one laser cavity.